Structural health monitoring of composites by combining machine learning and synthetic evaluation methods with vibro-acoustic modulations

Vom Promotionsausschuss der
Technischen Universität Hamburg

zur Erlangung des akademischen Grades

Doktor-Ingenieur (Dr.-Ing.)

genehmigte Dissertation
(Monografie)

von
Benjamin Boll

aus
Berlin

2025

Tag der mündlichen Prüfung: 18.12.2024

Vorsitzender des Prüfungsausschusses: Prof. Dr.-Ing. habil. Bodo Fiedler
(Technische Universität Hamburg)

Gutachter: Prof. Dr.-Ing. Robert Meißner
(Technische Universität Hamburg)
Prof. Dr.-Ing. Benedikt Kriegesmann
(Technische Universität Hamburg)

Thesis DOI: `https//doi.org/10.15480/882.14123`

Dedicated to my family

Abstract

The vibro-acoustic modulation (VAM) method is known for its high sensitivity to detect even small damages and is applied non-destructively. VAM uses a high-frequency ultrasonic carrier wave, that is modulated in the specimen by a high-amplitude pump wave of significantly lower frequency. The method was introduced in the 1990s, and the literature today includes over 200 journal publications in which VAM is applied to many laboratory-based applications. However, no industrial application has yet been proclaimed. Since transitioning from the laboratory to the industry is one of the biggest hurdles, this thesis aims to address and overcome the limitations to enable the next step toward industrial applications.

The requirements on the method depend on whether it will be used in the context of non-destructive testing (NDT) or the structural health monitoring (SHM). VAM, as traditionally described in the literature, has no defined baseline of the measurement. Hence, measurements of different specimens can not be reliably compared. In SHM applications, the first measurement is usually assumed to be pristine and is utilised as this baseline. Despite current investigations into estimating a baseline, it remains a major challenge (due to complex signal modulation and dependencies on the material, preexisting damage, *etc.*). To overcome this issue—specifically for NDT applications—this thesis proposes a data-driven approach that is validated with two applications. First, the adhesive bonding of fibre composite structures is investigated. Single-lap shear specimens with so-called weak bonds and kissing bonds were prepared by inserting a non-stick film, or by contaminating the bond line with a release agent. It is shown that a data-driven evaluation can accurately differentiate between undamaged and damaged specimens in specific frequency ranges, even though the differences based on the traditional evaluation methods are minimal. The trained neural networks are evaluated to recursively generate information on the significance of the input values, leading to a deeper understanding of the VAM method and its mechanisms. The applicability of this data-driven evaluation is confirmed

by testing welded steel specimens, where half of them contained crystallisation defects that resulted from false welding parameters.

When VAM is applied as an SHM method, it is advantageous to leverage the ambient vibrations as the modulating pump wave. Ideally, SHM systems are built with low-power and energy-harvesting devices to reduce installation and maintenance costs. The challenge results from variations of the ambient vibration due to changes of environmental influences. Thus, the traditional VAM measurements would neither be consistent nor comparable between the measurements over time.

This challenge is overcome by the proposed synthetic computation of the VAM signal. This synthetic computation minimises the dependency on the ambient vibration so that the VAM measurement can be performed on complex components without interference from environmental changes. The presented approach significantly reduces the requirements on the sensor nodes in terms of sampling rate, measured data points, data size, and energy required to drive the high-frequency emitter. Thus, the usage of self-sustaining energy-harvesting sensor nodes comes into reach. Furthermore, the synthetic method can be implemented into most existing SHM systems that contain acoustic emissions or guided wave measurements with minimal adaptations. Finally, the viability of the synthetic VAM method is demonstrated on larger and more complex structures.

Kurzfassung

Die Vibroakustische Modulation (VAM) ist eine zerstörungsfreie Prüfmethode, die sich durch eine hohe Empfindlichkeit für die Detektion von Schäden auszeichnet. Erstmals wurde die Methode in den 1990er Jahren publiziert. Mittlerweile befassen sich bereits über 200 Veröffentlichungen mit VAM, welche sich jedoch auf kleine Strukturen beschränken, die hauptsächlich under idealen Laborbedingungen getestet wurden. Eine industrielle Anwendung wurde noch nicht publiziert.

Die Anforderungen an die Methode variieren je nach Anwendung im Rahmen der zerstörungsfreie Prüfung (NDT) oder bei der Überwachung des strukturellen Zustands (SHM). Die größte Herausfoderung liegt in der genauen Zuordung von einem Modulationswerts zu einem Schadenszustands, mit dem die Messungen an verschiedenen Proben verglichen werden können. Bei SHM-Anwendungen wird dies üblicherweise umgangen, indem der initiale Zustand als fehlerfrei angenommen wird, und damit als Vergleichswert dient.

Um diese Herausforderungen bei NDT-Anwendungen zu überwinden, wird in dieser Arbeit ein datengetriebener Ansatz vorgeschlagen, der an zwei Anwendungsfällen validiert wird. Die Detektion von Adhäsionsdefekten in Faserverbunden ist relevant für die Fertigung von Faser-Verbunden. Überlappklebungen wurden unter idealen Bedingungen und mit eingebrachten Defekten hergestellt. Dazu wurde entweder eine PTFE-Folie eingelegt oder die Klebestelle mit einem Trennmittel kontaminiert. Beide Defekte verringern die erreichte Scherfestigkeit der Proben signifikant. Es wurde gezeigt, dass durch eine datengetriebene Auswertung von VAM eine präzise Klassifikation der Proben in die einzelnen Herztellungsarten erfolgen kann, trotz nur minimaler Unterschiede in der Auswertung der traditionell verwendeten Schadens-Indezes von VAM. Zusätzlich wurden die trainierten neuronalen Netze rekursiv evaluiert, um Informationen über die Bedeutung der Seitenbänder (Eingangswerte) zu generieren, was zu einem tiefgehenderen Verständnis der VAM-Methode und ihrer Mechanismen führt. Bei der

zusätzlichen Überprüfung von geschweißten Stahlproben, bei denen ein Kristallisationsfehler in der Schweißnaht eingebracht wurde, konnte die Relevanz der datengetriebenen Auswertung bestätigt werden.

Die Anwendung von VAM als SHM-System bringt zusätzliche Herausforderungen mit sich. Idealerweise werden SHM-Systeme mit energieeffizienten Sensorknoten gebaut, um die Installations- und Wartungskosten zu minimieren. Bei der Anwendung von VAM als SHM-Methode empfiehlt es sich, die bereits vorhandenen Vibrationen als modulierende niederfrequente Schwingung zu nutzen. Die Herausforderung dabei liegt in der Variation dieser Schwingungen aufgrund wechselnder Umwelteinflüsse. Daher sind konventionelle VAM-Messungen an realen Strukturen weder konsistent noch über die Zeit vergleichbar.

Diese Herausforderung konnte durch eine synthetische Berechnung des VAM-Signals umgangen werden. Mit dieser Methode kann die Abhängigkeit von Umgebungsschwingungen minimiert werden, sodass VAM-Messungen an komplexen Bauteilen ohne Beeinträchtigung durch Umgebungsänderungen durchgeführt werden können. Der vorgestellte Ansatz reduziert deutlich die Anforderungen an Sensorknoten in Bezug auf Abtastrate, gemessene Datenpunkte, Datengröße und die für den Betrieb des Ultraschallsenders erforderliche Energie. Dadurch könnten auch autarke Sensorknoten eingesetzt werden. Zudem ist VAM in die meisten bestehenden SHM-Systeme integrierbar, bei denen die akustischen Emissionen oder geführte Wellenmessungen gemessen werden. Die Anwendbarkeit der traditionellen sowie der synthetischen VAM wurde auch an größeren und komplexeren Strukturen demonstriert, wobei insbesondere die synthetische Variante vielversprechende Ergebnisse erzielte.

Contents

List of Abbreviations

Abbreviation	**Description**
AM	Amplitude modulation
ANN	Artificial neural network
ASTM	American society for testing and material
BVID	Barely visible impact damage
CDS	Characteristic damage state
CM	Cross-modulation
CMVA	Cross-modulated vibro-acoustics
CNC	Computerised numerical control
DAET	Dynamic acousto-elastic test
DEL	Delamination
EASA	*European union aviation safety agency*
FAA	*Federal aviation administration*
FFT	Fast fourier transform
FI	Feature importance
FM	Frequency modulation
FRP	Fibre-reinforced polymer
GFRP	Glass-fibre reinforced polymer
Laminate	Composite of several individual layers stacked on top of each other and glued together
NAM	Non-linear acoustic modulation
NDT	Non-destructive testing
NUVM	Non-linear ultrasound vibro-acoustic modulation technique
NWMS	Non-linear wave modulation spectroscopy
MSE	Mean-squared error
PM	Phase modulation
PTFE	Polytetrafluoroethylene
SHAP	SHapley Additive exPlanations
SHM	Structural health monitoring
STFT	Short-time fourier transform
UD	Unidirectional
VAM	Vibro-acoustic modulation
VARTM	Vacuum-assisted resin transfer moulding
VMT	Vibro-acoustic modulation technique

Symbol	**Description**	**Unit**
	Latin symbols	
A	Amplitude	dB or V
E	Modulus	GPa
f	Frequency	Hz
$\mathcal{F}$	Fast Fourier Transform	
MI	Modulation index	dB
n	Number of stress levels for synth. VAM	
n_f	Number of points used for fitting the signal	
n_freq	Number of neighbouring frequencies in the data set	
p	Number of points for a signal reconstruction	
R	Modulation intensity	
R_σ	Amplitude ratio of maximal to minimal stress	
s	No. of sidebands	
sq	square wave	
τ	Time of measurement	s
X	Vibration	
$\mathbf{X}$	Dataset of sidebands	
$\mathbf{X}_\mathrm{APM}$	Dataset of Amplitudes and Phases	
	Greek symbols	
β	Nonlinear parameter	dB
ϕ	Phase of the signal	$^\circ$
σ	Stress	MPa
σ_l	Stress level	MPa
	Indices	
APM	Amplitude and phase modulation	
c	Carrier or probe vibration	
eigen	Nearest eigenmode	
p	Pump vibration	
r	Resulting signal	
s	Sampling rate	
SB	Sidebands	

1. Structural health monitoring for polymer composites

Complex mechanical systems are the foundation of our modern society. Maintaining and monitoring these existing structures are significant concerns to prevent failures resulting from the occurring loads, the service conditions, corrosion, or even an improper usage. Additionally, the ageing of these structures raises the probability of damages and maintenance costs. Therefore, a reliable assessment of the structural integrity is the ultimate goal for users, owners and manufacturers [1–3]. Only knowing the current structural state with its loads and emerging defects allows for an optimal utilisation, preventing catastrophic failures and reduced downtime due to scheduled maintenance [4].

The traditional concepts for a preventive maintenance routine consist of predefined routine checks and scheduled replacements of critical components independent of their actual wear. This procedure results in inefficient operations, wasted resources and many downtimes of the structure [5]. The economic relevance of improving the structural evaluation is unquestionable.

- In Germany, around 30000 wind turbines are maintained on land, with an average service life of 13.9 years. The costs for maintaining these turbines increase after ten years of operation from 44 % to 55 % of total operating costs [6]. Furthermore, most insurance claims can be attributed to damaged wind turbine blades (41.4 %) with an average cost of 240,000 US$, while poor maintenance is the most reported cause (24.5%) [7].
- In the next two decades, approximately 41170 passenger aircraft will be delivered, which implies a volume of 7.2 trillion US$. Furthermore, 2.5 trillion US$ are estimated for maintaining, repairing and overhauling the in-service fleets [8].

Both industries depend on fibre-reinforced composites as an advanced lightweight material that is tailored for the anticipated load cases. However, due to the layered structure of the material, impact damages are barely visible from the outside but jeopardise the structural integrity. Hence, non-destructive damage detection and sophisticated load monitoring are essential.

Over the years, a wide variety of highly effective *non-destructive testing* (NDT) methods have been developed to ensure a reliable and safe operation. Typical NDT methods (*e.g.* thermography, ultrasonic inspection, X-ray or magnet resonance) are used to inspect a structure after manufacturing and at regular assessments over the lifetime. Most NDT methods are well understood, approved and standardised by technical committees (*e.g.* *American Society for Testing and Materials* ASTM). However, many structural components are only accessible during downtime and often require disassembly of secondary structured to be accessible, which reduces profit as shown in Fig. 1.1.

a) Inspection of a wind turbine

b) Disassembly of an aircraft for maintenance (D-Check)

Figure 1.1.: Potential fields for the application of SHM systems.

To prevent downtimes, several NDT techniques can be employed for continuous monitoring by integrating sensors into the structure. By combining the data from these integrated sensors with data from environmental and loading conditions, and applying sophisticated signal processing, allows for a predictive and condition-based maintenance planning, referred to as *Structural Health Monitoring* (SHM). The reduction of maintenance duration and cost coupled with condition-based maintenance makes the adaptation of SHM systems an economic decision.

Vibro-acoustic modulation (VAM) is a promising method for NDT and SHM research. In the literature, a high sensitivity towards damage detection was shown. However, this method also faces several challenges and has, to the author's knowledge, not yet been applied to actual industrial applications. Based on the demand for a reliable structural health assessment, this thesis focuses on establishing VAM for application in the NDT and SHM contexts. Since the requirements for the measurement method depend on the respective application, the overall research hypothesis is divided into two parts.

For NDT applications, the challenge of VAM is the missing baseline of the measured modulation, which is required for a comparison and, subsequently, the decision to determine whether damage is present. The system's response depends on many parameters since the traditional VAM method evaluates the steady state vibration, which results from a superposition of many different pathways of the excited vibrations. For example, differences in the specimen dimensions, the position of the bonded piezoceramics, the frequencies of introduced vibrations, and environmental factors (*e.g.* temperature, ambient vibrations) affect the measured signal. Therefore, estimating the structure's condition without a comparative measurement is challenging. The first research hypothesis, which will be discussed in Chapter 4, is derived as:

> *The VAM method can be applied as a non-destructive testing method for similar parts, with machine learning algorithms enhancing its sensitivity.*

Two experiments were conducted to evaluate this sub-research hypothesis. One of the most challenging aspects of manufacturing composite structures is the quality assurance of adhesive bonds. Especially, the detection of contaminations by a release agent is not possible by traditional NDT methods. Hence, this use case is an ideal example for evaluating the high sensitivities of VAM, coupled with the hypothesis that data-driven models approximate the baseline and allow for the detection of these defective bonds. Analogues to the GFRP specimens, this hypothesis was evaluated on metallic specimens to prove the significance of the data-driven approach, independent of the material or use case. Crystallisation defects in welded metallic specimens were created, which is a severe problem and difficult to detect.

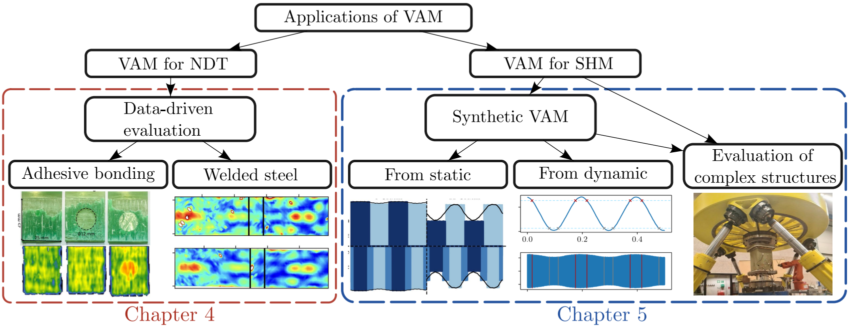

Figure 1.2.: Overview of the structure of this thesis. The content of the individual Chapters is visualised by a preview of one Figure.

If VAM is included in a SHM system, the baseline for the measurement is usually the first measurement after the manufacturing process. However, the actual implementation as a sensor network, coupled with variations of environmental conditions, hinders the application of VAM. Since the present ambient vibrations of the structure are ideal for utilisation as the pump wave, the influences posed by the changing ambient vibrations has to be compensated by the VAM method. Hence, the sub-hypothesis for Chapter 5 is derived as:

The pump vibrations required for VAM can be approximated by subsequent measurements at different load levels of the structure into a synthetic VAM signal.

This hypothesis is evaluated by a set of experiments conducted on several specimens, with sizes from coupon level to more complex structures. The typical damage parameters used for the VAM evaluations are synthetically generated by measuring only the carrier frequency at distinct stress levels. A synthetic signal is created from these measurements. Finally, each typical damage parameter can be acquired from measurements independent of the amplitude or frequency of the pump wave. Finally, the possibility of recreating the VAM measurements from a burst-excitation for the carrier vibration is tested and discussed.

This thesis consists of six chapters. After this introduction, the state of the art for the vibration-based NDT and SHM for composite materials is presented. In Chapter 3, the specimen manufacturing and the testing methods are defined. Specific information is given within the relevant chapters. Chapters 4 and 5 each present and discuss the introduced research hypotheses. Despite the focus on damage detection and structural health monitoring of fibre-reinforced polymers, both chapters also include additional evaluations of the developed methods on comparable metallic structures. Therefore, the applicability of VAM for the two material types can be evaluated. In Chapter 6, a general conclusion for the application of VAM is drawn and discussed, followed by the outlook. Figure 1.2 gives an overview of the thesis structure.

It should be noted that parts of the presented results were already published [9–11]. Additional contributions to VAM were made but exceed the scope of this thesis [12–17]. Collaborations with other institutions have also led to synergies in data-driven evaluations of magnesium degradation [18] and the experimental verification of reaction energies during the cross-linking of thermosetting polymers [19].

2. Vibration-based structural health monitoring

2.1. Composite materials

During the service life, fibre-reinforced polymer (FRP) structures are subjected to various mechanical and environmental loads far below the failure in a monotonic loading test. However, these lower loads result in degradation phenomena, which decrease the remaining lifetime of the structure. Due to the anisotropy, which results in advanced material properties, FRPs have complex damage mechanisms initiated by partial micro-damages that accumulate and result in ultimate failure [20, 21]. Combinations of different damage initiation and propagation mechanisms result from the multi-scale aspect of FRPs, illustrated in Figure 2.1. For the definition of FRPs, a second coordinate system simplifies the material definition with one axis pointing orthogonal to the plate-like structure. The damage resistance depends on the structural geometry and loading orientation of the *structural* level, the laminate layup, the ply thickness and the stacking order in the *Macro* material level. Finally, the used materials as fibres and matrix also define the material properties in the *Meso* level and the interface between both in the *Micro* level [22, 23]. Further influences include the environmental conditions and many more [24, 25].

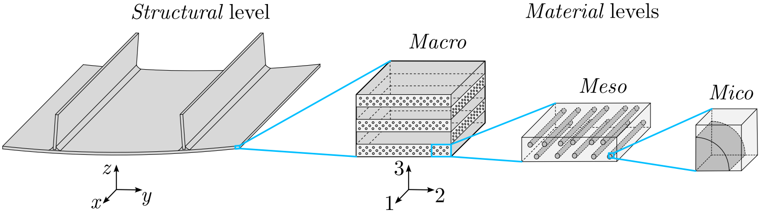

Figure 2.1.: Visualisation of the multi-scale aspect of FRP. Note that the coordinate system changes from a global to the material level.

Even though the fatigue behaviour is superior compared to other materials, it must be considered for FRP structures [20]. Typically, the fatigue life of FRP materials can be divided into three stages. This degradation process is illustrated in Figure 2.2 for a typical fatigue damage evolution in a cross-ply laminate with a [0,90,0] layup. Even if this schematic assumes a tensile-tensile load, similar states of degradation can be observed for other loadings. Note that the damages are assumed to be due to an internal biaxial plate-like stress state. In regions with geometric discontinuities such as free edges or notches, a triaxial stress state occurs and affects the damage evolution slightly [22].

During stage I, mainly micro-cracks are formed due to the fatigue load in the 90° layer, which is oriented transversely to the loading direction. These initial micro cracks act as initiators for the formation of cracks that propagate through the 90° ply as matrix crack or inter-fibre failure (c.f. Figure 2.2*a*, *b*). Throughout this first stage, the density of inter-fibre failures increases until a saturation with a uniform spacing is reached [22]. This state is known as the characteristic damage state (CDS) and is shown in Figure 2.2*c*. Additionally, first fibre-fractures occur in the 0° ply caused by stress concentrations at the intersection to the inter-fibre failure. In the second stage, the damage growth is significantly reduced. High inter-laminar shear stresses occur at an inter-fibre failure, which results in

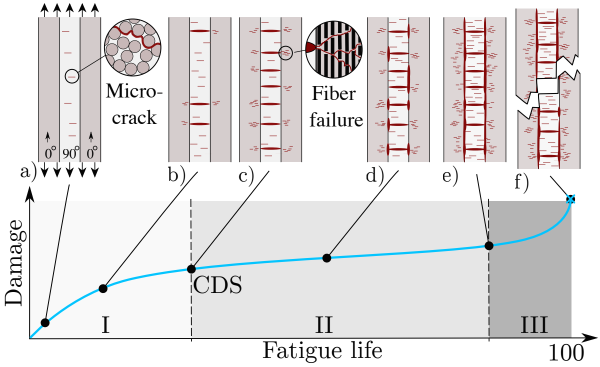

Figure 2.2.: Schematic representation of the fatigue damage evolution of a cross-ply FRP with associated damage mechanisms: *a*) micro-cracks in the matrix and fibre-matrix interface; *b*) growing micro-cracks lead to transverse cracks, isolated fibre failure in the 0° layers due to the transverse crack-induced stress; *c*) increase in crack density until saturation at characteristic damage state (CDS); *d*) and *e*) growing delaminations between the individual layers; *f*) final failure (adapted from Müller [26]).

a separation fracture between the individual layers of the laminate. So-called “delaminations” arise as a separation of the individual layers. Without any crack-stopping mechanisms, the delaminations can spread abruptly over larger areas. In the third stage, the bond between the plies is significantly reduced due to large delaminations. The load sharing between the plies is interrupted, and the composite is not behaving as single laminate any more [20]. Isolated fibre-fractures in the load-bearing 0° fibres result in stress concentrations and finally initiate the ultimate failure of the laminate [21].

The damage curve—illustrated in Figure 2.2—is calculated as:

$$\text{Damage} = 1 - \frac{E}{E_0} \tag{2.1}$$

where E is the current Young’s modulus and E_0 is the initial modulus at a pristine state. The decrease in stiffness in the first stage can be attributed to inter-fibre failures in the matrix material. The delaminations are mainly responsible for the slight reduction in modulus since they do not primarily contribute to the laminate stiffness. The fibre fractures in the third stage of the fatigue life result in a substantial decrease of stiffness and, hence, an increase in *damage*.

The precise characteristics of this degradation depend on many factors (*e.g.* the laminate layup, the thickness of the individual laminae, and the fatigue loading). While great effort has been made to model the fatigue damage in FRPs, a general fatigue model has yet to be established in the literature. Hence, the NDT of these structures or the implementation of a reliable SHM system is essential for a safe and reliable service of FRP structures [21].

2.2. Non-destructive testing of composites

Most NDT methods utilise direct measurements to evaluate the structure without affecting functionality and integrity. The term “direct measurement” implies the knowledge of the physical relations of the method with a direct proportionality between the measured entity and the material properties. Currently used NDT methods are based on visual or localised techniques such as acoustics, ultrasonics, magnetic field, thermal field, radiography or thermal methods [3]. Acoustic emission and ultrasonic testing are well understood and applied to many industrial applications [27]. While acoustic emissions are *passively* recorded transient stress waves—emitted from instantaneous energy/stress releases due to growing cracks or dislocations—the ultrasonic testing relies on the transmission and reflection of the *actively* introduced high-frequency bulk waves [27].

Over the last decades, the application of guided (ultrasonic) waves and acousto-ultrasonic techniques has been under immense research since they allow an *active* non-destructive evaluation of the structure. Lamb wave testing is the most used guided wave approach and has become promising for many industrial applications since lamb waves can propagate over large distances in thin-walled structures. These lamb wave inspections utilise the changes in wave attenuation and mode conversations due to damage interactions in the path between the sending and receiving probe [27–29]. However, the processing of lamb waves is complex due to noise, environmental influences and intrinsic characteristics of the structure, which affect the received signals [30]. In this context, the term "damage" defines a change in material properties, boundary conditions or system connectivity that ultimately affects the system's performance or integrity [1]. Since many structural parts are covered and damages mainly occur at the intersection between two parts, most damages might not be detectable by eyesight. Therefore, various highly effective NDT methods were developed and devised to monitor damages in different materials and structures. A relevant but incomplete overview is given in Figure 2.3 since the amount of published methods and variations is immense.

2.3. Structural health monitoring

Due to the non-continuous evaluation cycles, the application of NDT can be classified as "reactive" evaluation. The term "reactive" means that the testing is defined by a schedule or after unforeseen events which threaten the structural integrity (*e.g.* earthquakes in civil engineering, bird strikes, crashes, *etc.* at mechanical structures). Hence, significant efforts are being made to continuously diagnose the structural integrity using sensor systems that are permanently employed or integrated into the structure [1, 3]. These systems for a continuous monitoring or the SHM are "proactive" and provide real-time information that can be used to make informed decisions about maintenance and repairs [2]. A comparison between the fundamental concepts of NDT and SHM methods can be found in Table 2.1.

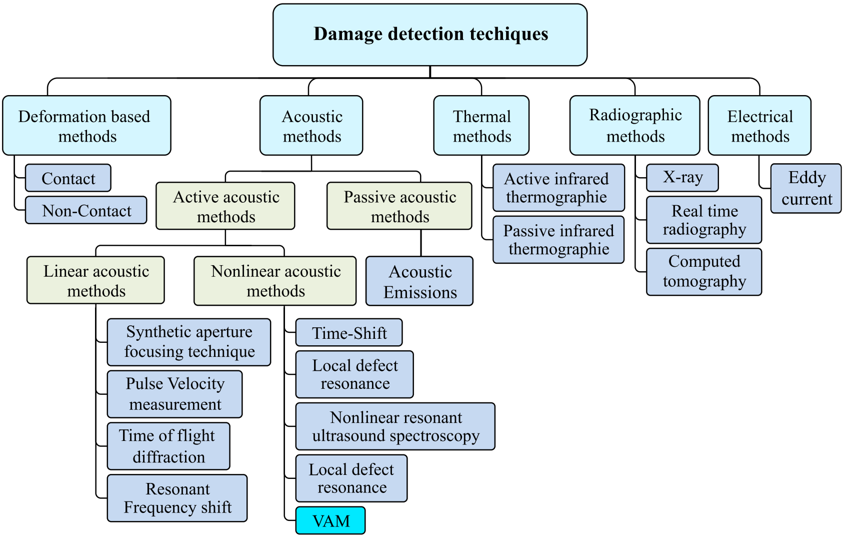

Figure 2.3.: Classification of non-destructive damage detection techniques. The focus of this thesis is on VAM, which is an active non-linear acoustic method. (adapted from Karve *et al.* [31])

For SHM applications, a network of sensors (*e.g.* piezoceramics, accelerometers or strain gauges) and actuators (*e.g.* piezoceramics or electrodynamic/hydraulic shakers) enable the real-time detection, localisation, and quantification of damage and the prediction of the remaining lifetime so that the NDT becomes an integral part of the structure [2, 33]. As a result, the structure's environmental loads and evolving degradation must be monitored and merged into a holistic process to monitor its health throughout its life cycle. An enormous amount of work has been published on SHM and NDT, which mainly focuses on automatic, and reliable damage detection technologies.

2.4. Guided waves for damage detection

Numerous NDT applications based on guided waves have already been published. Guided waves promise enormous potential for reliable damage detection but have reached a lower maturity level compared to the commonly used acoustic emissions and ultrasonic testing. Smart sensors integrated into critical components of a monitored structure have achieved essential steps towards sensitive and robust SHM methods in the last decades [27]. Guided waves use the structure itself

Table 2.1.: Comparison between the main characteristics of NDT and SHM for the evaluation of complex structures (adapted from [32])

NDT	**SHM**
Inspection with external probes and equipment	Permanently attached sensors at fixed locations at the structure
Offline monitoring: most parts must be disassembled for inspection	Online monitoring, inspection during operations or scheduled downtime
Time-based maintenance Checks must be conducted regularly	Condition-based maintenance. Disassembly only required for repair
Labour intensive evaluations	Automated evaluations
Mature technologies are available	Still under development for complex structures

as a waveguide, allowing them to propagate over long distances. Hence, larger areas in both isotropic and anisotropic plates can be inspected, which yields a potential of saving in inspection time and costs and results in a fast-growing number of applications [2, 27, 34].

Like classical elastic waves, guided waves are travelling disturbances that transport energy in an elastic medium without transferring matter and follow the linear stress-strain relation and Newton's second law. In contrast to bulk waves, where only longitudinal and shear modes exist in most materials, guided waves have an infinite number of wave modes, which are generated simultaneously and propagate as a superposition of all excited modes. The high number of modes results in complexity, which is challenging for industrial applications [34].

Lord Rayleigh (1885) identified the first guided surface waves, after whom this class of waves was named. The amplitude of Rayleigh waves is decreasing rapidly with depth, making them useful for inspecting surface defects. The decrease rate depends on the wavelength [27].

If a tested structure is plate-like, with its thickness in the wavelength range, the guided waves become lamb waves. The structural evaluation with lamb waves is attractive for plate-like structures due to their ability to travel large distances and inspect extensive areas of the structure. The interaction of these waves is called “linear” if the output of the response signal correlates with the strength of the input signal, as defined by Hooke's law [35]. Usually, changes in velocity, scattering effects, attenuation, and mode conversations of the introduced guided waves are evaluated to detect damage. These methods are ideal when the present damage significantly alters the linear features of the propagating ultrasonic wave, like a reduction of thickness and open cracks [2, 27, 36–38]. However, the evaluation of these linear features can be challenging. It requires sophisticated measurement equipment to detect and visualise the changes since it is ambiguous to differentiate whether the effect stems from damages, structural features or changes in environmental/operational conditions [39]. This can be explained since fatigue or corrosion cracks are mostly closed and in contact. Hence, they are invisible for the wave due to minimal differences in material impedance [37]. Therefore, the scientific community is actively working on non-linear vibration and acoustic phenomena that are typically more sensitive to minor damage severities than linear methods [40, 41]. However, it is not the goal to replace but rather to complement the existing linear techniques, which are already known and certified [42].

The non-linear approaches can be differentiated into "classical" methods, which characterise the damage by evaluating higher harmonics, and the "non-classical" methods, which were more recently developed. The higher harmonics of the "classical" non-linear methods result from a non-linear stress-strain relationship of a homogeneous material, resulting in a distortion of the propagating wave. Discontinuities in micro and macro scale (*e.g.* fatigue fractures in metals or delaminations in composites) result in "non-classical" non-linear phenomena in the ultrasonic response [37]. These "non-classical" non-linear phenomena include the occurrence of higher harmonics where the amplitudes decay less compared to

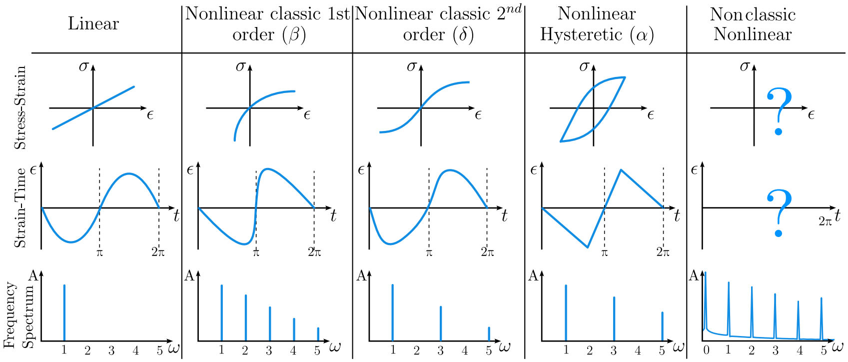

Figure 2.4.: Illustrations of the stress-strain/stress-time curves and their resulting patterns in the frequency spectrum are shown for a linear, non-linear and non-classical non-linear material-behaviour (adapted from [41]). Note that the indices of the harmonics are given at the frequency spectrum.

the classical case, higher harmonics of unusually high orders, frequency mixing, generation of subharmonics and more [39]. In Figure 2.4, wave propagation and resulting harmonics of a linear stress-strain relation are compared to various non-linear and hysteretic contributions. It is shown that the different non-linear behaviours result in distinct patterns in the frequency domain, as explained by Van Den Abeele *et al.* [41]. Consequently, for a thorough evaluation, the amplitudes of several sidebands should be considered to differentiate the type of non-linearity or even to separate the superposition of the several sources of non-linearity. Since, "the full mechanism of the nonlinear response is not yet understood" [41], actual measurements include many other influences, such as dissipative mechanisms, cross-modulation, modulation transfer, memory effect, and contact acoustic nonlinearity, which complicate an analytical explanation [39]. These "non-classical" non-linear phenomena were added to Figure 2.4, even though stress-strain or strain-time curves were not defined.

2.5. Vibro-acoustic modulation method

The vibro-acoustic modulation method (VAM) is one of these "non-classical" non-linear acoustic methods. It was introduced in the 90s by Donskoy and Sutin [43–46], and is based on the work of Zaitsev *et al.* [42]. In literature, the method is further referred to as non-linear wave modulation spectroscopy (NWMS) [41], non-linear acoustic modulation (NAM) [47], non-linear Ultrasound Vibro-Acoustic Modulation Technique (NUVAM) [48], and cross-modulated vibro-acoustics (CM/CMVA) [49–51]. VAM in its varieties is the subject of over 200 studies, as shown in Figure 2.5. However, no industrial application has yet been

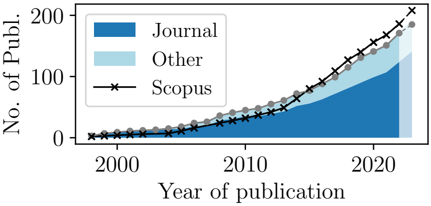

Figure 2.5.: Publications over the years found in a comprehensive literature search, divided between journal articles and other publications. Compared are the results of a Scopus search, where the name variations should be either in the title, abstract or keywords (total Scopus: 208 until 12/2023).

reported. Further evaluations and information on the publications can be found in the Appendix A.1.

The VAM method is based on a so-called “pump-probe” approach, where two dynamic fields are simultaneously applied to the specimen [52]. The general approach is schematically illustrated in Figure 2.6 with the introduced vibrations (left) and the measured resulting signal in the time and frequency domain (right). The *pump wave* is a strong vibration X_p of low frequency f_p, which affects the current stress in the specimen and thus perturbs the material elasticity. This variation is strongest around inhomogeneities or defects in the material. Simultaneously, a high-frequency ultrasonic vibration X_c, commonly referred to as *probing* or *carrier wave*, monitors the elastic and/or dissipative non-linearities of the structure which affect the propagation of the ultrasonic waves [37, 39, 41, 43–46].

Both vibrations differ in amplitude ($A_\mathrm{c} \ll A_\mathrm{p}$) and frequency ($f_\mathrm{c} \gg f_\mathrm{p}$) significantly. In the shown example, the pump vibration X_p is introduced by a hydraulic testing machine, while piezoceramic actuators introduce the carrier vi-

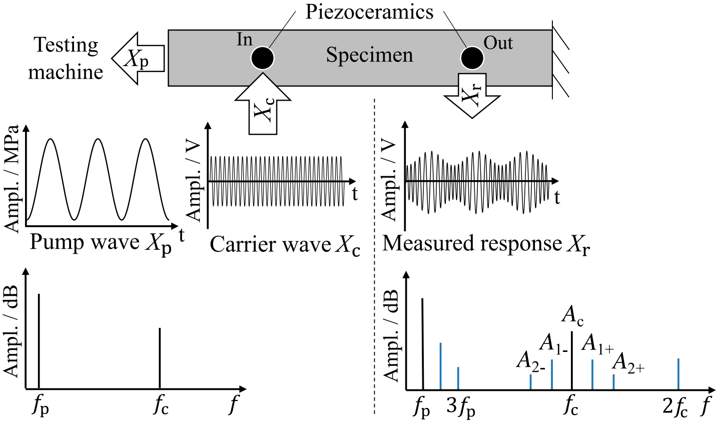

Figure 2.6.: Schematic representation of a vibro-acoustic modulation analysis. Introducing a high-strain pump wave X_p, and an ultrasonic carrier wave X_c of frequency f_c simultaneously results in the modulation of the resulting signal and the formation of sidebands in the frequency domain (lower). The test of a coupon specimen is shown (top), where X_c is introduced by a piezoceramic disk actuator (In) and X_p by a testing machine. The resulting vibration X_r is acquired by a second piezoceramic (Out).

bration X_c. However, the methodology differs in literature and will be discussed later in this chapter. The measured response signal X_r is typically evaluated in the frequency domain, calculated by a Fast Fourier Transform (FFT, denoted as $\mathcal{F}$). $\mathcal{F}(X_\mathrm{r})$ from an ideal linear and undamaged specimen, where the response is measured with ideal equipment, would result in two amplitudes resulting from X_c and X_p, as shown in Figure 2.6 (left). However, a modulation is already present in each actual VAM measurement, even in pristine specimens. This initial modulation results from non-linearities in the specimens, due to the manufacturing process, the measurement equipment itself and effects due to the geometry of the specimens and resulting edge effects. The modulation is visible in the frequency domain by the formation of higher harmonics (kf_p and $kf_\mathrm{c} \mid k \in \mathbb{N}$) from both introduced vibrations and, more importantly for the evaluation of this method, by sidebands around the carrier wave ($f_\mathrm{c} \pm kf_\mathrm{p} \mid k \in \mathbb{N}$). Typically, the amplitudes of the sidebands A_k are compared to the carrier amplitude A_c to estimate the modulation, where k is indicating the frequency of the sideband ($f = f_\mathrm{c} \pm k \cdot f_\mathrm{p} \mid k \in \mathbb{N}$). An increase in the sidebands results from a stronger modulation and, therefore, indicates the formation of damage. Yet, the contribution of the different mechanisms to the resulting modulated signal is still unknown.

The carrier is usually introduced into the structure by applying piezoceramic actuators. However, the excitation of the *pump wave* differs between publications and can be divided into one of three classes. Donskoy and Sutin [53] proposed a differentiation of these classes based on the pump-excitation into the *vibro-modulation* method and the *impact modulation* method. The two classes are accompanied by the utilisation of already present ambient vibrations of the structure, which will be called *ambient-modulation* in the following.

- For the *vibro-modulation* method, a continuous pumping wave with a frequency of f_p is introduced into the structure with an electromagnetic shaker (orthogonal), a hydraulic testing machine (longitudinal) or, in some cases, even a piezoceramic (stack)-actuator. This class is mostly found in the literature.

- The *impact-modulation method*, uses an impact-excitation (*e.g.* an impact-hammer). This method is easily realisable and has advantages in field applications compared to a computationally controlled *vibro-modulation.* However, this method is cumbersome to calibrate and reproduce. Furthermore, the “ring” (i.e. the duration of the vibration introduced by the impact) has to be long enough to resolve the sideband components in the FFT of the measured signal X_r [54].

- For the inspection of large structures, the *ambient-modulation* method is favourable regarding the applicability and installation costs. The ambient vibrations can originate from environmental loads (winds, traffic, etc.) or the circular motion of components (engines, pumps, etc.) [55] and must be significant enough to alter the stress state. The benefit is the energy efficiency since only the ultrasonic carrier has to be excited by the piezoceramics. However, this advantage also results in an undefined low frequency, which might not be constant over time. Therefore, with the traditional evaluation, structural evaluations with this method are cumbersome to reproduce.

Relevant VAM publications are sorted by their type of excitation in Table 2.2. It is evident that especially the pump wave excitation was introduced with several different methods. Alternatively to the usage of piezoceramics, the carrier was also introduced with an air-coupled transducer. The other mentioned excitation methods are modifications to the method like a “Swept sine excitation”, or the “Cross-modulation” where the carrier itself was modulated. VAM has also been applied to various use cases. Pieczonka *et al.* [39] provides an extensive introduction to VAM with a review of the tested materials and promising applications. Additionally, the method was summarised in the book chapters written

Table 2.2.: VAM Literature sorted by the method of excitation. For X_c, deviations from a typical excitation with piezoceramics and relevant changes to the continuous vibro-modulation are shown.

	Variations	Reference
X_c	Swept sine excitation	[56–59]
	Cross-modulation	[49, 51, 60, 61]
	Wide-band excitation	[62]
	Air-coupled excitation	[47, 63]
X_p	Impact modulation	[41, 55, 63–68]
	Testing machine excitation	[69–72]
	Shaker excitation	[55, 66, 73–80]
	Piezoceramic excitation	[81–84]
	Speaker excitation	[85]
	Thermographic modulation	[86]
	Ambient modulation	[87]

Table 2.3.: VAM literature sorted by the application. Additional efforts concerning data reductions and damage localisation are given in the second section.

Application	Reference
Fatigue damage in metal	[55, 69–73, 84, 89–97]
Fatigue damage in composites	[13]
Impact damage in composites	[49, 79, 82, 85, 89, 98–103]
Delaminations and reduced adhesion	[104–109]
Bolt-Loosening	[58, 77, 110–116]
Stone, mortar and Concrete	[31, 51, 68, 80, 83, 117–120]
Bones	[118]
Glass	[121]
Complex geometries	[74, 76, 81, 87]
Pipeline inspection	[75]
Data reduction	[11, 97]
Damage localisation	[47, 82, 84, 86, 89, 122–124]

by Donskoy [54] and Staszewski *et al.* [88]. Additionally, a comprehensive but incomplete list of literature on the various applications of VAM is summarised in Table 2.3. Unfortunately, the majority of VAM-related experiments were conducted on small coupon specimens within a laboratory setting, where both required vibrations (pump and carrier) are introduced as ideal sinusoidal signals with a defined and constant amplitude. Detecting a rotor blade defect on a small wind turbine with a blade-length of 1 m has been the largest reported application, that was found so far [87]. Hence, this summary shows that VAM is still far from an actual industrial applicability.

Many parameters were introduced in the literature to quantify the damage in a VAM experiment. The most popular parameters are the *Modulation index* (MI) [12, 71, 91, 125, 126] which is given in decibels and the “modulation intensity coefficient” (R) [39, 90, 102]. The calculation of the MI and R is given by

$$\mathrm{MI} = 20 \cdot \log_{10}\left(\frac{A_{1+} + A_{1-}}{2 \cdot A_{\mathrm{c}}}\right) \tag{2.2}$$

$$R = \frac{\sum_{k=1}\left(A_{k+} + A_{k-}\right)}{A_{\mathrm{c}}} \tag{2.3}$$

where k again indicates the frequency of the sidebands. Note that in several publications, only the first sidebands are used to calculate R. Consequently, the relevant similarity between the MI and R is the dB scaling. Other proposed parameters, like the “non-linearity parameter” [127, 128], the “sideband ratio” [129] or the “sideband peak count”[130–132], were evaluated in some experiments, but the information gain was minimal compared to the MI of R and, therefore, will be omitted in the following chapters.

The most highlighted benefit of VAM is its sensitivity towards damage detection [54, 69]. Hence, several works were published where the sensitivity of VAM was compared to established baseline-free techniques (in metals), such as ultrasonic testing and eddy-current testing. Donskoy and Liu [133] have performed fatigue experiments on an aluminium coupon specimen where the formation of a crack was observable after 85 % – 88 % of lifetime by ultrasonic and eddy-current testing and visible by eyesight at around 90 %. However, the MI increased significantly at 80 % of fatigue life, demonstrating a superior sensitivity. A study with similar specimens has compared VAM to the acoustic emission testing where the incipient damage detection of VAM was around 80 % as well compared to 85 % of the fatigue life for the acoustic emission measurements [134]. Donskoy and Ramezani [135] have shown a reliable detection and the monitoring from micro-defects to macro-cracks. To detect loosened bolts, Zhang *et al.* [110] could demonstrate an enhanced sensitivity, with additional merits to detect loose multi-type joints and the early stage of bolt loosening. For the evaluation of steel-reinforced concrete, Miró *et al.* [83] have seen an increase in modulation prior to the detection of an open crack. It can be concluded that the non-linear features outperform their linear counterparts in terms of sensitivity, but linear features show advantages in noise tolerance and hence increased practicability [136].

A theoretical explanation of VAM was given by Lim and Sohn [127], in which several necessary conditions for a modulation were derived for the occurrence of a modulation in the measured response signal. These relevant conditions for the detection of fatigue cracks in metallic specimens are the following:

- The “Crack perturbation condition” requires the strain at the crack location to be oscillated by both vibrations. This condition is always met in a transient wave propagation (*e.g.* found for an impact modulation), as the propagating waves constantly perturb the crack’s strain. In stationary resonant vibrations, where a piezoceramic actuator or electromagnetic shaker introduces the pump wave X_p, non-linear modulation does not occur when the crack coincides with a node where the wave modes have a minimum (zero) amplitude.

- The “Mode matching condition” requires the motion of the crack that is induced by one of the waves to modulate the other at the crack’s location. For instance, if a low-frequency shear horizontal wave (with no change in x and some change in y) and a high-frequency longitudinal wave (with no change in y and some change in x) travel through a crack oriented perpendicular to their direction (in the z-direction), the low-frequency shear horizontal wave makes the crack surface move in the y-direction (friction, crack mode II). This motion does not affect the high-frequency longitudinal wave or create modulation because they move in different directions. Therefore, the generation of modulation depends on the selection of two input frequencies and various factors, including the location and alignment of the crack and operational conditions, such as the loading of the structure.

However, the same work indicated that complying with these necessary conditions does not guarantee a successful application of VAM. In addition to the mentioned conditions, Li *et al.* [137] suggested that especially the frequency of the carrier vibration should be chosen to excite lamb waves, but only of the fundamental S_0 and A_0 modes. Further information and the preconditions for Lamb waves can be found in Chapter A.2 of the Appendix.

While the fundamental concept of VAM—the simultaneous excitation of two vibrations—appears relatively straightforward, the governing non-linear material responses and the underlying physical mechanisms remain poorly understood [41, 71, 123]. Despite the formulation of the binding conditions combined with several mathematical and physical descriptions available in the literature [127, 129, 138–141], a full explanation and, more crucially, the prediction of the initial modulation in any given structure remains unsolved. Consequently, to ensure comparable VAM results, the specimens need to be nearly identical, as even slight differences result in deviations of the initial modulation [142]. Moreover, the intensity of modulation is highly contingent on the carrier frequency (f_c). Due to factors such as resonances within the structure, altered wave propagations, reflections, and mode conversions, the MI can fluctuate significantly (over 40 dB) for different carrier frequencies f_c [133]. Hence, it is often suggested to average the results of VAM over a specific frequency range. Donskoy [54] advises evaluating $30 - 100$ frequencies for a reliable result, which makes the method rather time and computationally expensive.

Several studies have indicated that the observed modulations in VAM measurements of actual specimens represent a combination of amplitude modulations (AM), phase modulations (PM), and frequency modulations (FM), which result from the periodic changes due to X_{p}. Consequently, the differentiation of the measured signal into distinct modulation types has demonstrated advantages in the damage evaluation since they could be linked to various types of damage within a specimen [91, 126, 135]. Hu *et al.* [91] proposed the separation of the modulation types using the *Hilbert-Huang transformation* and suggested that AM exhibits a stronger correlation with crack size. However, it was stated by Donskoy and Ramezani [135] that applying the *In-phase Quadrature Homodyne Separation* algorithm allows for a more precise damage classification than the *Hilbert-Huang transformation*. In the study, structural contacts and large cracks resulted primarily in AM, while the initial stage of fatigue damage primarily resulted in FM. Oppermann *et al.* [97] have shown that the short-time Fourier transform (STFT) is suitable for differentiating between the AM and PM, even on low-powered devices. They have further pointed out that neither of the previously mentioned algorithms can differentiate between FM and PM. Hence, in their work, the resulting angular modulation (PM and FM) is denoted as PM, which will be adapted in this thesis from here on. Note, that a mathematical description of the types can be found in Chapter A.3. The proposed application of the STFT [57, 97, 143] and wavelet transform spectrogram methods [144, 145] are constrained by their suitability for analysing VAM-Chirp signals with pump waves of relatively high frequencies, typically exceeding hundreds of Hz. However, load-induced ambient vibrations (e.g., bridge traffic) correspond to the structure's resonance frequencies, which generally are significantly below 100 Hz [142]. At the Köhlbrandbrücke in Hamburg (Germany), vibrational data show the strongest ambient vibrations in the frequency range of 10 – 20 Hz [97, 146].

The VAM method—as typically described—requires the ultrasonic carrier signal X_{c} and the pump vibration X_{p} to remain consistent during the measurement and, more importantly, to have the same amplitude in subsequent measurements. This demand results in one of the biggest challenges concerning the industrial application of VAM. Ideally, at larger structures, the already present ambient vibration is utilised as pump vibration to prevent the installation of many low-frequency actuators, which must be powered and maintained. However, these ambient structural vibrations are influenced by many environmental factors such as temperature, winds, and in-service loads like traffic. Consequently, the eigenmodes and dominant frequencies within the structure fluctuate, affecting the modulation and hindering the applicability of VAM.

Furthermore, structural boundary conditions significantly influence the resulting modulation of a signal and the sensitivity of VAM. Exemplary, the clamping force applied by a testing machine can have a notable impact on the modulation's intensity in laboratory experiments [49]. Several studies have consequently opted to suspend specimens using threads [66, 67] or springs [124] to minimise the influence of these boundary conditions. Nonetheless, even in cases where specimens were suspended using threads, Duffour *et al.* [66] encountered challenges when attempting to validate the suggested high sensitivity of VAM.

Considering all these factors, the evaluation of VAM is a complex endeavour. Furthermore, analogous to the non-linear contribution in the frequency spectrum of the higher harmonics—presented in Figure 2.4—these patterns also affect the VAM sidebands. Hence, defects contribute differently to the measured modulation, which is a combination of all influences. Consequently, evaluating just the first sidebands may not result in a precise detection or identification of damages. Thus, a data-driven analysis using machine learning algorithms to "learn" and evaluate correlations and characteristic patterns of the sideband amplitudes seems beneficial for the highly correlated and complex input data.

The development of data-driven models can be classified into two main categories:

- Supervised Learning: Data from both damaged and undamaged structures are given with the corresponding *label*. The data and the labels can be utilised to identify a pattern to map from the data to the *label* and assess unknown data with the trained model.
- Unsupervised Learning: The data represents the state of a material or specimen and is available in a structured format. Unsupervised learning techniques, such as statistical methods or machine learning algorithms, are used to identify deviations (outliers) and to group data points (referred to as samples in this thesis) into clusters.

The supervised learning algorithm can be further categorised into the *classification* and the *regression*, based on the type of the provided label (a finite set of classes vs numerical values). The application of data-driven evaluations was already proposed for evaluating lamb waves [147–150] and many other NDT methods, as summarised by Harley and Sparkman [151]. Machine learning methods are furthermore essential for the creation of SHM systems, which can be categorised into the mentioned groups based on the available data [5].

Applying machine learning or ANNs to VAM measurements was first suggested by Lim *et al.* [128], for the evaluation of the crack length in aluminium specimens and consequently, the remaining lifetime, based on the number of fatigue cycles and the “nonlinear parameter” β. This approach was improved by Miele *et al.* [120], who used physics-informed machine learning models for damage localisation in concrete structures based on several pre-determined values from a VAM measurement. Finally, the reduction of spectral noise and data size using a long short-term memory network was proposed by Jang *et al.* [152], where the signal-to-noise ratio could be improved by 175% by using only 20% of the original data. However, it has to be noted that the pump wave ($f_\mathrm{p} = 84\,\mathrm{kHz}$) was excited by a piezoceramic actuator. Since X_r was measured for 0.1 s at a sampling rate of 1 MHz, still a signal of 10^5 measured points are required.

Furthermore, the possibility of a damage localisation with a VAM measurement was addressed. The damage localisation is challenging due to the dispersive and multimodal nature of the propagating guided waves combined with the continuous excitation in most VAM experiments [84]. However, there were several studies with promising results. The approaches range from scanning of the structure by laser vibrometers [76, 82], infrared cameras [86], moved air-coupled transducers [47] and the application of sensor networks. In a sensor network, it was shown that the damage indices are higher on the sensors in the proximity of the damage [123, 140]. Additionally, the location can be calculated from the propagation path of the modulated responses if the shape of the specimen is known [84, 124]. However, it is essential to note that these localisation techniques were demonstrated primarily on thin plates or coupon specimens. The applicability at more intricate structures still needs to be verified. Nonetheless, the VAM method may offer a potential solution for detecting and localising damages in such complex structures.

3. Materials and methods

Throughout this thesis, several experiments were conducted on various specimens. This chapter provides an overview of the used materials, the manufacturing processes, and the applied experimental techniques. Hence, describing the same manufacturing or testing procedures in the following chapters is minimised. The focus of this thesis is the application of VAM on fibre-reinforced composites. Consequently, the following chapters will mention only the layup, laminate thickness, and specimen dimensions. However, the enhancements developed for the VAM methods were additionally validated on metallic specimens. Additionally, Chapter 5 will discuss two large-scale specimens to test the sensitivity of VAM.

3.1. Manufacturing

The tested GFRP coupon specimens were manufactured using a vacuum-assisted resin transfer moulding (VARTM) process. As reinforcement, dry unidirectional (UD) E-glass fabrics (UT-E500 with $500\,\mathrm{g/m^2}$, Gurit) were used to manufacture the laminate. The fabrics are stacked in a desired sequence and placed into a mould made from aluminium.

The aluminium mould consists of two halves separated by a frame to form a rectangular and flat cavity. The frame defines the cavity and, consequently, the final plate's dimensions, thickness and proportion between the volume of fibres and matrix material. Before using the mould, it is essential to apply a release agent (Mikon W-64+, Münch Chemie) to all surfaces that need to be separated to guarantee a demoulding without damaging either the mould or the plate. The stacked fabrics in the frame were surrounded by 2 cm of fleece material to prevent any channelling of the resin between the stacked fibres and the frame.

For the infiltration, the mould is closed and fixated with surrounding screws. Any deformation is minimised by inserting the mould inside a heating press and applying a clamping force of 20 kN. Due to an applied vacuum on one side and by pressurising the resin with 2 bar on the other side, the fibres were infiltrated with a 2k low-viscosity epoxy resin (RIMH 135 + RIMR 137, Hexion). Increasing the temperature of the mould to 50°C reduces the viscosity of the matrix and improves the infiltration process. Afterwards, the plates were cured for 16 h at 50°C in the mould with the pressure still applied. Additionally, a post-curing in an oven (8 h at 80°C) without the mould results in the complete cross-linking of the matrix material. The finished plates are expected to have a fibre volume fraction of around 50 %.

Finally, the plates were cut into specimens of the desired dimensions, using an *ATM Brilliant 265* CNC-saw (ATM Qness GmbH) with a 2.2 mm thick corundum blade. The cut surfaces were polished with 1000-grit sandpaper to reduce crack initiations due to surface roughness from the saw blade.

3.2. Experimental methods

The experimental procedures can be divided into the mechanical testing of the specimen and the vibrational analysis.

Several quasi-static tensile tests were performed to evaluate the modulus and the ultimate strength of the specimens. For bonded specimens, the shear strength was determined. All these tests were conducted on a Z100 universal testing machine (ZwickRoell) equipped with a 100 kN load cell, as shown in Figure 3.1 (left). The machine features hydraulic clamps and an automatic strain measurement system with an extensometer (multiXtense) to acquire the true elongation. This extensometer uses an automatic centring of the sensor arms, which were attached to the specimens at a distance of 50 mm. The displacement rates were chosen to comply with the respective test standards. Stress values were calculated based on the initial cross-section of the specimens or the overlap of the adhesive joints.

All VAM-related experiments in this thesis (except a GFRP cuboid presented in Chapter 5.6.2) were performed on uni-axial servo-hydraulic testing machines. Depending on the load level of the experiment, either a machine with a 40, 63 or 100 kN load cell was used. Exemplarily, the one with the 63 kN load cell is shown in Figure 3.1 (right). All these servo-hydraulic testing machines were manufactured and maintained from *Instron* and controlled by the WaveMatrix$^{\text{TM}}$

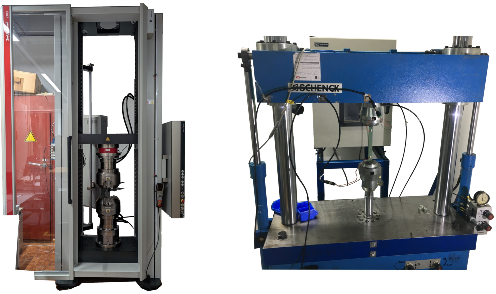

Figure 3.1.: Universal testing machine Z100 (left) and servo-hydraulic testing machine with a 63 kN load cell (right), used in the experiments.

software. The machines can test statically and dynamically with a maximal frequency of approximately 10 Hz in the load range of the VAM experiments. Due to the different material properties, failure mechanisms, geometries, and specimen types in this thesis, individual testing strategies were defined for each experiment.

3.3. Vibro-acoustic measurements

The vibro-acoustic measurements of this thesis are similar to a methodology described in many works [12, 70, 74, 97, 126, 135]. The tested coupon specimens are clamped on two sides into the previously mentioned servo-hydraulic testing machines to introduce the pump vibration X_p with a frequency f_p of 5–10 Hz. This frequency range was chosen, as it is typical for the ambient vibrations of many industrial structures. Note that the hydraulic gripping force is held constant for each specimen to eliminate possible influences as pointed out by Aymerich and Staszewski [98]. The introduced pump vibrations are defined in the following by its frequency f_p, the maximal stress σ_max and the stress ratio R_σ, which is defined as:

$$R_\sigma = \frac{\sigma_\mathrm{min}}{\sigma_\mathrm{max}} \tag{3.1}$$

and R_σ is typically chosen as 0.1 for tests in the tension-tension regime or $R_\sigma = 0$ if the minimal stress is at neutral stress state, to prevent buckling of coupon specimens.

The *carrier wave* X_c of all VAM tests was introduced into the specimens by piezoceramic actuator disks. Disks with a diameter of 10 mm and a thickness

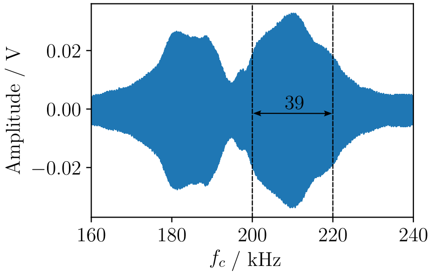

Figure 3.2.: Selection of frequency range, based on the amplitude of the measured signal strength. The carrier range between $f_\mathrm{c} = 200 - 220\,\mathrm{kHz}$ was chosen and subdivided into 39 measured frequencies.

of 2 mm (PIC255, PI-Ceramics) was used in all experiments due to their radial resonance of 200 kHz. If not specified otherwise, the disks are bonded to the structure with double-sided tape (56172, Tesa). Using the double-sided tape offers the reusability of the piezoceramics for subsequent measurements. However, the low stiffness of the tape reduces the signal strength, compared to bonding the piezoceramics with a dedicated thermosetting adhesive. With sufficient excitation voltage at the piezoceramics, the reduced signal strength and consequently the increased signal-to-noise ratio can be compensated. A NI-USB 6366 data acquisition board (National Instruments) with two signal generators and eight measurement channels is used to drive the piezoceramics and acquire the system response. The response signal X_r can be recorded with a sampling rate of 2 MS/s and a 16 bit resolution. The arbitrary waveform generator provides voltages with a maximum of ±10 V. Furthermore, the signal is amplified twofold in all experiments by a BUF634 amplifier, with a built-in low-pass filter of 420 kHz. As indicated in the literature, measuring the structural response of VAM for several frequencies is recommended. In this work, the range with the highest signal strength is chosen, based on a chirp signal, where the frequency of a sinusoidal signal is linearly swept between $1 - 300\,\mathrm{kHz}$ within 10 s. The resulting amplitude over the carrier frequency as a linear structural response is illustrated in Figure 3.2 for one of the adhesive bonded single-lap shear specimens from Chapter 4.1. The chosen frequency range is divided into distinct frequencies, measured for all specimens of the designed experiment. Note, that all signals were multiplied with a Hanning-window, to ensure the periodicity and increase the precision of each measurement, as elaborated further in Chapter A.4 of the Appendix.

4. Bond line evaluation in joined structures

VAM-related research primarily focuses on an application for SHM, while its high sensitivity in detecting micro and meso-damage is often emphasised [74]. However, a significant limitation arises due to the necessity of a baseline measurement, as the resulting modulation greatly depends on several factors such as (1) the location of the actuating piezoceramic, (2) the placement of the receiving piezoceramic, (3) the characteristics of the material, and (4) the geometry of the tested structure or specimen.

First studies of Vehorn [153] or Donskoy and Liu [133] have explored baseline-free VAM approaches. Nevertheless, a viable solution to apply piezoceramic to an unknown structure and assess its current damage state using the VAM method—as possible with most traditional NDT methods—has not yet been achieved. While this limitation is acceptable for SHM applications, where the initial state of the structure is typically assumed to be *pristine* and changes in signals are evaluated, it presents a significant drawback for the applicability of VAM as an NDT method. However, when evaluating several similar specimens, such as in a production line, it is assumed that the required baseline for the VAM evaluation can be taken from the other tested specimens.

4.1. Detection of adhesion defects

FRPs are utilised for their lightweight properties, especially in structural members. Prominent examples include aircraft structures, blades of wind turbines, sailing boats and many more. In contrast to the principle of lightweight design, especially aerospace structures are still bonded with traditional mechanical methods like bolts and rivets. The resulting stress concentrations at the fasteners have to be counteracted with thickened material or metal inserts [154]. In contrast, adhesive bonding reduces this extra weight due to uniform stress distributions in the joint [154, 155]. Nevertheless, despite automated bonding processes and rigorous controls, contaminations, application errors, or improper surface preparation persist, resulting in areas with reduced adhesion and, consequently, a dramatically reduced bond strength [29, 154–157].

While techniques like ultrasonic testing can detect voids and porosities in adhesives, weak bonds result from atomic-level chemical interactions, which are much smaller than ultrasonic wavelengths [156]. Therefore, conventional NDT methods cannot detect these areas reliably [155, 157, 158].

The weak bonds are typically artificially recreated in literature by inserting non-adhesive films [129, 159–164] or by contaminating the surface of the adherent [129, 163–169]. However, inserting a non-adhesive film like polytetrafluoroethylene (PTFE) into a joint alters the physical properties locally due to interfaces, allowing the detection with ultrasonic testing and other NDT methods [129, 159, 163]. More challenging for the detection, and closer to the real weak bonds is the contamination of the adherent with a small amount of release agent [168].

The NDT of bond line flaws was addressed in literature, applying linear and non-linear ultrasonic methods [156, 163, 164, 170], guided Lamb-waves [160, 171, 172], X-ray [159], digital image correlation [173] and laser shock adhesion testing [165, 174]. A general overview is given by Ehrhart *et al.* [155] and Ramalho *et al.* [29] are focusing on lamb waves for the evaluation of adhesive bonds. However, the existing methods and current research are not mature enough to meet the standards (*e.g.* the Federal Aviation Regulations Section 23.573(5)—(iii) [175]). Hence, no NDT method is currently approved by the Federal Aviation Authority to reliably evaluate adhesive bonds, emphasising the demand for precise and reliable approaches [154, 157, 158, 176].

As already summarised in Chapter 2.5, VAM has shown a superior sensitivity to damages in many applications compared to other non-linear methods, as summarised by Donskoy *et al.* [55] and Pieczonka *et al.* [39]. It was further indicated (see Chapter 2.5) that many influences on the modulation and, consequently, the sidebands in the frequency spectrum exist.

4.1.1. Single-lap shear bond manufacturing

To overcome the challenges, 33 single-lap shear specimens were produced in a secondary bonding process. The dimensions of the specimen follow the ASTM D5868 - 01 [177] standard and are given in Figure 4.1.

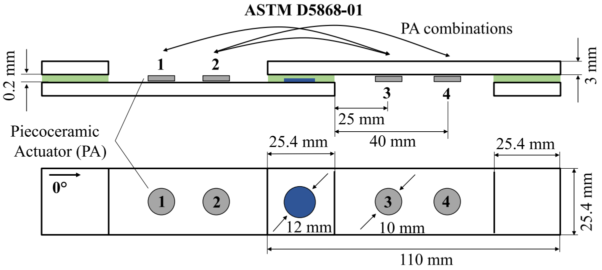

Figure 4.1.: Specimen dimensions after ASTM D 5868 - 01 with the locations and size of the introduced contaminations and the location of the piezoceramic and the measured combinations.

For the substrates, three GFRP plates were manufactured as $[0_4]_s$ layup from UT-E500 glass fibres, according to the definitions in Chapter 3.1. This UD laminate was chosen to prevent influences of the mode conversation by angled plies, as described by Mook *et al.* [178]. The matrix material is the low-viscosity epoxy system (RIMR 135 and RIMH 137). After curing, the plates were cropped into 110 mm wide stripes to manufacture several specimens simultaneously. The whole manufacturing process is illustrated in Figure 4.2. Prior contaminations on the bond lines were eliminated by finishing the area with 1000-grit sandpaper and cleaning the bonding areas with isopropanol.

Three classes of single-lap shear bonds were manufactured, including pristine bonds and two types of bond line flaws. During the manufacturing, circular areas (diameter of 12 mm) in the centre of the bonds were contaminated with release agent (Mikon W-64+), similar to the weak bond creation from Harder

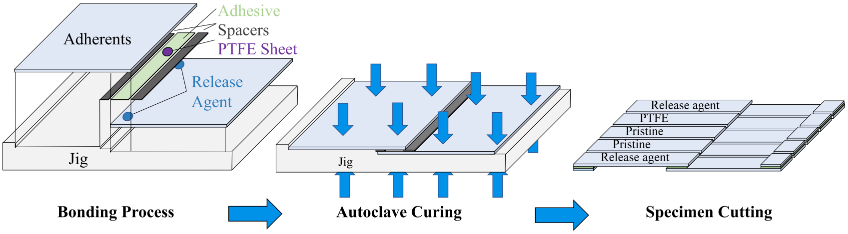

Figure 4.2.: Illustration of the manufacturing process and the creation of artificial defects (left), the curing process with the mould in an autoclave (middle), and cutting the plates into the final specimens (right).

et al. [168]. Stencils (Hostaphan cut on an Aristomat TL 1625) ensured a precise application and protected the remaining area from further contamination. The second class of defects result from inserted circular PTFE films (Goodfellow FP301100) with a thickness of 0.01 mm and an identical diameter compared to the contaminations. The films were cut on the router as well.

The epoxy adhesive (SikaPower-1280) used for the single-lap shear bonds is commonly applied on GFRP wind turbine blades. The bond line thickness of 0.2 mm was ensured by spacers, which were positioned relative to the substrates in a milled jig. The produced panels were cured in an autoclave for 4 h at 70 °C with a pressure of 2 bar and afterwards cut to their width of 25.4 mm on the CNC-saw (cf. Chapter 3.1). Finally, all specimens were conditioned for two weeks according to ISO 291 at 23 °C and 50 % relative humidity. The manufacturing of the plates and the adhesive bonds were evaluated, using an optical examination (EPSON V850 Pro transmission light scanner) and measurement of bonded regions of the single-lap specimens with pulse-echo ultrasonic (USPC 3040 ultrasonic imaging system) evaluated as C-scans.

4.1.2. Data acquisition and processing

All measurements on this specimen were performed according to the description in Chapter 3.3. The pump wave was introduced by a hydraulic testing machine with $\sigma_{\max} = 11\,\mathrm{MPa}$, a stress ratio of $R_\sigma = 0.1$ and a frequency of $f_\mathrm{p} = 5\,\mathrm{Hz}$. Based on the signal strength over the frequency, a range of $f_\mathrm{c} = 200 - 220\,\mathrm{kHz}$ with a spacing of 0.5 kHz was chosen for the carrier excitations. Hence, these 39 VAM measurements were performed for a duration of 2 s at each of the three signal pathways between the piezoceramics, as indicated in Figure 4.1. Note, that for each pathway, the measurements were performed in both directions, to determine if certain locations of the piezoceramics are superior to others. Consequently, a total of 234 VAM measurements were acquired at each of the specimens (39 frequencies at 3×2 signal pathways).

The data preparation and processing is shown exemplarily in Figure 4.3 ($f_\mathrm{c} = 210\,\mathrm{kHz}$, $f_\mathrm{p} = 5\,\mathrm{Hz}$ and $f_\mathrm{s} = 2\,\mathrm{MSa/s}$). The measured signal in the time domain (Figure 4.3, top-left) is transformed into the frequency domain with the fast Fourier transformation (FFT). Only the steady-state signal (after 0.4 ms) is used to further reduce the spectral leakage and highlight the sidebands. For each excited carrier frequency f_c at every specimen j, the amplitudes of the carrier

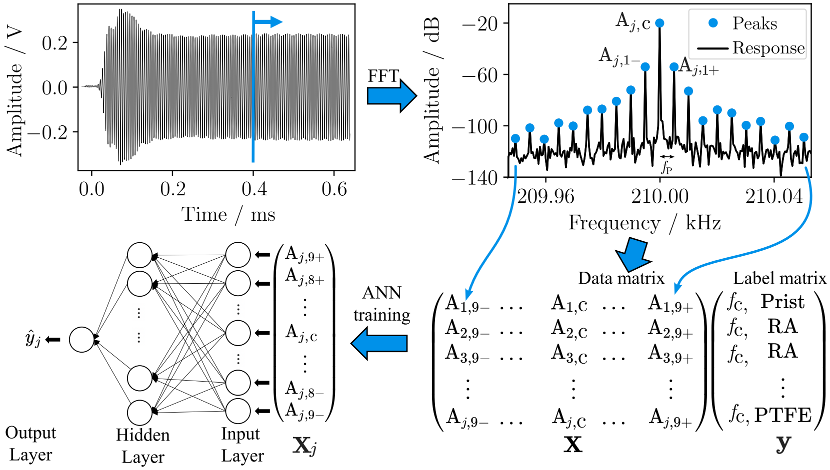

Figure 4.3.: Schematic of the data-driven evaluation of VAM: The measured signals are converted in the frequency domain with the FFT. The amplitudes of the sidebands and the carrier are extracted and used to train the neural networks. The corresponding labels (Prist, RA and PTFE) represent pristine specimens, contaminated specimens with release agent and specimens with inserted PTFE sheets.

$A_{j,\mathrm{Ca}}$ and nine sidebands on each side $A_{j,i\pm}$ (all blue dots of Figure 4.3 top right) were extracted and combined into a matrix $\mathbf{X}$ for further evaluations. The respective specimen class (pristine, release agent contamination, PTFE film) and the specimen's shear strength are stored as labels in the vector $\mathbf{y}$ together with a specimen identifier. One additional dataset was created similarly to the data matrix $\mathbf{X}$, where the signals (Figure 4.3, top left) were evaluated with the STFT algorithm to extract the AM and the PM separately. The procedure for the AM-PM separation was adapted from Oppermann *et al.* [97]. Hence, a second matrix $\mathbf{X}_{\mathrm{APM}}$ was created from both extracted parameters. It can be assigned to the same label-matrix $\mathbf{y}$.

4.1.3. Machine learning application

Based on the created data sets, machine learning models can be applied for a classification or regression of the samples. Note that the term “samples” is used as synonym for the individual VAM measurements, used to predict the bond quality. Hence, in the following chapters, artificial neural networks (ANN) are trained for the classification of the specimen classes (Prist, RA and PTFE) and the regression of the resulting shear strength of the adhesive bonds. Both approaches were realised by training two ANNs with minor adaptations. The training process was implemented in `Keras` 2.3 [179] which is referencing to `TensorFlow` 2 [180] in a `Python` 3.7 environment. The network architecture and learning parameters for both datasets were optimised by conducting a randomised grid search [181], where combinations of the number of hidden layers (ranging between 1 and 4) and the number of neurons per layer were tested. For the training of an ANN on the data set $\mathbf{X}$, the number of sidebands used as input values (as given by the input vector $\mathbf{s}_j = [A_{j-}, \ldots, A_{\mathrm{Ca}}, \ldots, A_{j+}]$ in Figure 4.3) were varied as well. Note that $\mathbf{X}_{\mathrm{APM}}$ consists of only two columns and was not altered. Furthermore, for all datasets, the signal pathways between the piezoceramics and the range of included carrier frequencies were varied, shuffled and permuted in a randomised grid search. The information-gain of the ANN by adding more sidebands is evaluated. Additionally, frequency ranges which allow a precise classification can be identified. Finally, the different signal pathways between the piezoceramics were evaluated regarding the prediction of the bond quality and the resulting shear strength.

The precision of the ANNs was evaluated by the classification *accuracy* and the *mean absolute error* (MAE), which are calculated as

$$\mathrm{accuracy}(\mathbf{y}, \hat{\mathbf{y}}) = \frac{1}{n}\sum_{i=1}^{n} 1_{y_i}(\hat{y_i}) \quad \text{and} \quad \mathrm{MAE}(\mathbf{y}, \hat{\mathbf{y}}) = \frac{1}{n}\sum_{i=1}^{n} |\hat{y_i} - y_i|. \tag{4.1}$$

The index i runs over the number of predicted samples n. Both metrics compare the true label y_i and the predicted label $\hat{y_i}$ for each sample in the prediction and $1_{y_i}(\hat{y_i})$ is the indicator function which returns “1” if the predicted label corresponds to the true label.

Due to several measured signal pathways and the wide frequency range, the ANNs were trained on subsets of the dataset. Hence, specific combinations of piezoceramics (*e.g.* all measurements from Position 1 → Position 3 and Position 1← Position 3 denoted as P1↔P3) at distinct frequency ranges (*e.g.* $200 - 205$ kHz) were used. By employing a ten-fold cross-validation, where ten ANNs are trained on differently composed training sets, the robustness and reliability of the predictions are ensured. If not otherwise stated, the data set is split randomly into a training set (80 %) and a test set (20 %). Hence, each shown result averages ten ANNs, which were trained on dissimilar training sets. It was furthermore ensured, that all measurements from one specimen belong either to the test or the training set to assure reliable predictions.

The ANNs used for classification and regression differentiate mainly in the output layer and, consequently, the applied loss-function. For the classification, a softmax output-layer[1] was applied, and a single output neuron[2] was used as the output of the ANN for the regression. Also, a standard scaling[3] of the measured amplitudes, improved the optimisation in the training process of the ANN (Z-score normalisation). Over-fitting of the ANNs was reduced by including the *dropout* of neurons in the training process with a probability of 10 % for every hidden layer and the *early stopping* of the training process at the smallest error [183], with a delay of 100 epochs on the validation loss. Based on the randomised-grit search for optimal hyperparameters, the neural network architecture was set to four hidden layers with a minimum of [40,40,30,20] neurons.

4.1.4. Recursive feature importance

In this study, the impact of each sideband on the prediction is evaluated to determine their individual significance. To achieve this, the feature importance of each input is calculated by two different methods.

Shapley values, which are used in the cooperative game theory, are calculated with the DeepExplainer from the SHapley Additive exPlanations (SHAP) package [184]. These values quantify the average contribution of each feature coalition (input) to the model's prediction. By considering all possible feature combinations, Shapley values measure the average importance of a feature across different subsets of the data [185]. Generally, large absolute Shapley values indicate high relevance to the predicted values and, therefore, signify greater feature importance.

The results obtained from SHAP are compared to those from Garson's algorithm [186, 187], which analyses the weights of a trained neural network to determine the importance of input features. Due to variations in feature importance across the ten different cross-validation runs, the mean value is calculated and used for the comparison.

---

[1] categorical cross-entropy loss, Adam optimiser [182] with an initial learning rate set to 0.01

[2] ReLu activation, mean squared error loss, Adam optimiser with an initial learning rate set to 0.0001

[3] The standard scaling results in the sideband amplitudes to have a mean value of zero combined with a standard deviation of one.

4.1.5. Mechanical testing

The shear strength and modulus of each single-lap shear specimen were tested on a universal testing machine (*cf.* Chapter 3.2). In contrast to the specifications of the ASTM D5868-01, the displacement rate was set to 2 mm/min to account for the small fracture strain of the adhesive bonds. Figure 4.4 shows a comparison of the results for the specimen class. Intuitively, the pristine specimens exhibit the highest shear strengths, measuring 22.3 ± 1.5 MPa, which is close to the 25 MPa specified in the datasheet of the adhesive.

In the presence of contaminants, the shear strength is reduced to 20.7 ± 1 MPa, and PTFE films reduce the shear strength further to 19.7 ± 0.9 MPa. Although the standard deviations of these two measurements are similar, it is hypothesised that the stress concentration resulting from the finite thickness of the PTFE film contributes to the reduced shear strength, compared to the release agent which reduces the adhesion significantly. Furthermore, the reduction in shear strength due to the release agent in this study is only half as severe as the 26 % decrease observed in scarf-bonded joints tested by Harder *et al.* [168]. This difference can be attributed to the stress concentrations at the edges of single-lap shear joints, compared to the more uniform stress distribution in scarf-bonded joints. No significant differences were observed in the shear modulus of the contaminated specimens. Corresponding stress-strain curves can be found in Figure A.6 of the Appendix.

The typical fracture surfaces and ultrasonic C-scans of the three different classes are compared in Figure 4.5. The applied release agent and inserted PTFE films are identifiable as circular areas, without any adhesive remaining on the surface. Consequently, no cohesion defects of the adherents occur in these areas.

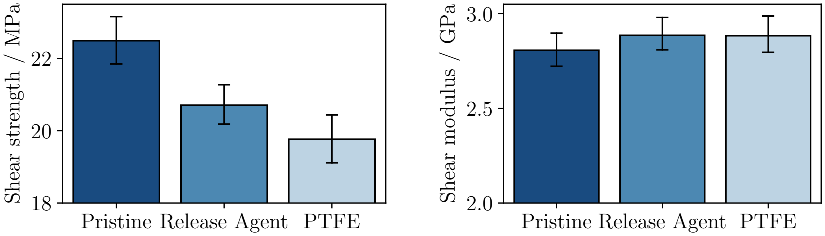

Figure 4.4.: The averaged shear strengths (left) and shear modulus (right) of the different classes of adhesive joints.

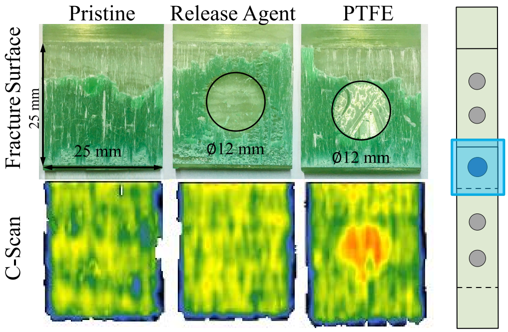

Figure 4.5.: The fracture surfaces of all three bond classes (upper) are compared to the respective ultrasonic C-scan of the overlapping bond regions. Only the PTFE sheet is observable in the C-scan.

Additionally, around the contaminations, minor fibre tear failures are observed regardless of the specimen type. However, in the compared C-scans, only the PTFE films are distinguishable in the bonding region. It can be concluded that the created weak bonds are realistic and reduce the shear stress. However, they are not detectable with conventional NDT methods.

4.1.6. Vibro-acoustic measurements

The vibro-acoustic measurements are initially assessed by calculating the MI as a "traditional" evaluation, described in Chapter 3.3. Additionally, the AM and PM components of the signal are extracted, following the approach described by Oppermann *et al.* [12]. The box plots in Figure 4.6 display the distributions of the three damage indices. Indicated by the position of the median value, especially the MI and the AM, would eventually enable the detection of the inserted PTFE film for most measured signals. However, distinguishing between pristine and release agent specimens is not possible. The interquartile range of both specimen classes overlaps regardless of which damage parameter is evaluated. Nevertheless, the median MI and PM of the contaminated specimens with release agent are slightly higher compared to the pristine specimens and lower at the evaluated AM. These slight differences could indicate patterns in the signal, which require a thorough separation of the defects or the implementation of a data-driven approach. The significant difference observed for PTFE aligns with

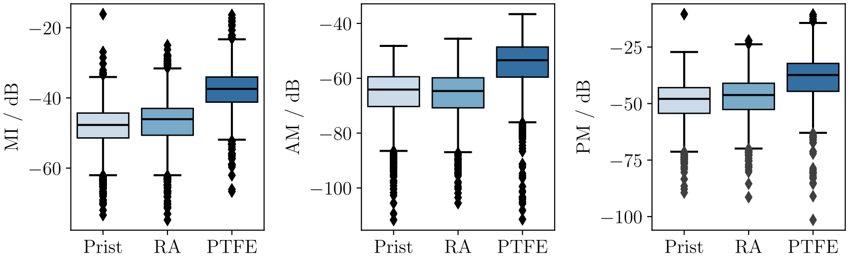

Figure 4.6.: Modulation index of the measurements (left) compared to the amplitude modulation (centre) and the phase modulation (right) for all three classes. Note that "RA" corresponds to the release agent contaminations.

the findings of Chen *et al.* [129], where a PTFE film was detectable within a laminate using VAM measurements.

4.1.7. Adhesive bonding classification

To classify the specimens, a more sophisticated defect detection is proposed in the following by utilising ANNs trained on both datasets $\mathbf{X}$ and $\mathbf{X}_{\mathrm{APM}}$. Due to the different input values, the network geometry is altered as well. As already mentioned, the influence of the number of evaluated sidebands, smaller ranges of the carrier frequencies f_{c} and the different signal paths between the piezoceramic actuators were assessed. For these variations, the frequency range was randomly selected from the measured interval of $200 - 220\,\mathrm{kHz}$ to consist of at least five values. Additionally, the number of sidebands as input to the ANNs trained on $\mathbf{X}$ was varied. Finally, ten ANNs are trained on this selected data set as a 10-fold cross-validation to additionally test the robustness of the process.

Prior tests have resulted in the most accurate prediction on the dataset $\mathbf{X}$ with a network architecture of four hidden layers with $[40, 60, 40, 30]$ neurons. This architecture will be denoted as $\mathrm{ANN}_{\mathrm{SB}}$[4] in the following. The network architecture of $\mathrm{ANN}_{\mathrm{APM}}$ for the bonding classification—based on $\mathbf{X}_{\mathrm{APM}}$—is significantly smaller due to the reduced number of input parameters. The architecture consists of just eight neurons in one hidden layer. More extensive architectures have resulted in *overfitting* of the network and ultimately worse predictions, despite the application of *dropout* and *early-stopping*.

---

[4] Since the network was trained on the actual sidebands, it is denoted as "SB"

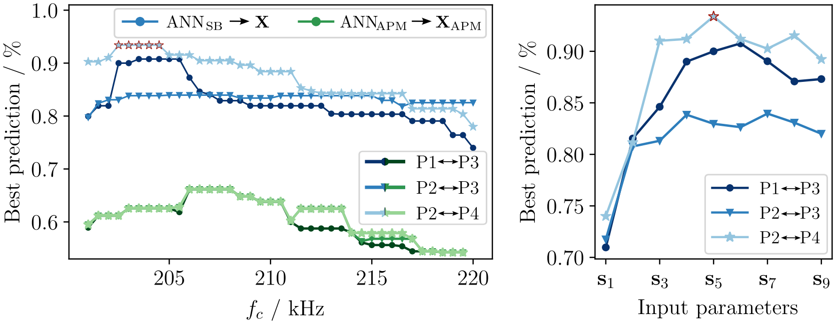

Figure 4.7.: Most precise classifications of the bond line defects over the carrier frequencies. The results from the different signal pathways between the piezoceramics and ANNs trained on the different datasets are compared (left). The accuracy of ANN$_{\mathrm{SB}}$ depends on the number of sidebands $\mathbf{s}_j$, used as input for the training, as shown by the maximal achieved accuracy of this input-combination (right).

The most precise classifications are shown in Figure 4.7 (left) over the carrier frequency for the three tested signal pathways and both datasets. Each point represents the averaged accuracy over the ten-fold cross-validation of different test/train compositions (with a ratio of 20/80). Note that in Figure 4.7 (left), different ranges of the carrier frequency were used to train the ANNs and that these ranges overlap, instead of individual frequencies. Consequently, each dot in Figure 4.7 (right) represents the highest averaged accuracy over the cross-validated ANNs, trained on input data including this particular frequency.

When comparing the accuracy of both datasets, a significant difference is observable. The smaller ANN$_{\mathrm{APM}}$, trained on the extracted AM and PM, reaches a maximal accuracy of 69 %. The accuracy of different signal paths overlaps at many frequencies and affects the predictions only in certain frequency areas. On the other hand, the ANNs trained on the actual amplitudes of the sidebands (ANN$_{\mathrm{SB}}$ trained on $\mathbf{X}$), resulting in more precise classification accuracies. These observations result from two causes. Firstly, the STFT compresses and neglects essential information in the signal. The STFT assumes, that the signal can be represented as a sum of perfect sinusoidal components within each evaluated time window, in which the statistical properties of the signal do not change significantly. This assumption holds for an ideal specimen but deviates from the predominant stress-strain relation of actual specimens or even larger structures. Secondly, the ANN has fewer possibilities to “learn” patterns in the dataset if the number of inputs is reduced. Especially the second effect is also observable in the results of the ANN$_{\mathrm{SB}}$ trained on $\mathbf{X}$. Here, the number of input parameters, the evaluated frequency range and the combination of piezoceramics significantly influence the resulting predictions. The highest accuracies originate from measurements at piezoceramics that were asymmetrically positioned relative to the overlap (P1↔P3, P2↔P4), which are wider apart compared to both inner piezoceramics (P2↔P3). However, the asymmetric positioning appears to be more dependent on the evaluated frequency range. The most information-rich frequency range for both asymmetric combinations is located between $202.5 - 206.0\,\mathrm{kHz}$. However, these observations result from the formation of eigenmodes in the specimen, which is dependent on the location of the piezoceramics and f_{c}, as will be shown later (Chapter 4.2). In contrast, the symmetric positioning shows wide horizontal areas, indicating a reduced dependence on the frequency range, which could be beneficial in terms of reliability.

An intuitive result can be observed by evaluating the highest reached accuracy for the different pathways over the numbers of used sidebands $\mathbf{s}_j$ sidebands for the ANNs (Figure 4.7 right). Note that $\mathbf{s}_j$ is indicating the number of included sidebands to the left and right around the carrier ($\mathbf{s}_2 = [A_{-2}, A_{-1}, A_{\mathrm{c}}, A_{-1}, A_{-2}]$). By training ANNs exclusively on the amplitude of the carrier and the first sidebands, a classification accuracy of around 73 % is achieved. Evaluating more sidebands $\mathbf{s}_j$ increases the amount of information for the network, resulting in significantly higher accuracies. The highest accuracy is achieved by using $\mathbf{s}_5$ (the carrier amplitude and five sidebands of each side). Using more sidebands resulted in a slight decrease in accuracy. One reason for the decrease could originate from the diminishing amplitudes of the subsequent sidebands and the reduced signal-to-noise ratio. Consequently, the ANN "detects" patterns within the noise, which leads to overfitting and a subsequent decline in accuracy. Furthermore, additional input parameters complicate the optimisation process during training, but this can be mitigated by providing more or higher-quality data.

The relevance of more data points was additionally evaluated by increasing the size of the training set from 10 % of the dataset to 90 %. The increase of the classification accuracy is shown in Figure 4.8, where it rises from around 60 % to around 90 %. Note that the number of cross-validations in this graph was increased to 50 trained ANNs to account for variability, especially if the size of either the train or the test data is small.

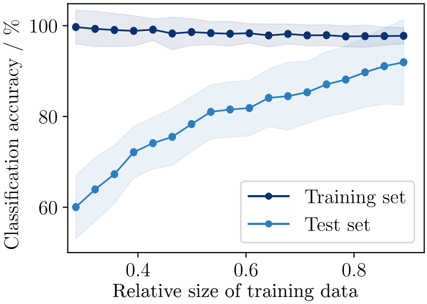

Figure 4.8.: The mean classification accuracy over the percentage of the training set size.

The ANNs with the highest averaged cross-validation accuracy resulted in an overall accuracy of 93.4 %, and is indicated by red markers in Figure 4.7. This classification result is also shown in Figure 4.9 (left) as a confusion matrix, where the diagonal fields indicate the percentage of true classifications and the off-diagonal fields represent the percentage of the false classifications. Hence, it is possible to understand which classes were "confused" by the ANN. The data for this prediction results from ten different frequencies per specimen (five from P4↔P2 and five from P2↔P4 in the range 202.5 – 204.5 kHz) and 11 input values (*i.e.*, $\mathbf{s}_5$: amplitude of the carrier and five sidebands of both sides). It is

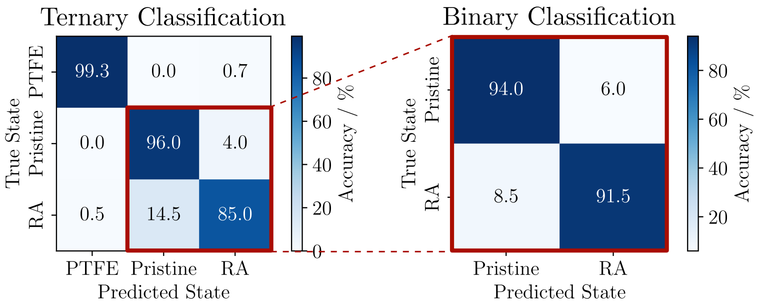

Figure 4.9.: Confusion matrix from the most accurate prediction based on the mean of a 10-fold cross-validation when differentiating between all resulting samples, *i.e.*, vibro-acoustic modulation signals, using an ANN trained on all three defect classes (left). A second binary ANN (right) is trained solely to differentiate between samples from pristine and release agent contaminated specimens by removing all samples associated with PTFE film specimens from training and classification.

shown, that the measurements at specimens with introduced PTFE films were classified correctly with an accuracy of over 99 %. However, distinguishing the measurements of the other two classes is less accurate, with an average accuracy of 91.6 %, resulting in an overall accuracy of 93.4 % between all three classes (ternary classification).

Since PTFE films in the bond are detectable with both the $\mathrm{ANN}_{\mathrm{SB}}$ and traditional ultrasonic testing, the PTFE samples were removed from the dataset to focus on the challenge of detecting weak bonds. Using an ANN with the same architecture (except for a reduction in the number of softmax outputs), the ability to distinguish between the remaining two defects was tested. The detection of weak bonds could be enhanced by using input data with the same number of sidebands and carrier frequency range as before. As shown in Figure 4.9 (right), an accuracy of 93.1 % was achieved for a binary differentiation between pristine specimens and those contaminated with a release agent.

This highly precise prediction from the ternary classification was inspected more thoroughly. Interestingly, there is one specimen from which all samples were misclassified. Also in the binary classification, 80 % of the samples from this specimen were misclassified. Both ANNs (binary and ternary) classified this pristine specimen as contaminated with a release agent. Interestingly, its shear strength mirrors that of release agent-contaminated specimens as well, which is illustrated in Figure 4.10 (star below distribution). This misclassification sug-

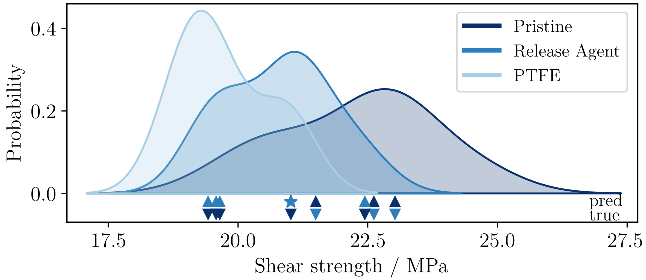

Figure 4.10.: Probability distribution of the shear strength from the three specimen classes. Below the distribution, the shear strength of misclassified samples is indicated. Upward triangles represent the predicted value, while downward triangles indicate the actual class, following the colour code in the legend. The specimen that was completely misclassified is denoted as a star. Note that only samples of the eight specimens with the lowest prediction accuracy were included.

gests that the ANN detected unintended manufacturing errors in this pristine specimen, which led to the reduced strength. Additionally, seven other specimens had more than 10 % misclassification, indicated by triangles in Figure 4.10. The colour code of the upper triangle represents the predicted specimen class, while the lower triangle indicates the actual class. The ternary ANN frequently misclassifies pristine specimens with low shear strength as release agent contaminated and vice versa for release agent specimens with relatively high shear strength. This suggests that the ANN detects actual but unintended contaminations and manufacturing errors, altering the specimen's shear strength and thus predicts the class to which the specimen should belong.

4.1.8. Shear strength prediction

Instead of merely classifying the specimens into three categories, the previous results indicate that shear strength could serve as an additional metric for more detailed differentiation, enhancing the robustness of the ANN approach. In a further evaluation, the shear strength σ_s of each specimen was predicted through regression, using a similar ANN architecture but with a linear output unit. Prior tests confirmed that the previously defined architecture of the ANN is adequate for regression as well. Similar to the classification process, various numbers of sidebands, ranges of carrier frequencies f_c, and signal pathways between piezoceramic actuators were used, permuted, and shuffled to assess the robustness and information gain of these parameters.

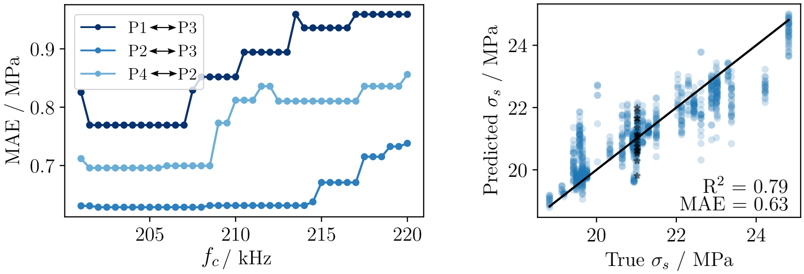

Figure 4.11.: MAE of the predicted shear strength over the carrier frequency for the different signal paths from ANNs trained on $\mathbf{X}$ (left). The prediction with the lowest MAE is compared to the actual shear strength (right), where closer proximity to the line indicates a higher precision. Black stars denote samples from the single misclassified pristine specimen.

Comparable to the results of the classification, the MAE improves when more sidebands are included in the ANN analysis (see Figure A.7 in the Appendix). It is important to note that the goal is to minimise the MAE. As before, the accuracy depends on the frequency, although the areas of minimal MAE cover wider frequency ranges as shown in Figure 4.11 (left). Unlike previous results, the lowest MAE results from a symmetric piezoceramic layout (P2↔P3). Also, lower frequencies lead to the lowest error of the prediction, while the frequency influences P2↔P3 less, compared to the other piezoceramic locations. The predicted σ_s with the lowest MAE of 0.63 MPa shows a reasonable correlation to the actual σ_s ($R^2 = 0.79$ in Figure 4.11, right). However, a notable deviation is observed in the predictions of each individual specimen (using input data from 13 different carrier frequencies in the range of $202 - 208$ kHz for P2↔P3).

The misclassified pristine specimen, indicated by stars in Figure 4.11 (right), shows variations between the predictions at the different samples but, on average, aligns well with the experimentally determined shear strength. Consequently, the shear strength regression serves as a complementary tool for interpreting classification results and helps to identify weak bonds.

4.1.9. Feature importance

Understanding the decision-making process in ANNs is inherently complex, making it difficult to interpret the causal relationship between inputs and outputs. To address this, two well-established methods are utilised and compared to evaluate and determine the significance of sidebands in the predictions made by ANN_{SB}. Figure 4.12 presents the results of the feature importance analysis, comparing Shapley Additive Explanations (SHAP) [184] with feature importance derived from Garson's Algorithm [186]. Shown are the averaged results of the ten-fold cross-validation. For each cross-validation, sidebands of either $\mathbf{s}_3$, $\mathbf{s}_5$ or $\mathbf{s}_8$ are used as inputs, resulting in the three highest classification accuracies. It is worth noting that the frequency ranges of the training data from these ANNs differ slightly ($202.5 - 204.5$ kHz, $202.5 - 204.5$ kHz and $204 - 206.5$ kHz). According to both evaluated feature importance methods, the first sidebands around the carrier are not the most important features for classifying the bonds. Instead, the subsequent sidebands show much higher importance in both methods. This result underlines the significance of improving the traditional VAM evaluation to detect bond line flaws. The high importance of the second and third sidebands

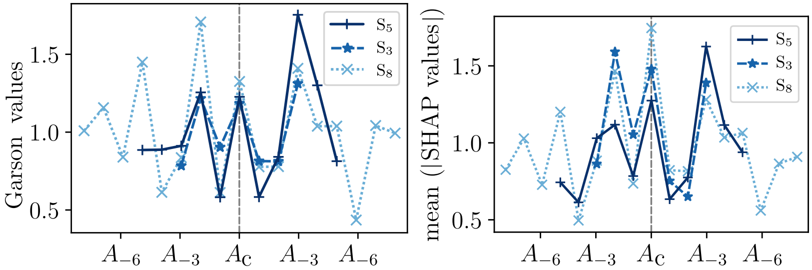

Figure 4.12.: Two types of feature importance are shown from the three most precise $\mathrm{ANN}_{\mathrm{SB}}$, each trained on slightly different frequency ranges and $\mathbf{s}_j$. The results of the Garsons' algorithm (left) and SHAP (right) show the averaged importance over the 10-fold cross-validation, where the height indicates the relevance of the individual sideband or carriers.

further indicates the relevance of analysing the effect of the different sources of non-linearity (cf. Figure 2.4) on VAM, as they have specific contributions to the harmonics and sidebands. Finally, the shortcomings of a traditional evaluation are emphasised, which are based on a damage parameter (*e.g.* the modulation index or the sideband ratio), since these parameters are typically calculated using only the carrier and the first sidebands. Finally, the limitations of traditional evaluations, which rely on damage parameters (*e.g.*, the MI or the sideband ratio), are emphasised. These parameters are typically calculated using only the carrier and the first sidebands, which also explains, why the differences in Chapter 4.1.6 were minimal.

In a third attempt, the symmetry of the sidebands was evaluated. Interchanging the left and right sidebands as input for the most accurate ternary $\mathrm{ANN}_{\mathrm{SB}}$ reduces classification accuracy by an average of 28 %. This indicates a significant asymmetry in the sidebands, which is likely another essential factor in detecting the specimens with a weak bond.

4.2. Detection of crystallisation defects in welded steel

Evaluating VAM with machine learning algorithms has significantly increased the sensitivity for detecting contaminations in adhesive bonds. Based on the presented classification of adhesive bonds, this chapter assesses and validates the applicability of the enhanced evaluation (by training ANNs on VAM sidebands) for metal specimens. Metal specimens pose an additional challenge due to pronounced eigenmodes in the frequency spectrum. These eigenmodes cause fluctuations in signal strength and modulation, interfering with the comparison of neighbouring carrier frequencies. To address the challenges, welded "dog-bone" specimens were created. Similar to the GFRP specimen, the defects were introduced in the weld root at the centre of each specimen during the joining process. It is anticipated that incorrect welding parameters result in defects that are challenging to detect with traditional NDT methods.

Numerous NDT methods have been established for testing metals and welded joints in particular. These include visual inspections, electromagnetic testing, eddy current testing, ultrasonic testing, *etc.* [188–191]. However, these methods often reach the limits of their sensitivity for the detection of root defects in butt welds [192]. This limited sensitivity is problematic when the defect does not result from voids or cracks where a cavity is formed. A relevant example of the "challenging defects" arises from incorrect welding parameters (*e.g.* welding current or speeds), leading to unfavourable crystallisation, distinct grain boundaries or the inclusions of the more pure electrode material within the base material [193]. Such defects can be detected reliably by X-ray testing. However, the use of X-ray testing is challenging since the surrounding area must be shielded from the emitted radiation [194].

In literature, the evaluation of welded structures with VAM has already been tested by Lim and Sohn [195], where the remaining fatigue-life of welded bonds was predicted based on the increase of the *nonlinear parameter* (β). Additionally, Zagrai *et al.* [69] discussed the sensitivity of VAM for evaluating micro/meso scale. Therefore, the primary objective of this chapter is to assess whether the VAM method can detect root defects in welds. It is assumed that the traditional VAM evaluation is insufficient for defect detection, which can be overcome by utilising a data-driven evaluation similar to the introduced approach used for the adhesive bonds in Chapter 4.1.

The specimens were manufactured from S355 structural steel with a thickness of 8 mm. The geometry is a "dog-bone" shape with a total length of 270 mm in accordance with DIN EN ISO 6892-1. The specimens were joined with an X-weld in the centre of the narrowed cross-section. In total, 30 specimens were created with *ideal* and 30 specimens with faulty welding parameters. The second class will be referred to as *defect* specimens. Since the specimens originate from another project [196], the precise manufacturing was not part of this work and is only briefly summarised in the Appendix A.6.1.

For the VAM measurements, the pump wave was introduced in a hydraulic uniaxial testing machine. The load level was set to $R_\sigma = 0$, where the amplitude of 110 MPa coincides with the maximal stress and corresponds to 31 % of the elastic yield strength, and a frequency of 8 Hz was chosen. According to DIN 1993-1-9, the specimens should endure 2,000,000 load cycles at this stress level. Since each VAM measurement requires only 1,500 load cycles, the influence on the fatigue life is minimal. During this pump vibration, 71 carrier vibrations within the range of $f_\mathrm{c} = 185 - 220\,\mathrm{kHz}$ (spacing of 0.5 kHz) were measured for a duration of 2 s. Each carrier vibration was introduced by the before-mentioned piezoceramics, with a current of 9 V from the NI USB-6366 and amplified twofold by a BUF634 amplifier (*cf.* Chapter 3.3).

While VAM measurements were performed for all specimens after the welding, the mechanical properties of both classes were evaluated with tensile and fatigue experiments on several specimens. The cyclic tensile-tensile load for the fatigue experiments had an amplitude of 301 MPa (with a load level of $R_\sigma = 0$ and frequency of 8 Hz), which corresponds to 85 % of the specimen's elastic yield strength. Therefore, the specimens were projected to endure this load for 288.000 cycles, effectively translating to a fatigue life of 10 hours.

The tensile properties were acquired for two specimens from each class. The fracture pattern was similar across all specimens, occurring outside the heat-affected zone but inside the gauge length. Hence, the ultimate tensile strength is nearly identical at 379 MPa for *ideal* specimens and 368 MPa for *defect* specimens. Interestingly, the *defect* specimens showed a crack inside the weld around a dark

Figure 4.13.: Specimens after the tensile tests with the failure outside the heat affected zone for ideal (top) and altered welding parameters (bottom), with the average fatigue life of both specimen classes.

spot, which was already visible before the tensile test. Such effects and these kinds of dark spots were just observed at the *defect* specimens, as depicted in Figure 4.13 (left). The difference between the mechanical properties of both classes becomes evident in comparing the fatigue behaviour in Figure 4.13 (right). Specimens with the incorrect welding parameters endure a tension-tension fatigue load only for 29.4 % of the fatigue life compared to the ideal specimens. This significant reduction symbolises the demand for an improved detection of these defects.

In Figure 4.14, the average signal strength and average MI over all measured frequencies for the thirty specimens of each class are compared. While the median signal strength of the defect specimens is slightly increased, the median MI is equivalent for both classes. These differences are even smaller than those observed in the adhesive-bonded specimens of the previous chapter. As a comparison, the measurements from one specimen *without* a welded joint are shown. The signals of this specimen demonstrate a higher signal strength, stronger modulation and resulting in a higher MI. Therefore, creating more specimens without a weld did not seem relevant, as the deviations are comparable to the adhesive-bonded specimens with the introduced PTFE films in the previous chapter, for which the classification was almost flawless.

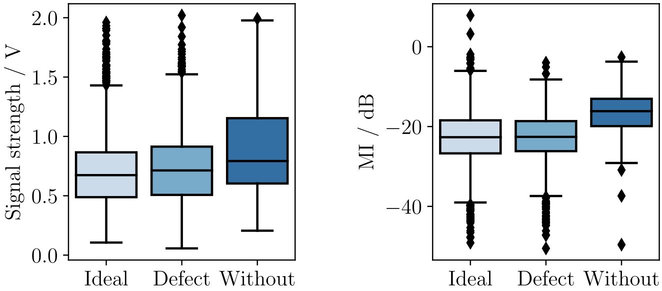

Figure 4.14.: Comparison of the mean signal strength (left) and the mean MI (right) between the *ideal* and *defect* specimen compared to a specimen without a weld.

Similar distributions result from extracting the AM and PM values.[5] It can be seen, that both welded classes are indifferentiable as well (*cf.* Figure A.9 of the Appendix).

When comparing the carrier amplitude A_c and the MI for both classes in more detail, as shown in Figure 4.15, deviations between the ideal and defect specimens emerge in several frequency areas. Especially, the A_c in the frequency area of $193 - 203\,\mathrm{kHz}$ differs between both classes, which is less obvious in the MI. However, the mean values of both classes are still within each other's standard deviation, depicted by the shaded regions. Notably, the shape of the mean amplitude A_c differs from the MI, indicating an information gain when evaluating both parameters in a statistical analysis or with machine learning algorithms.

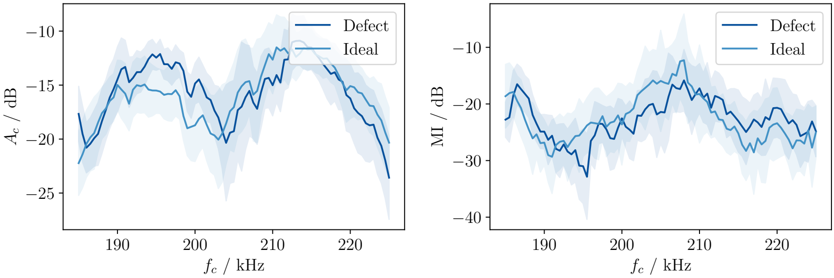

Figure 4.15.: Average amplitude of the carrier (left) and the MI (right) of all 60 specimens with the standard deviation as a shaded areas.

For the evaluation, the previous data-driven approach for the classification was adopted. However, in this evaluation, the frequency ranges on which the ANNs were trained had a constant width, which was shifted over the measured frequency spectrum to find "information-rich" areas. This procedure was conducted for different numbers of sidebands $\mathbf{s}_j$,[6] used as the input values to each ANN. A constant network architecture with two hidden layers of 36 and 10 neurons was chosen with two softmax neurons for the output of the classification. Larger networks were also tested but did not result in an increased classification accuracy, as they were prone to overfitting.

---

[5] This process is adapted from the STFT-based AM-PM separation, presented by Oppermann *et al.* [97]

[6] As before, the index j indicated the number of included sidebands to both sides of the carrier with "0" being just the carrier.

In the upper half of Figure 4.16, the highest achieved classification accuracy from the ten-fold cross-validations of an ANN trained on a frequency range, that includes this specific frequency, is shown. These results are differentiated by the width of the frequency range (see Figure 4.16, top left) and the number of sidebands (see Figure 4.16, top right). As before, the prediction accuracy depends on the carrier frequency. The most precise classifications were made in the range of 193 – 196 kHz with an accuracy of approximately 90 %. However, there are ranges (205 – 209 kHz) where the classification accuracy decreases below 70 %. In Figure 4.16 (top left), the number of subsequent frequencies in the test set was evaluated. Using a range of $n_{\text{freq}} = 5$ neighbouring frequencies results in the most precise classification. Increasing the number of neighbouring frequencies

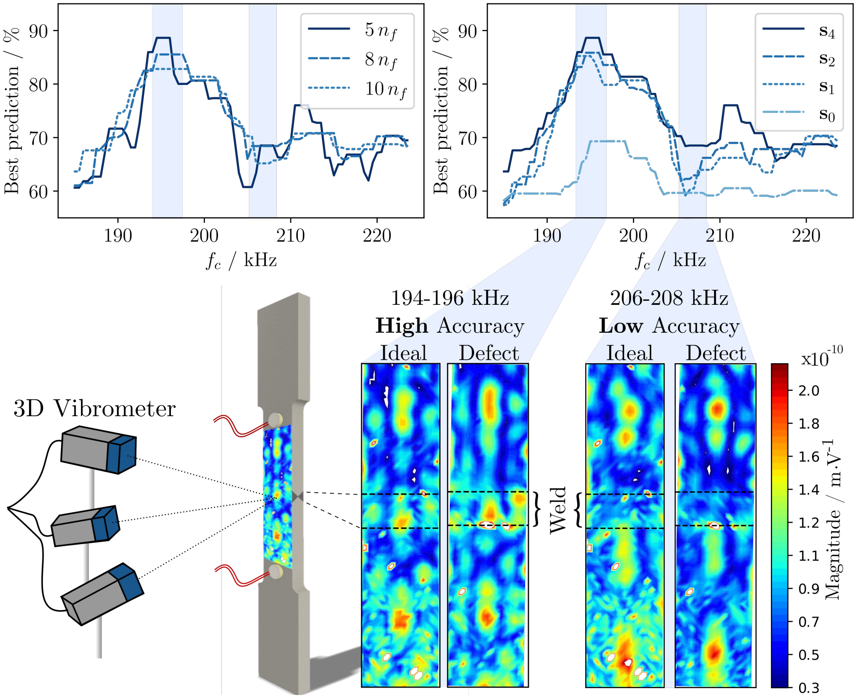

Figure 4.16.: Maximal reached accuracy from the ANN evaluation approach, regarding the number of neighbouring frequencies in the data set n_{freq} (top left) and the evaluated number of sidebands $\mathbf{s}_j$ (top right). Both graphs show a high dependency on the excitation frequency. The eigenmodes of the frequency range with the highest and the lowest accuracy are shown in the 3D-Vibrometer measurements (bottom right).

in the dataset reduces classification accuracy but increases the robustness of the prediction, as the dataset includes more frequencies.

Regarding the number of evaluated sidebands $\mathbf{s}_j$, a significant increase is observed when the first sidebands $\mathbf{s}_1$ are also included in the evaluation instead of just the carrier. The most accurate predictions can be computed if four sidebands of each side are used ($\mathbf{s}_4$). Interestingly, the frequency region around $f_\mathrm{c} = 210\,\mathrm{kHz}$ profits the most from including the third and fourth sidebands, since the difference between $\mathbf{s}_2$ and $\mathbf{s}_4$ is the highest in this area.

Comparable to the adhesive-bonded specimens, some frequency regions result in significantly higher classification accuracies. To understand the origin of this phenomenon, specimens of both classes were examined with a 3D-scanning, laser doppler vibrometer (Polytec, PSV-500-3D). For this evaluation, the signal generator of the vibrometer introduced a chirp signal into the specimen through one of the bonded piezoceramics. The three scanning heads acquired the acceleration of the specimen due to the chirp in all three dimensions for a defined grid of points throughout the specimen. From this data, the frequency of the eigenmodes and the form of the vibration at any frequency can be evaluated and visualised from the scanned zone. For these specimens, the scanned areas cover the entire width, between the piezoceramics as illustrated in Figure 4.16 (lower left). The lower piezoceramic was used to introduce the carrier vibration.

From this data, the vibration of the two indicated frequency ranges were visualised for ideal and defect specimens, as shown in Figure 4.16 (lower right). The images depict the magnitude of the vibration perpendicular to the specimen's surface. While the vibrations of both specimens appear similar, the relevant difference can be observed when comparing the two frequency ranges, especially between the dashed lines, which indicate the location of the weld. For the frequency range of $194-196\,\mathrm{kHz}$, where a high classification accuracy was achieved, a high magnitude of steady-state vibration can be found in the vicinity of the weld. In contrast, the magnitude is low for carrier-frequencies in the range of $206-208\,\mathrm{kHz}$, which resulted in rather low classification accuracy. Consequently, these results indicate that only in the first frequency region, the "necessary conditions" of Lim and Sohn [127] for the VAM evaluation are satisfied, and explain the occurrence of the frequency dependence of this data-driven approach.

5. Synthetic VAM for structural health monitoring

As shown in the previous chapter, the application of VAM in NDT environments has a high potential. Enhancing the VAM evaluation with machine learning methods improves the sensitivities for further detecting damages or deviations from a pristine state. However, despite 30 years of VAM research and numerous publications, the applicability for a condition monitoring of industrial structures or even SHM applications still faces several hurdles. These limitations must be overcome before the method is “industry-ready” or even ready for extensive testing on actual structures. In contrast to the controlled environmental conditions in the laboratory, massive computing capabilities, and the possibility of adding as many sensors as needed, the reality of industrial structures differs significantly. The most important aspects and how they affect VAM measurements are summarised briefly below.

(1) The probability that two industrial structures have identical vibrational behaviour, as assumed in the previous chapter, is unlikely. The classical SHM approach uses the initial measurements as the baseline, for which the pristine status after manufacturing is assured by traditional NDT evaluations. Hence, the SHM systems evaluate the structure for signal changes over the lifetime.

(2) Introducing the low-frequency pump wave X_p is challenging on actual structures and requires powerful actuators with external energy sources. Therefore, installing the needed infrastructure (*e.g.* cables for a power supply) and, more importantly, assuring that the introduced pump vibrations do not affect the fatigue life impedes the seamless integration of VAM into actual systems. Consequently, taking advantage of already present ambient vibrations as pump waves is desirable. However, using ambient vibrations also has several downsides. Most important is the effect of variations in the pump wave’s amplitude or frequency on the resulting modulation. A comparison between two VAM measurements is only valid if the ambient vibration remains constant during the measurement

and, more importantly, is consistent to the subsequent measurements as well. Unfortunately, such ideal pump vibrations are not evident in most civil or engineering structures. Structural vibrations depend on various environmental factors, such as wind patterns, temperature fluctuations, traffic, and seasonal variations. These aspects result in changes in the structure's eigenmodes and corresponding dominant frequencies and hinder the application of VAM with ambient vibrations. Additionally, the ambient vibrations of industrial structures appear as a superposition of multiple frequencies, complicating VAM evaluation. This results in sidebands for each ambient frequency, producing wide sidelobes compared to those observed when distinct frequencies are excited within the frequency range.

(3) Implementing actuators for the high-frequency carrier wave X_c follows similar challenges to pump wave actuators. Again, power management is a crucial aspect. Ideally, no additional power sources for the individual X_c actuators are needed. Wireless communicating actuators combined with energy harvesting systems for self-sufficient service life, are pertinent subjects currently being researched and advanced [197–199].

(4) The sensing and evaluation of the vibration is the fourth challenge. Ideally, the self-sufficient sensor nodes can also measure the resulting vibration. With low-power devices, the traditional evaluation of VAM is not possible as indicated by Oppermann *et al.* [97]. To circumvent this, the application of the STFT to chunks of the signal was proposed, which significantly reduced the required data and energy consumption. However, changes in the amplitude of X_p still affect the result and prevent the application of the sensor nodes outside the laboratory. These self-sufficient sensor nodes would allow for the application of VAM at many structures and the realisation of a sensor network, performing measurements in several locations. An optimal damage detection and even the damage localisation could be achieved by combining the data from these locations, as shown by Broda *et al.* [123]. Nevertheless, the strategic positioning of sensors for reliable damage detections is still unresolved and under active research [200].

To address the aforementioned aspects, this chapter proposes a new strategy for acquiring and evaluating data for the VAM method. The *synthetic VAM method* reconstructs the modulated signal from multiple measurements, where only the carrier vibration X_{c} is introduced and measured at different stress levels in the structure. This new approach differs from the traditional VAM, which requires simultaneous carrier and pump vibrations. In contrast, the synthetic VAM method decouples the measurements from the actual amplitude and frequency of the pump vibration X_{p} enabling the application of VAM even when environmental conditions—and subsequently X_{p}—change around the structure. This decoupling drastically enhances the applicability of VAM. Furthermore, this methodology reduces the requirements on the sensor nodes in terms of measured points and sampling rate drastically, leading to cheaper and lighter sensors. With these reduced requirements, even the application of self-sufficient energy-harvesting sensors becomes feasible, further reducing the installation and maintenance costs to monitor a structure.

5.1. Generation of the synthetic VAM

The traditional approach of VAM—as summarised in Chapter 2.5—is based on the acousto-elastic and stress-dependent change of an exited ultrasonic vibration. Most studies use a sinusoidal pump vibration to periodically alter the stress state of the specimen, which affects the ultrasonic wave propagation, widens defects and creates local stress distributions. These effects result in the modulation of the continuous introduced carrier vibration X_{c}. Dorendorf *et al.* [71] have shown that the wave characteristics of the resulting VAM measurement X_{r}—such as the amplitude and phase of the signal—oscillates between the response of only the carrier excitation at the lowest and highest stress of the pump vibration.

For the fundamental concept of the *synthetic VAM*, it is assumed that the amplitude and phase of the resulting signal X_{r} can be approximated by the steady-state response of the carrier vibration X_{c} for each specific stress level σ_{l}. Consequently, the dynamic VAM signal can be reconstructed by quantising the pump vibration into a distinct amount of stress levels n, similar to the analogue-to-digital transformation in signal processing. The resulting synthetic signals can be evaluated with traditional evaluated damage indices, like the MI, R and others. This process is illustrated in Figure 5.1 by quantising the pump wave X_{p} into $n = 4$ distinct stress levels. A sinusoidal pump vibration—as typ-

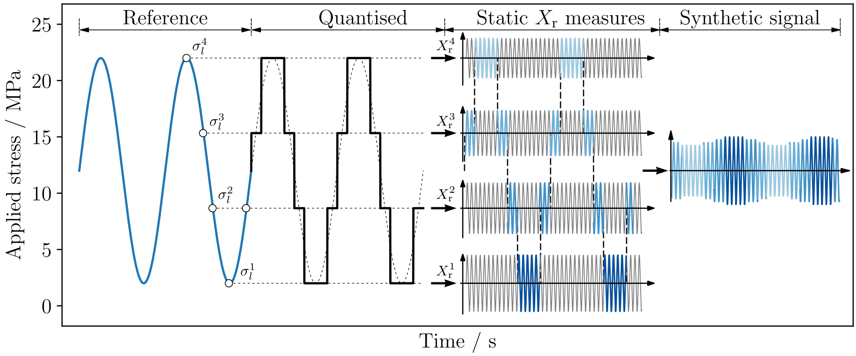

Figure 5.1.: For the synthetic VAM method, the traditional sinusoidal pump wave is quantised into n discrete stress levels. In this example, $n = 4$ stress levels were chosen, at which the resulting signals X_r of just the carrier vibration is acquired. The highlighted areas of the X_r measurements are concatenated into a synthetic VAM signal of arbitrary frequency.

ically used in the traditional VAM—is given on the left side at a stress range of 2.5 – 25.0 MPa. The signal in this example is quantised with equidistant stress levels σ_l, which are illustrated by the dots and dashed horizontal lines. Other procedures for choosing the quantisation levels—known from signal processing [201]—could reduce the quantisation error, but are outside the scope of this thesis. At each stress level of this quantised pump vibration, the high-frequency response $\left[X_\mathrm{r}^1, \ldots, X_\mathrm{r}^n\right]$ with $X_r^l(\sigma_\mathrm{l}, t)$ is measured. Finally, the synthetic VAM signal is generated by concatenating chunks of the measurements, based on the alternating stress levels of quantised pump vibration (right). In this process, any arbitrary pump frequency can be used for the concentration, and the signal can be combined with an arbitrary length. Even though the synthetic procedure results in discontinuous transitions between the chunks due to the concatenation and an already-mentioned quantisation error, this quantisation error diminishes when the number of levels n is increased.

To compare and evaluate the synthetic VAM, the generated signals with a calculated MI are compared to the traditional dynamic VAM approach. Firstly, the synthetic approach is shown on an artificial amplitude-modulated signal (eq. (A.7) in the Appendix). The envelope of a dynamic signal is illustrated in the time domain as a black line in Figure 5.2 (left). Additionally, synthetic signals are shown, which were generated from $n = 2$ and $n = 3$ stress levels. Note that both signals are symmetrical. For a better comparison, only half of the

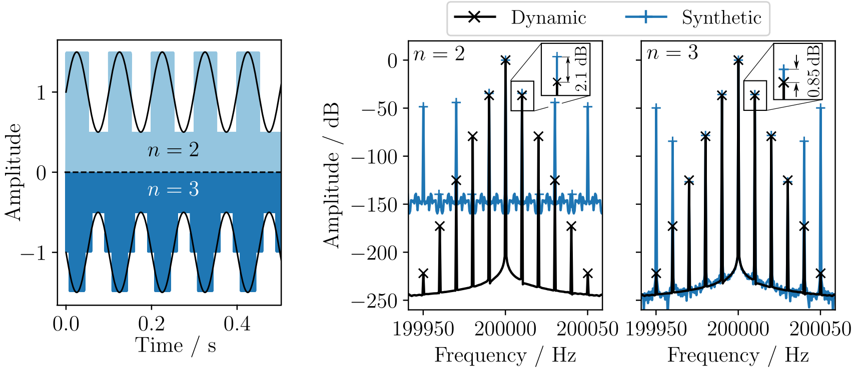

Figure 5.2.: Comparison of the dynamic modulated signal (black line indicates the envelope of the signal) with the synthetically generated signals with $n = 2$ and $n = 3$ static levels. The time domain (left) and the frequency domain (right) show a high precision of the approximation, which improves by increasing n.

synthetic signals are shown. An amplitude modulation is visible at both signals, that follows the expected dynamic reference. Intuitively, increasing the number of stress levels n results in the convergence of the synthetic signal towards the dynamic response. Using more steps, on the other hand, requires more measurements and data points to be transmitted and stored. Hence, the reduction to the minimum of $n = 2$, resulting in the creation of a square wave (Figure 5.2, top left), is advantageous when applying VAM inside a sensor network.

The FFT from both signals is compared to the FFT of the dynamic signal in Figure 5.2 (right). The FFT of the dynamic signal results in distinct sidebands around the carrier frequency, where the amplitudes decrease at the subsequent sidebands. In contrast, in the FFT of the synthetic signals ($n = 2$), only the first, third and fifth sidebands are visible, while the amplitudes decline minimally. Intuitively, the synthetic signal from $n = 3$ approximates the dynamic signal more precisely, resulting in a close resemblance of the first three sidebands. However, a notable offset of around 2.098 dB and 0.847 dB occurs between the first sideband of the synthetic approaches from $n = 2$ and $n = 3$, compared to the dynamic measurements, as shown in the insets. The amplitude at the carrier frequency A_c is identical for all three signals.

The shown deviations for $n = 2$ were already explained in the literature in the mathematical description of square waves (sq) and its Fourier transformation $\mathcal{F}$ [202]. The observed behaviour follows equation 5.1.

$$\mathcal{F}\left\{\mathrm{sq}(2\pi f_\mathrm{p})\right\} = \begin{cases} \frac{4}{l\pi}, & \text{for } |f| = l f_\mathrm{p}, \text{ with } l = 1, 3, 5, \dots \\ 0, & \text{otherwise} \end{cases} \tag{5.1}$$

In the frequency-spectrum of square waves, only odd frequencies ($l = 1, 3, 5, \dots$) are present, the first amplitude is offset by $4/\pi$ and the following amplitudes by a factor of $4/(l\pi)$. Hence, if our modulating low-frequency pump wave is synthetically recreated to be a square wave, the relationship shown in equation 5.1 applies to the sidebands around the carrier in a modulated signal as well. While the amplitude of the carrier is identical for the synthetic and dynamic measurements, the first sideband (at $n = 2$) is increased by $20 \cdot \log_{10}(4/\pi) = 2.098\,\mathrm{dB}$. Consequently, the MI of the synthetic signal is offset by this $2.098\,\mathrm{dB}$ as well, which describes the difference shown in the inset of Figure 5.2 (right).

By increasing the number of levels n, the synthetic signal converges towards the dynamic measurements. This convergence is shown for the MI in Figure 5.3. Furthermore, the amplitudes of the higher sidebands converge towards the amplitudes found at the dynamic measurements, making the evaluation of these sidebands also suitable for an evaluation if n is large enough.

To improve the synthetic method and decrease the required data points to a minimum, the underlying requirements of a VAM measurement have to be discussed. Each VAM measurement depends on several parameters. Obviously, the frequency f_c and excitation amplitude A_c of the carrier vibration are influencing the resulting signal X_r. The positioning of the actuators and the frequency f_c define the lamb wave propagation, which influences a VAM measurement

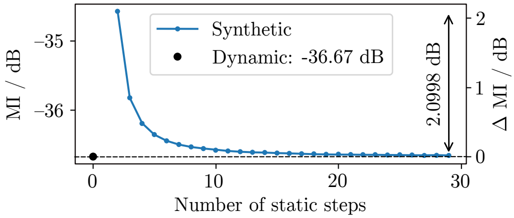

Figure 5.3.: As the number of steps increases, the MI of the synthetic VAM signal converges towards the MI of the dynamic measurement.

(*cf.* Chapter 4.2). However, the often proposed averaging over several frequencies reduces the influence of both. Note that the optimisation of the actuator's positioning is already a subject in literature [123, 203]. If this received signal has a sufficient signal-to-noise ratio and the conditions for a modulation (*cf.* Chapter 2.5) are satisfied, the limiting parameters on the measurement and used equipment are the *sampling rate* and the *time of measurement* at the data acquisition.

Challenging on low-power/energy-harvesting sensor nodes is the required *sampling rate* f_s, which determines the highest frequency in the spectrum. According to Nyquist's theorem, the sampling rate must be at least $f_\mathrm{s} > 2f_\mathrm{max}$ to accurately sample a sine wave with a f_max. For VAM measurements, f_max must exceed the frequency of the highest sideband $(f_\mathrm{c} + kf_\mathrm{p})$ that is of interest, where k is the index of the sideband. There are techniques (e.g., undersampling of the measured signal [97]) to circumvent this requirement. However, these algorithms presume constant vibrations throughout the measurement with a length of several periods of the pump vibration.

The *time of measurement* τ is also critical, as it limits the resolution of the FFT and, consequently, the evaluation of sidebands. Increasing τ increases the resolution in the frequency domain and improves the reliability of VAM if the pump and carrier vibrations remain constant. The traditional VAM requires a measured signal which includes at least one entire period of the pump vibration X_p to cover the whole stress range. Including additional cycles enhances reliability. However, the complex conditions in industrial structures impedes extended measurement times due to numerous external influences. Consequently, extracting relevant information from short signals is vital for VAM applications outside the laboratory.

So far, the generation of a synthetic signal has been explained by concentrating signal chunks for the stress levels with $f_\mathrm{s} > 2f_\mathrm{max}$. Assuming a steady state, even the required data from each chunk can be reduced drastically, by approximating each of the measurements $\left[X_\mathrm{r}^1, \ldots, X_\mathrm{r}^n\right]$ at σ_l from just several measured sampling points p. In theory, a minimum of two measurement points $(p = 2)$ would be sufficient to approximate the amplitude and phase of a sinusoidal carrier vibration [204]. Increasing p reduces the noise of the measurement and consequently, improves the precision. The approximation of X_r^l further allows for a sampling significantly below the Nyquist rate (undersampling) of just the carrier vibration, since τ can be as short as a few milliseconds, resulting in a measurement of nearly constant stress.

By monitoring the stress of the structure side by side with the ultrasonic response X_r (with strain gauges, fibre optics, etc., additionally to the piezoceramics), the individual chunks for the synthetic generation can also be extracted from an undersampled dynamic measurement, where the approximated values are combined with the actual stress. The process of generating the signal chunks from a dynamic measurement is illustrated in Figure 5.4. The measured elongation (equal to X_p) is compared to X_r (left). Every time a specified stress (or elongation) σ_l is reached (indicated by the intersections to the dashed horizontal lines for $n = 2$), the phase and amplitude of X_r at this point in time can be estimated. This process is shown in more detail in Figure 5.4 (right), where the measured signals at both stress levels are compared. From $p = 4$ measured points (dots in the Figure) of each signal, the amplitudes A and phases ϕ are approximated (since the frequency is known) and used to create the signal chunks for the synthetic process. For illustration purposes, the difference between both values is shown. However, the actual amplitude of each signal and each phase relative to the original carrier is calculated. Based on this process, any number of stress levels can be extracted from a dynamic signal. Since the elongation is known, the f_p of the signal becomes less relevant.

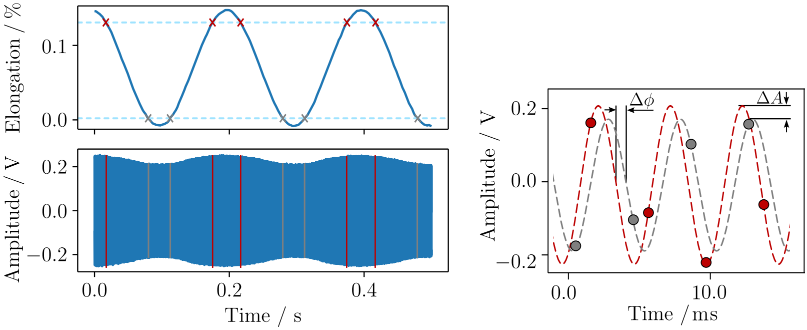

Figure 5.4.: Acquiring the specimen's elongation (pump-vibration, top) additionally to the response X_r (bottom) enables the extraction of the amplitude and phase from the measured signal X_r at the relevant stress states. X_r of both stress levels are compared to illustrate the approximation from the down-sampled signal (right).

5.2. Burst excitation for VAM evaluation

The carrier wave X_c of the traditional VAM method is excited continuously, which could also be a limiting factor. To improve the damage localisation based on the VAM principle, Hu *et al.* [84] has proposed the utilisation of transient sinusoidal burst as carrier vibration to obtain a compromise between time resolution and dispersion of guided waves. Even though this burst-VAM method allows for the localisation of damage, no information regarding the sensitivity or comparisons to continuous carrier excitation has been given in the literature so far. Therefore, the damage sensitivity of the continuous VAM will be compared to the burst excitation.

To account for the damping of the propagating guided waves, a five-cycle sinusoidal burst, multiplied with a Hanning window, was chosen. The results are averaged over 20 subsequent bursts, sent with a time delay of 1 ms, to reduce the noise. For comparability, the frequencies f_c of the bursts as carrier vibrations are identical to the frequencies of the continuous excited carrier vibrations.

From each burst, the received signal can be evaluated regarding the change in amplitude A and time of travel for the main signal, but also the reflections on the edges of the specimen. In Figure 5.5 (right) the first peak corresponds with the time, the A_0 modes of the Lamb-waves travel between the piezoceramics. The second and third marked peaks stem from a reflection of the upper and lower edges. From these peaks, the time and amplitude can be evaluated in

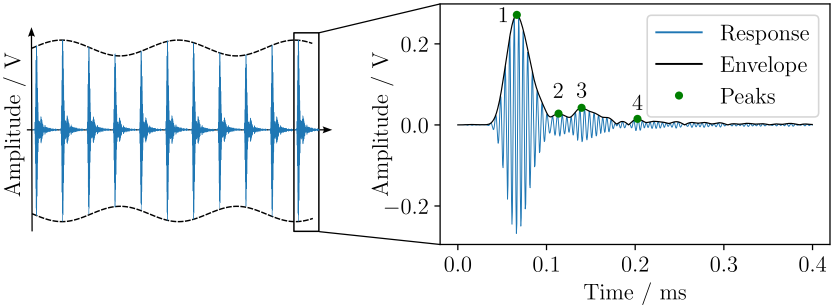

Figure 5.5.: Illustration of the burst-VAM approach. Instead of a continuous carrier, a set of tone bursts is introduced into the specimen. From this method, the modulation of the bursts due to the pump vibration (left) and the individual reflections inside the specimen (right) can be evaluated.

regard to the damage that was introduced. Note, that the amplitude of each peak was calculated from the Hilbert transform of the signal, which is illustrated as “Envelope” in Figure 5.5 (right).

5.3. Manufacturing and testing of the coupon specimen

The tested specimens in this Chapter can be divided into two groups. The first group consists of coupon specimens, which were tested to evaluate the synthetic method. These are made from GFRP in a cross-ply layup or from aluminium. The synthetic method was furthermore validated on two larger and more complex specimens as a second group. The description of these larger structures is given in the respective Chapters 5.6.1 and 5.6.2.

The cross-ply specimens were manufactured from dry glass fibres as $[0, 90_3]_\mathrm{s}$ layup. According to Chapter 3.1, the dry fibres were impregnated with the low-viscosity epoxy resin during the VARTM process. The resulting specimens have a thickness of 3 mm and an overall length of 240 mm. The width was chosen to be 30 mm for the specimen discussed in Chapter 5.4 and 70 mm for the specimens of Chapter 5.5, due to the different objectives of the experiments. The dimensions and the positioning of the piezoceramics are shown in the lower part of Figure 5.6.

The synthetic VAM method was validated with open-hole aluminium specimens, in accordance with the work of Dorendorf *et al.* [71] and Oppermann *et al.* [97] and comparable to specimens used by Ramezani [126]. The specimens were cut in the required length from cold-pressed aluminium 7075 bars with the dimensions of 25 x 2 mm. Afterwards, a hole of 4.5 mm diameter was drilled in the centre, as shown in the upper part of Figure 5.6, along with the dimensions.

The testing strategy was adjusted for both materials and specimen type, to account for varying material properties, geometries and failure mechanisms. The cracks were introduced into the aluminium specimens through fatigue loading in the tension-tension regime, with a maximum stress of 150 MPa, a fatigue frequency of 5 Hz, and a stress ratio of $R_\sigma = 0.1$ to realise a lifetime of approximately 30 000 cycles. Prior to the fatigue loading, and after every 2 000 cycles, a dynamic VAM ($\sigma_\mathrm{p} = 3 - 30\,\mathrm{MPa}$) was performed. Additionally, the carrier vibration was measured at three stress levels ($\sigma_\mathrm{l} = 3, 16, 30\,\mathrm{MPa}$) to generate

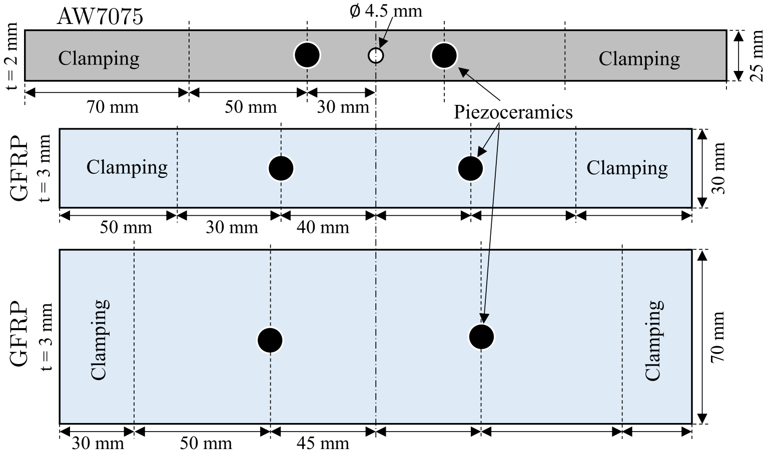

Figure 5.6.: Overview of the tested coupon specimens with dimensions, the location of the piezoceramics and the clamping. Shown are aluminium (top) and GFRP $[0, 90_3]_s$ specimens (centre and bottom).

a synthetic VAM signal. The process continued until the specimens reached ultimate failure.

The defects were introduced into the GFRP specimen by increasing the stress stepwise, as illustrated in Figure 5.7. When the cross-ply laminate is subjected to the so-called "knee-stress", cracks in the 90° layer occur (inter-fibre failures), which reduces the Young's modulus. Hence, after the static measurements ($\sigma_l = 2.2, 5.6, 8.9, 12.2, 15.6, 18.9, 22.0\,\mathrm{MPa}$) for the synthetic VAM and dynamic measurements for the traditional VAM ($\sigma_p = 2.2 - 22.0\,\mathrm{MPa}$), a uniaxial tensile test was performed. The load was increased at a rate of 5 MPa/s until the specified stress level was reached, and afterwards decreased to zero at the same rate. The maximal load of each step was increased until a sufficient number of cracks were visible in the specimen. These damage states enable the correlation between the number of cracks in the GFRP specimen and the results from both VAM methods.

The high-frequency carrier X_c was introduced and measured of all specimens using piezoceramic actuator disks within a frequency range of $f_c = 185 - 215\,\mathrm{kHz}$. In this range, 61 carrier frequencies were measured (spacing of 500 Hz). The dynamic VAM was measured for $\tau = 1\,\mathrm{s}$, at a sampling rate of $f_s = 2\,\mathrm{MSa/s}$. To simulate lower resolution signals, every 10th, 100th or 500th value of the sig-

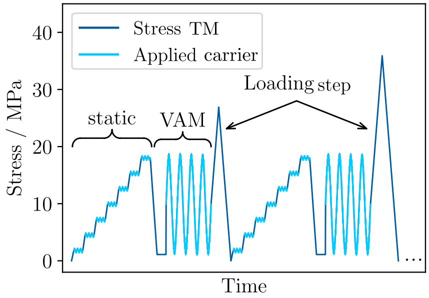

Figure 5.7.: Test design to compare the traditional and the synthetic VAM. Applied stress as introduced by a hydraulic tensile-testing machine and respective VAM measurements with a carrier vibration are indicated. After each measurement cycle, a loading step is performed.

nal was selected to mimic sampling rates of $f_s = 200\,\mathrm{kHz}$, $f_s = 20\,\mathrm{kHz}$, and $f_s = 4\,\mathrm{kHz}$, respectively. Given the highest carrier frequency f_c with the sidebands, a sampling rate of 450 kHz would be sufficient to satisfy the Nyquist criterion. Consequently, the sampling rate of $f_s = 4\,\mathrm{kHz}$ represents just 0.9 % of the Nyquist rate.

5.4. Synthetic VAM for coupon specimens

The tested cross-ply specimens offer the advantage of visually quantifiable damages, allowing for the correlation of VAM measurements to the number of inter-fibre cracks. The stress-strain curve of the cross-ply laminate in Figure 5.8 (left) shows the occurrence of these inter-fibre cracks in the 90° layers at a stress of approximately 60 MPa. These damages increase the elongation and reduce the modulus of the specimen as visible in the formation of a so-called “knee” of the stress-strain curve. However, the ultimate tensile strength of the specimen is mainly determined by the 0° layers on the outside of the specimen. Hence, the ultimate failure occurs at 198 MPa. This high distance between “knee stress” and failure is only observable in a tensile test. A fatigue load would result in delaminations around the inter-fibre cracks, which reduce the fatigue life drastically, as introduced in Chapter 2.

VAM measurements were performed at these specimens below the “knee stress” to establish a baseline without any damage. Subsequently, the specimens were subjected to a tensile stress of 67 MPa, resulting in the formation of inter-fibre

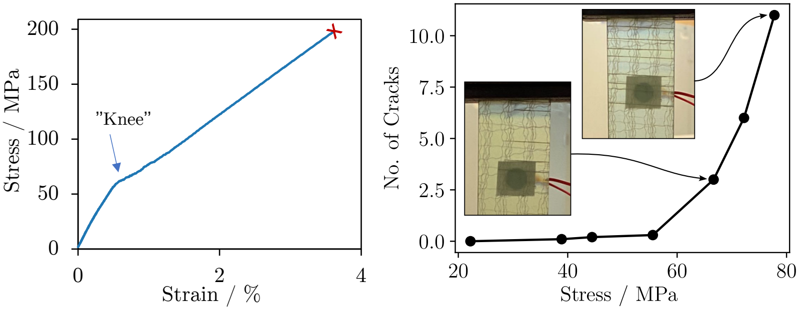

Figure 5.8.: The stress-strain curve of a representative specimen (left) shows a distinct “knee-stress”, which indicates the occurrence of inter-fibre fractures in the 90° layer. These cracks were counted after each loading step to correlate the VAM measurements. These cracks are depicted exemplarily in the insets.

cracks. After each loading step, the number of cracks was counted, as shown in Figure 5.8 (right). The insets depict two different states of the specimen. The occurrence of inter-fibre cracks is visible as darker horizontal lines. Initially, the cracks only extend over half of the specimen’s 90° layers but evolved into full cracks at the next stress level of 72 MPa. The second picture shows the specimen after the loading step to 78 MPa, resulting in the final damage state with 11 cracks.

Figure 5.9 (left) compares the specimen’s response before and after damage. A carrier frequency of $f_\mathrm{c} = 185\,\mathrm{kHz}$ was chosen in this illustration, and due to symmetry, only half of the synthetic signals are shown. The signal chunks of the different stress levels are distinguished by colour. Additionally, the envelope of the dynamically measured VAM is included for comparison. It can be seen, that the amplitude of the dynamic signal matches the amplitudes of the static measurements at each stress state. For the initial undamaged measurement at the shown frequency, the measured voltage is the highest at $\sigma_\mathrm{l} = 22\,\mathrm{MPa}$ and decreases slightly with decreasing stress. This relation reverses with the formation of cracks. While the amplitude at $\sigma_\mathrm{l} = 2\,\mathrm{MPa}$ remains almost constant, the amplitudes at the higher stress levels are reduced. This decrease with higher stress aligns with the often-mentioned bi-linear stiffness behaviour, commonly used to explain VAM [133, 205]. The stress-related crack opening reduces the wave propagating, thereby decreasing the amplitude. However, specific frequencies exhibit the opposite behaviour. At a frequency of $f_\mathrm{c} = 209.5\,\mathrm{kHz}$ (*cf.* Figure A.11),

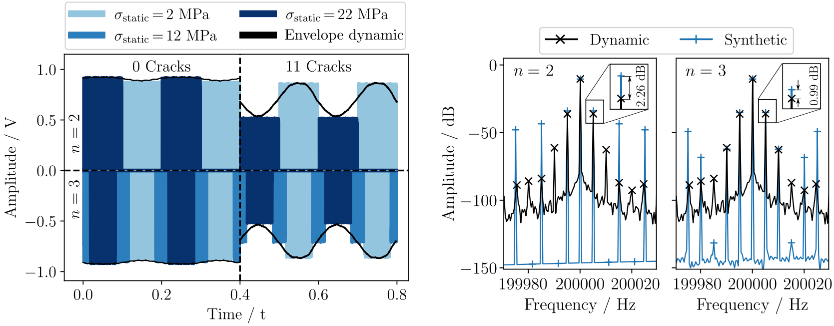

Figure 5.9.: Synthetic signals were generated for the GFRP specimen from $n = 2$ (top) and $n = 3$ (bottom) static measurements. The pristine signals are compared to the state with 11 inter-fibre fractures. In comparison, the envelope of the dynamic VAM signal is depicted as a black line. The frequency spectra of synthetic and dynamic VAM are compared from $n = 2$ and $n = 3$ (right), with insets highlighting the first sidebands and the differences between the two VAM methods.

the voltage at both low and high stresses increases due to the damage, contradicting the bi-linear stiffness model. The VAM model proposed by Dorendorf *et al.* [71] on the other hand explains both observed phenomena. This model emphasises the importance of the nearest eigenmode that primarily contributes to the system response. Therefore, whether the carrier frequency is higher or lower than f_{eigen} determines if the signal increases or decreases with changing stress.

It should be noted, that the stepwise change in amplitudes between individual signal chunks results in the amplitude modulation of the synthetic signal. Additionally, the phase of the signal changes between the signal chunks. The different phases arose from the alternating elongation, the changing distances between the piezoceramics, and the altered geometrical stiffness due to the stress changes in the specimen. Thus, the alternating chunks introduce a phase modulation into the synthetic approach, even though it is not visible in the figure.

Both methods are compared in the frequency domain around the carrier in Figure 5.9 (right). The findings align with those observed in perfectly modulated signals, as shown in Figure 5.2 (right). The first sidebands of the synthetic signal ($n = 2$) are offset from the dynamic signal by approximately $\Delta\text{MI} = 2.1\,\text{dB}$. Using three stress levels decreases the difference to $\Delta\text{MI} = 0.85\,\text{dB}$. While the sidebands of the square-wave signal follow eq. 5.1, the usage of three stress levels improves the approximation of the first and second sidebands and reduces quantisation error. This approximation of the third and subsequent sidebands is even further improved by generating the synthetic VAM from more stress levels, as demonstrated by the convergence of the MI in Figure 5.3.

In Figure 5.10 (left), the difference between the synthetic and dynamic MI is shown using $n = 2, 3, 7$ stress levels. For this evaluation, the synthetic VAM was generated from $p = 8$ points of each stress level to approximate the amplitude and phase ($f_s = 2\,\mathrm{MSa/s}$). Using the measurements of two stress levels, the averaged difference between both methods is $\Delta\mathrm{MI}_2 = 2.254 \pm 0.45\,\mathrm{dB}$, which closely matches the anticipated offset of $\Delta\mathrm{MI}_{2,\mathrm{ref}} = 2.098\,\mathrm{dB}$, that results from the synthetic process itself. Therefore, the deviation of the synthetic process from this expected offset is 0.154 dB, which is equivalent to 0.73 % of the averaged dynamic MI. Increasing the number of static stress levels ($n = 7$) reduces the averaged difference to $\Delta\mathrm{MI}_7 = 0.44 \pm 0.44\,\mathrm{dB}$. Hence, the deviation of the MI is reduced to 0.12 %. Moreover, Figure 5.10 (left) reveals that the mentioned deviations primarily originate from two frequency ranges, around 196.0 kHz and 205.5 kHz, where the MI itself is minimal. This is further illustrated in Figure A.10 of the Appendix, where the MI is given for each damage state across the frequency

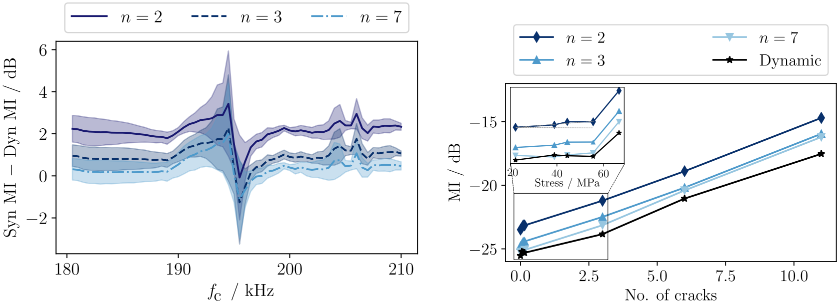

Figure 5.10.: The difference between the synthetic and dynamic MI and the standard deviation (over all tested damage states) are given for each frequency and the different n (left). The averaged MI over all frequencies measured at the GFRP cross-ply laminate, is compared for the different synthetic generated and dynamic signals of each damage state (right). With each inter-fibre fracture, the average MI increases linearly. The inset displays the first measurements plotted against the highest applied stress, which separates the overlapping measurements without a visible inter-fibre crack.

spectrum. Interestingly, the synthetic MI is increased on the left side of the resonance at 196 kHz and decreased on the right side. Selecting a suitable frequency range between 180 − 190 kHz helps to reduce these deviations. It's worth noting that the areas around the resonances are also commonly excluded in traditional VAM evaluations or compensated for by averaging over a wide frequency range [55, 66].

When considering the entire frequency range, the MI increases almost linearly with each inter-fibre fracture. This trend is depicted in Figure 5.10 (right) for the MI of the dynamic measurements and synthetic signals. Interestingly, the synthetic MI increases more linearly and consequently proves to be a robust indicator of cracks in the GFRP specimens. Moreover, there is a noticeable MI increase even before the first inter-fibre fracture occurs. This phenomenon is highlighted in the inset of Figure 5.8, where the MI is plotted against the maximal stress of the individual loading steps. This increase in MI after the first loadings may indicate the occurrence of initial micro-cracks within the composite or damages, introduced by the grips of the testing machine. Nevertheless, it's important to note that the MI increase, associated with the first inter-fibre fractures, is notably higher. Detailed results for the MI and the difference between both VAM methods, considering various values for the number of stress levels n, the sampling frequency f_s, and the number of points used p, are presented in Table A.2 of the Appendix. Results of a second GFRP specimen closely resemble those of the presented specimen, with a deviation of 0.97 % observed for $n = 2$. The averaged difference between the MI of both methods and the deviations from the expected offset are compared in Table 5.1. A parameter study for the second GFRP specimen can be found in Table A.3.

In contrast to the tested GFRP specimens, the MI for aluminium specimens exhibits considerable fluctuations which exceed 30 dB across the measured car-

Table 5.1.: Averaged difference between the synthetic and dynamic VAM and its standard deviation for the tested specimens. The results stem from a synthetic signal, generated from $p = 8$ points from each of $n = 2$ static load levels at $f_s = 2$ MSa/s.

Specimen	Averaged difference dB	Deviation dB	 %
GFRP 1	2.254 ± 0.447	0.154	0.73
GFRP 2	2.302 ± 0.418	0.202	0.97
Aluminium 1	1.828 ± 1.329	−0.272	−1.26
Aluminium 2	1.761 ± 0.804	−0.339	−1.86

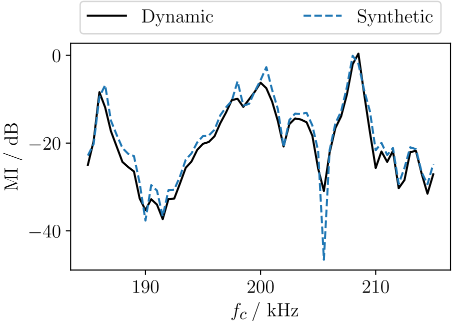

Figure 5.11.: Comparison between the MI of the dynamic and synthetic VAM from an aluminium specimen after a fatigue load of 10.000 cycles.

rier frequencies. These strong fluctuations result from the pronounced resonances of the material. Figure 5.11 presents a comparison between the synthetic ($n = 2$,p=8, $f_\mathrm{s} = 2$ MSa/s) and dynamic MI after a fatigue load of 10.000 cycles. Similar to the GFRP specimen, the highest differences between both methods occur in proximity to the extremes of either weak or strong modulations (e.g. 206.5 kHz). Therefore, the mean deviation (approximately 0.34 dB) worse and results in -1.3 to -1.9 %. However, these deviations are negligible compared to the MI increase of $10 - 30$ dB due to damage that is reported in the literature [97, 135]. The mentioned deviations are compared for all specimens in Table 5.1. Additionally, parameter studies are provided in Table A.4 and A.5 of the Appendix.

5.5. Comparison of VAM with continuous and non-continuous carrier vibrations for the impact detection in GFRP

Further evaluations of the synthetic VAM were performed on three GFRP specimens with a width of 70 mm, as introduced in Figure 5.6. In addition to the piezoceramic actuators, a strain gauge (HBK LY41, HBK Germany) was applied to the specimens with a dedicated adhesive (HBK X60, HBK Germany). The strain gauge was connected to the NI-USB 6366 through an amplifier (HBM MGCplus AB22A). This setup allows for the correlation of the carrier vibration with the actual stress that is present in the structure. The testing process was adapted from the prior GFRP specimens. However, the first damage was introduced as barely visible, low-velocity impact damage (BVID). The BVID was introduced with a light tap of a hammer on a steel ball (diameter of 15 mm) to mimic a “tool-drop”, while the specimen was subjected to a stress of 47.6 MPa. The impact itself was not observable, but two small inter-fibre defects were introduced, magnified in Figure 5.12 (left inset). The occurrence of two cracks indicates, that the steel ball rebounded and hit the specimen twice. Further damages were introduced by subsequently increasing the tensile stress to surpass the “knee stress” resulting in inter-fibre fractures in the 90° layers of this cross-ply laminate.

After each of the mentioned loading cycles (including the BVID), VAM measurements were performed at three different stress amplitudes to evaluate the influence of varying stress conditions during a VAM measurement. The lowest amplitude of $2 - 20$ MPa is comparable to the test setup of the 30 mm wide

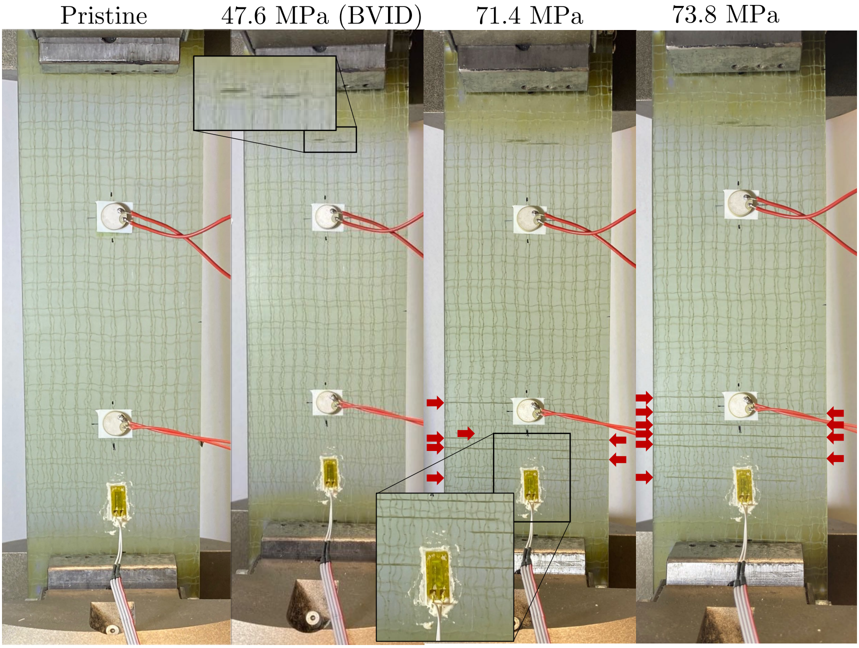

Figure 5.12.: The specimen is shown at each damage state. The inset at 47.6 MPa also marks the location of the impact. Note that after 71.4 MPa a crack appears below the strain gauge, as shown in the bottom inset.

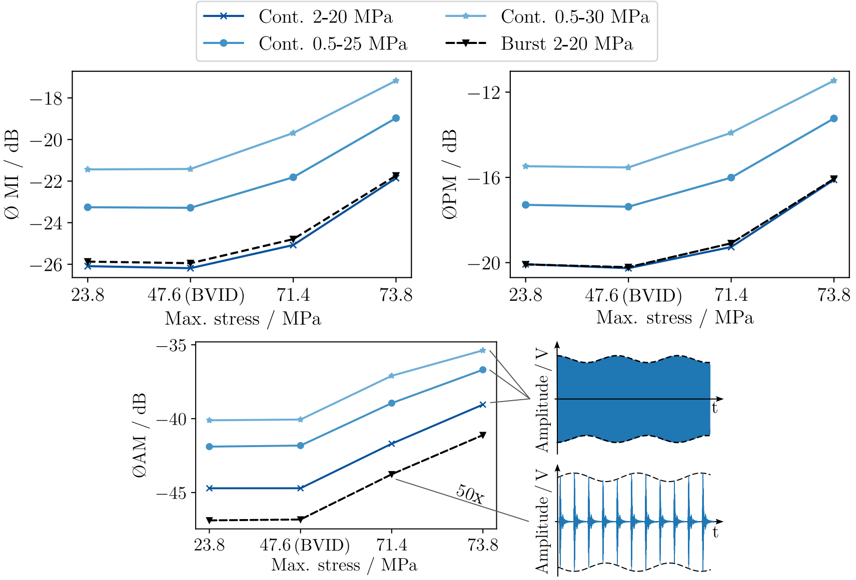

Figure 5.13.: Averaged MI (top left), PM (top right) and AM (bottom) from the three pump amplitudes are compared. Furthermore, the results from the burst excitation are included in each graph. A pictogram indicates the difference between the resulting measurements.

specimens, discussed in Chapter 5.4. The VAM measurements with the stress amplitude of $0.5 - 25.0\,\mathrm{MPa}$ and $0.5 - 30.0\,\mathrm{MPa}$ were utilised as comparison and to calculate the synthetic VAM from a dynamic signal, as illustrated in Figure 5.4.

During the pump vibration X_p, and at static stress levels $\sigma_\mathrm{l} = 2, 11, 20\,\mathrm{MPa}$, a series of 50 tone-bursts were introduced into the specimen and measured with the piezoceramic actuators. These tone-bursts consist of a 5-cycle sine, multiplied by a Hanning window, and were subsequently sent with a delay of 1 ms. Utilising these bursts results in an energy reduction for the carrier-excitation by over 98 %, compared to a continuous excitation. The carrier of both excitation methods was introduced with an amplitude of 6 V (doubled by a buffer), in a frequency range of $180 - 235\,\mathrm{kHz}$ (steps of 0.5 kHz). Hence, the responses at 111 frequencies were acquired at each damage state and per method.

In Figure 5.13 (top left), the averaged MI is shown for the different damage states at the three tested amplitudes of X_p. It is shown that the introduction of the

BVID influences the MI minimally. At the stress amplitude of $2-20\,\mathrm{MPa}$ the MI even decreases slightly, which is in contrast to the expected behaviour and could be attributed to changes in the stress amplitude, introduced damage by the grips of the testing machines, or the orthogonal impact itself. A similar phenomenon was observed in aluminium specimens by Dorendorf *et al.* [71]. However, the subsequently introduced inter-fibre cracks, through the higher loads result in a notable increase in the MI. Also, a larger amplitude of the pump wave X_p increases the MI as well. The initial MI at the stress amplitude of $0.5-30.0\,\mathrm{MPa}$ is higher than the MI with the most damages, which was measured at a stress amplitude of $2-20\,\mathrm{MPa}$. Furthermore, the MI shows a high correlation with the amplitude of X_p in this experiment. As an effect, the slopes of the MI are nearly identical between the three amplitudes. These drastic differences in MI underline the relevance of a constant load amplitude to allow a comparison of the VAM measurements. The dashed lines in Figure 5.13 illustrate the equivalent evaluation of VAM, where the carrier consists of subsequent burst signals. Interestingly, the MI of both carrier excitation methods is almost identical. Consequently, an MI-based VAM analysis is feasible with burst excitation, which reduces energy consumption. The BVID results in no significant MI increase with this method either.

All signals were further evaluated with the STFT algorithm[1] to separate the modulation into AM and PM, to evaluate if the introduced damages are detectable by a certain type of modulation. Figure 5.13 (top right) shows, that the slope of the PM is consistent with the results of the MI. Again, the BVID results in a slight decrease in PM, while subsequent damages cause a notable increase in PM. Also, the PM of the burst VAM is identical to the slope from the continuous excitation at the amplitude of $2-20\,\mathrm{MPa}$.

In contrast, the AM of the burst VAM measurements is much lower compared to the continuous excitation. For illustration purposes, the AM of the burst excitation is multiplied by 50 (which was arbitrarily chosen for a similar range). The slope of the AM after this multiplication becomes identical to the continuous AM measurements. However, this reduced amplitude of AM can be attributed to the lower energy of the burst signal. It can be observed, that the slope of the AM (Figure 5.13 bottom) differs slightly from the MI. Interestingly, the BVID does not result in a decrease in the AM, which is in contrast to the prior results and can not be explained.

---

[1] Based on the approach presented by Oppermann *et al.* [12]

This comparison has shown, that both excitation methods perform similarly if the dynamic modulated signal is evaluated. However, the bursts offer more information. As already shown in Figure 5.5, each measured burst shows “fingerprint patterns” of several peaks in the envelope of the signal (calculated with the Hilbert-transform). The strongest wave package, which arrives first, is a superposition of antisymmetric A_0 lamb-waves (as elaborated in Chapter A.2), that travelled the straight path between both piezoceramics or as direct reflections on the long sides of the specimen. This assumption is based on the time of the arrival and the typical wave speeds of Lamb waves in FRP materials. The later “peaks” in the signal can be attributed to longer signal paths due to more reflections at the boundaries. Analogous to the main idea of the synthetic VAM, the amplitude difference of these peaks due to the stress changes can be calculated. In Figure 5.14, the amplitudes of the peaks at a stress of $\sigma_\mathrm{l} = 2\,\mathrm{MPa}$ were subtracted from the amplitudes at $\sigma_\mathrm{l} = 20\,\mathrm{MPa}$. Interestingly, the slope of the three evaluated peaks differs. Due to the BVID, the difference of A_{P1} decreases slightly, which is not expected since the damage is not located in the signal path and should not influence the amplitude. At the third peak A_{P3}, the difference stays constant after the BVID. At the fourth peak, where the signal travels the longest path, the difference increases due to the BVID and the subsequent damages. Based on these results it is speculated, that either the connection between the piezoceramics, introduced damages in the clamping area, or that the specimen has changed. The BVID could influence the stress in the 0° layers and has therefore affected the area between the piezoceramics and hence the amplitude of the direct propagation. However, the introduced inter-fibre fracture with a tensile load results in a prominent increase in the amplitude difference for all

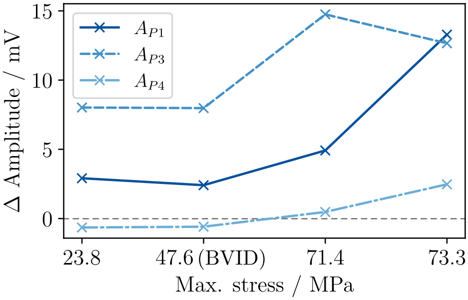

Figure 5.14.: Amplitude difference of the individual impulses between the measurements at $\sigma_\mathrm{l} = 2\,\mathrm{MPa}$ and $\sigma_\mathrm{l} = 20\,\mathrm{MPa}$.

evaluated wave packages. It should also be noted, that each resulting peak in the envelope results from a superposition of several wave-propagation paths through the specimen. The introduced damages alter the reflections of the lamb waves and consequently also the amplitude and time of arrival of each peak. Especially for the second peak (of the pristine measurement), the inter-fibre fractures have changed the shape of the resulting envelope. Therefore, the amplitude and also the time of the maximum are not constant and can not be compared. A similar behaviour is observable for the third wave package. At the last damage state, a separation into two smaller signals is observable, which explains the sudden decrease even though the damage is stronger.

Additionally, the dynamic VAM measurements can be evaluated more deeply with the synthetic VAM. In Figure 5.15, the results from the traditional dynamic VAM approach are compared to the synthetic VAM, which was reconstructions from just the minimal and maximal stress ($n = 2$). The signal for the synthetic VAM was also down-sampled from 2 MHz to 4 kHz and just 5 points at each step were used, compared to the $2,000,000$ points measured at the high sampling rate for each dynamic signal. Reducing the sampling rate even below 4 kHz is possible but not necessary since such a sampling rate is achievable by many low-power devices. These reduced parameters are sufficient to reconstruct the dynamic measurements as well. However, a slight decrease in MI during the first damage states is also evident for these synthetic VAM measurements.

Analogous to the evaluation of the difference in amplitude of the bursts, with the synthetic VAM the individual amplitudes and phases at chosen stress levels σ_l of a continuous excitation can be evaluated and used for a damage detection as well. Note that all values were estimated from 5 points at 4 kHz of the con-

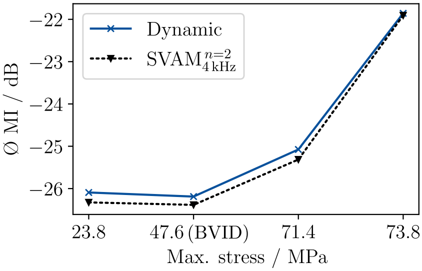

Figure 5.15.: Elongation measured with a DMS, AMP and phase is extracted and composed signal is created.

tinuously excited carrier during the dynamic stress amplitude of 0.5 – 30.0 MPa. Figure 5.16 (left) shows the extracted amplitude (top) and phase (bottom) of each frequency after the BVID. Also, the measured phase was in the range of $0 - 2\pi$. The preprocessing is shown in Figure A.12 of the Appendix. The measurements at the stress levels of $\sigma_\mathrm{l} = 2\,\mathrm{MPa}$ and $\sigma_\mathrm{l} = 20\,\mathrm{MPa}$ are compared, as they were used of the synthetic MI of Figure 5.15. The difference between both lines essentially resembles the modulation due to the stress variation of X_p. Interestingly, the measured amplitude increases with higher stresses at several frequency ranges, but decreases in others. The same phenomenon is visible for the phase, while these areas do not necessarily coincide. Consequently, the overall modulation is a superposition of both modulations (and probably more influences). At some frequencies, AM has a higher influence and at others PM, which is in contrast to the ideas of Donskoy *et al.* [206] or Ramezani [126], where the different modulations were correlated to different types of damage. The assumptions of these works may hold for a certain frequency range at some specimens, but not without restrictions.

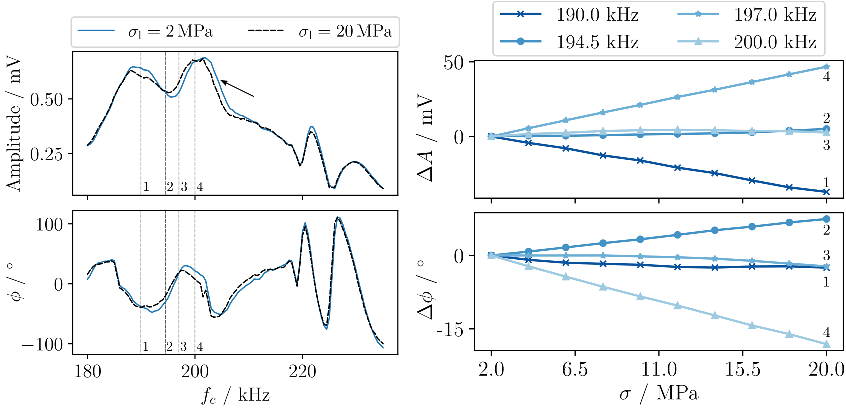

Figure 5.16.: Compression of the amplitude (top left) and the phase (bottom left) between the low and the high-stress level. The difference between the curves of both stress levels is essentially the amplitude or phase modulation. The slope of amplitude (top right) and phase (bottom right) is depicted over the applied stress level for specific frequencies. It shows that the change of each quantity is dependent on the evaluated frequency, and can increase or decrease with higher stress.

In the shown frequency range of Figure 5.16 (left), four carrier frequencies f_c were highlighted, which are either governed by a large difference between both levels or none at all. The amplitudes and the phases of these frequencies are shown over the stress range in Figure 5.16 (right) for ten stress levels at which they were extracted from the dynamic signal. While specific frequencies show a near linear increase or decrease, there are also frequencies where first an increase and a subsequent decrease occurs. Especially the latter ones are relevant in this evaluation since the modulation due to the change is not evident in the synthetic VAM. This phenomenon was already addressed in the initial publication [11] about the synthetic VAM and can be compensated by increasing the number of levels n.

Similar to the evaluation of the bursts, also the amplitude and the phase (shown in Figure 5.16 (left)) of the continuous excitation were subtracted and averaged. The calculation follows the equations 5.2 and 5.3, where j counts through the measured frequencies.

$$\Delta A = \frac{1}{j} \sum_{i=1}^{j} \left| A_i^{20\,\mathrm{MPa}} - A_i^{2\,\mathrm{MPa}} \right| \tag{5.2}$$

$$\Delta \phi = \frac{1}{j} \sum_{i=1}^{j} \left| \phi_i^{20\,\mathrm{MPa}} - \phi_i^{2\,\mathrm{MPa}} \right| \tag{5.3}$$

The results are shown in Figure 5.17. Interestingly, both of these two values increase with each introduced damage, even after the introduction of the BVID. Since these results from this precise evaluation show the expected increase due to the damage, and they were calculated from just 5 points of each stress level of the downsampled signals, it suggests many new possibilities for a more thorough evaluation of VAM.

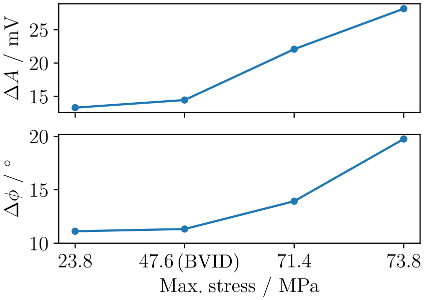

Figure 5.17.: Mean absolute difference between both stress states calculated for the amplitude (top) and phase (bottom).

5.6. Application of synthetic VAM to complex structures

The previous chapters have demonstrated and discussed the application of the synthetic VAM for SHM at rather simple specimens. To evaluate the applicability of VAM and especially the synthetic VAM to structures of increased size, complexity and material thickness, two studies on more complex structures were conducted and will be discussed in the following Section.

5.6.1. Section of a wind turbine blade

The first specimen is a substructure of a rotor blade that was in service for about 20 years on a 1.5 MW wind turbine located near the shore in northern Germany. The tested structure was extracted from the central structure around the shear webs and near the tip of the blade. This structure is a typical example where the online damage detection could be much more economical compared to the currently available health monitoring described earlier. Especially, detecting the occurring damage with the estimation of a remaining service life would prolong the maintenance cycles, reduce the overall waste from still intact structures and decrease the inspection costs.

To accommodate the structure inside the hydraulic testing machine (Instron 100 kN), the leading and trailing edges of the blade were cut at a distance of 30 mm from the shear webs inside the wing assembly. The resulting structure was shortened to a length of 665 mm. The origin of the structure with the cuts made to achieve a suitable specimen is depicted in Figure 5.18 a). The dimensions and location of the piezoceramics and strain gauges are given in Figure 5.18 b).

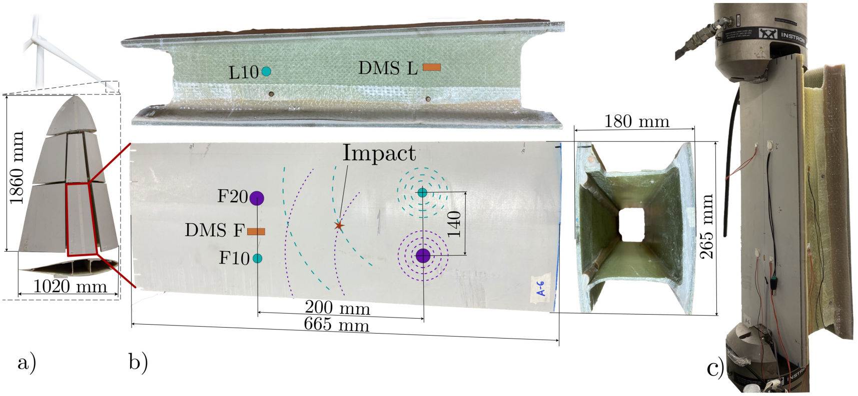

Figure 5.18.: Sub-structure of a wind turbine blade containing the shear web with the surrounding front and backside of the wing. The origin of the structure a), the dimensions and locations of piezoceramics b), and the test setup in the laboratory are displayed c).

The fibre volume content of the laminates was tested by burning epoxy-matrix material and resulted in 45,22 % for the shell and 42,99 % for the shear web. From a burned specimen and by evaluating the cutting surfaces, a layup with $[\pm 45/0_3]_\mathrm{s}$ was identified for the shell, with an additional layer of unoriented short-fibres of approximately 50 mm length on the outer surfaces. The shear web is built with a quasi-isotropic layup with $[\pm 45/0/90]_3$.

In Germany, most insurance claims of wind turbines can be attributed to damaged blades, resulting from *e.g.* birds, ice or hailstorms. Consequently, its detection is of high interest for the SHM of these structures. Since the original stress state of this blade was not reproducible in the lab, the evaluation of the front surface was prioritised. Consequently, in this experiment, the grips of the testing machine were attached to the front surface for the introduction of the pump wave X_p, as shown in Figure 5.18 c). The force amplitude of $F_\mathrm{p} = 1.5 - 15\,\mathrm{kN}$ was selected to mimic the in-service loads, which are used as ambient vibrations for the VAM but more importantly also the synthetic VAM evaluation. Note that the height and distance between the shear webs decrease slightly towards the wing tip. Consequently, only the applied loads are given in this chapter. Due to the mounting of the specimen, the main stress will occur on the frontal surface, and the occurring stresses in the shear webs and on the backside will be of lesser magnitude.

For the impact detection with VAM, four piezoceramics were mounted with double-sided tape (Tesa 56172) to the front side of the wing, as shown in Figure 5.18 b). The high laminate thickness of 8 mm and the junctions in the structure pose a new challenge to the application of VAM. Hence, two frequency ranges ($90 - 110$ kHz and $185 - 215$ kHz) were tested, to evaluate if an increase of the wavelength—with its affect on the Lamb-wave characteristics—is beneficial for the damage detection. Each frequency range was excited by a distinct piezoceramic disc actuator (PIC255 from PI Ceramics with a diameter of 20 mm × 2 mm and 10 mm × 2 mm). Both exciting piezoceramics were attached at a distance of 140 mm on the upper half of the structure. Additionally, piezoceramics of both dimensions are mounted as sensors on the bottom half of the structure (F10 & F20) with a distance of 200 mm to the upper piezoceramics. Sensing piezoceramics were attached in the centre of the left shear web (L10) and centred on the backside (B10) as well.

To evaluate the sensitivity of VAM towards impact damages in such complex structures, subsequent impacts were introduced onto the front surface between the piezoceramics, with an increasing impact energy. The location of the impact damage is indicated in Figure 5.18 b). The first damage was achieved by a moderate tap with a hammer on a steel ball of 15 mm diameter. After the VAM measurement, the velocity of the hammer was subsequently increased, until the damage state with index 6. Consequently, the damage size should increase subsequently, as well as the modulation in the measured VAM signals.

Note that in the following, only the results for the excitation with the 10 mm piezoceramic are shown. The results of the 20 mm actuator do not show the expected behaviour but can be found in the Appendix (*cf.* Figure A.14). This difference between both actuators could result from the increased wavelength, unfavourable locations of the piezoceramic actuators or other factors, such as an incomplete coupling between the larger actuator to the curved surface of the blade.

The results of the traditional VAM analysis (from the 10 mm piezoceramic) are shown in Figure 5.19 (left) from the two measuring piezoceramics (10 & 20 mm) at the front, the one at the side and the one at the backside of the structure. As expected, both the signal strength and the modulation are the strongest for the measurement on the front surface (F10). At this piezoceramic, the MI curve indicates an upward trend that correlates with the increasing damage. For illus-

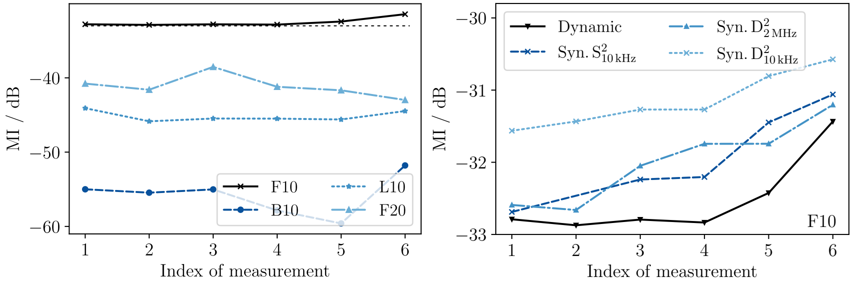

Figure 5.19.: Evaluation of the MI for each side with a frequency range of 185-215kHz (left). Each point represents the mean MI of the whole spectrum. The MI of the front side (F10) is additionally compared to the synthetic MI calculated from static carrier measurements (right).

trating purposes, a horizontal line marks the amplitude of the first measurement. Despite being located on the frontal surface as well, the measured modulation with the bigger piezoceramic (F20) is much lower compared to the smaller one. This can result from the unfavourable resonance frequency (which is half as high compared to the smaller piezoceramic) or problems with the bonding to the structure as well. Also, the modulation on the left (L10) and the back surface (B10), do not indicate an increasing damage or a clear trend. Note that the modulation for the measurements at the left and back sides is relatively low since a difference of 3 dB indicates a halving of the MI in voltage. Furthermore, the impact damage and subsequent delaminations are relatively small and localised on the frontal surface. Consequently, the impact damage is not in the direct signal path between the exciting piezoceramic and the receiving ones (F20, L10 or B10). Also, the shear web on the sides is bonded to the plate-like frontal surface, which hinders the propagation of the carrier wave due to the increased local stiffness. The unfavourable propagation of the carrier vibration into the shear web results in a low amplitude of the measured signal. Consequently, the signal-to-noise ratio of the measurements at the shear web and the backside is higher, and the modulated waves, due to the impact, are concealed from unmodulated waves of a more direct propagation path. So, the sensors located on the shear web or the backside were insufficient to detect the impact on the frontal surface.

Two synthetic VAM variants were applied to the measurements at the front surface (F10), where the stress change due to the testing machine is the strongest.

Firstly, a synthetic MI was calculated from measurements, where only the carrier vibration X_c was introduced at the static stress levels σ_l. These static computations will be denoted as Syn.S. As before, the measured signals were downsampled[2] to 10 kHz and the signal was reconstructed from $p = 10$ points at both steps $n = 2$. Furthermore, the synthetic VAM was extracted from the dynamic VAM measurements. At two stress levels, which were chosen to be slightly in between the dynamic load, the signal was approximated to reconstruct the VAM signal. These measurements are denoted as Syn.D. Since one of the main advantages of the synthetic VAM is the evaluation of undersampled data, the sampling rate of the signal is given in the subscript and the number of steps used for the computation in the superscript. Hence, $\mathrm{Syn.D}^{2}_{10\,\mathrm{kHz}}$ denotes a synthetic signal extracted from the dynamic measurement with two steps and a sampling rate of 10 kHz.

In Figure 5.19 (right) the dynamic MI is compared to the synthetic computations for the front surface. Note that the expected offset of 2.1 dB was already subtracted from the results, to improve the comparability. In this magnification, it can be seen, that the dynamic MI fluctuates slightly due to the first impacts, but increases significantly at index five and six. In contrast, the graphs of the synthetic generated modulations are increasing with every damage, which indicates a higher sensitivity to the damage. The overall increase in MI is comparable to the dynamic measurement. Interestingly, the modulation of the highly down-sampled signals $\mathrm{Syn.\,D}^{2}_{10\,\mathrm{kHz}}$ is deviating more from the dynamic VAM measurements, by being slightly higher. It was observed, that the amplitude of the elongation measured with the DMS varied slightly between the measurements, which could explain the difference between the dynamic and the synthetic measurements. This experiment further underlines, that applying the synthetic VAM method in this complex structure results in a similar (or slightly increased) sensitivity compared to a traditional VAM measurement. Additionally, even down-sampled signals of $f_\mathrm{c} = 10\,\mathrm{kHz}$ are sufficient to reconstruct the dynamic response.

---

[2] A prime number of 197 was chosen which results in 10.15 kHz, since down-sampling the original signal (acquired at 2 MHz) by the factor of 200× would result in artefacts, which increases the error.

5.6.2. Thick walled composite cuboid

The second complex structure, used to evaluate VAM and especially the synthetic VAM method is a cuboid made from biaxial GFRP. The wall thickness of this cuboid is 10 mm, which is even thicker than the previously tested blade structure. The laminate consists of 16 layers of woven glass rowings (Valmiera Glass 05507-FK144) in an orientation of ±45°, which was impregnated with a polyurethane matrix material (Henkel Loctite Max 2, $T_\mathrm{g} = 100°\mathrm{C}$). Due to the braiding process around the mandrel, the layers are not fully symmetrical. The resulting fibre–volume fracture is estimated as 49 %. In contrast to the prior tested specimens, this structure was loaded in compression (45 – 450 kN) and torsion (1.8 – 18 Nm) concurrently with a frequency of 3 Hz. This testing procedure was achieved by using a Hexapod-based test machine that allows multi-axial loading conditions in all six degrees of freedom for static and dynamic experiments. The load ranges were chosen to be close to the limits of the load cell (500 kN). The tests were furthermore performed at the elevated temperature of 70°C inside a temperature chamber, as defined in the project from which this structure originates [207]. The structure was preheated within the temperature chamber for 2 h to reach an equilibrium prior to each test. For the VAM mea-

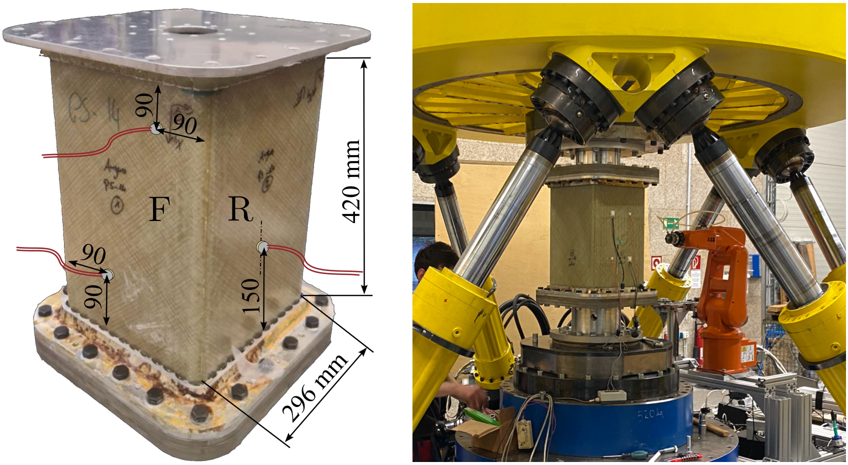

Figure 5.20.: The dimensions of the GFRP cuboid and locations of the piezoceramics (left). The front (F) and right (R) surfaces are marked. The piezoceramics on the right side and the surface were attached centred with a height of 150 mm. The Hexapod with the mounting of the structure is shown on the right (without the climate chamber).

surements, two piezoceramics (10 mm × 2 mm PIC255 from PI Ceramics) were mounted on the front side of the structure. Only this smaller actuator size was used since it performed better in the prior experiments. Due to the increased temperatures, the piezoceramics were mounted with a 2k epoxy adhesive (Uhu Endfest) instead of double-sided adhesive tape. The upper piezoceramic was used for the excitation of the carrier vibration, and the lower piezoceramic was used as the sensor to acquire X_r. Furthermore, one piezoceramic was added as a sensor on the right surface of the specimen and one as a sensor at the back surface of the structure. Alongside the vibration, the strain was recorded with two strain gauges (HBK LY41) which were connected through a Wheatstone bridge to the data acquisition board. The strain gauges were aligned with the compressive load and bonded to the structure with a dedicated strain gauge adhesive (HBK X60) in the centre of the frontal and the left surface of the cuboid. The dimensions and locations of the piezoceramics and strain gauges are given in Figure 5.20, and further images can be found in Figure A.16 of the Appendix. The VAM measurements were conducted simultaneously at the three sensing piezoceramics and the strain gauges to correlate the strain to the vibrational response X_r.

Since the Hexapod allows movement in six degrees of freedom, initial stress-controlled experiments have resulted in an unexpected loading behaviour of the structure. Therefore, the fatigue load of the experiment was controlled by the Hexapod's displacement, in contrast to the prior experiments, where the actual stress (or force) was the controlling parameter. The displacement of the fatigue experiment was defined before the first cycle, to reach the defined fatigue amplitude. After 162.000 cycles, the amplitude was redefined, since the stress amplitude has decreased over time.

Shown in Figure 5.21 is the amplitude of the elongation resulting from the fatigue load. Higher values indicate an increasing compression. The shown elongations were measured alongside the VAM experiments with the strain gauges connected to the data acquisition board. The compression and torsion were measured with the load cell of the Hexapod at every fatigue cycle. The unusual upward trend of the elongation can be attributed to a superposition of internal heating (due to the energy dissipations of the fatigue load due to internal friction, especially pronounced around the defects), the visco-elastic behaviour of the polymeric matrix material and the occurrence of inter-fibre damages in the structure. Prior tests of a similar structure have shown that these dissipations increase the actual

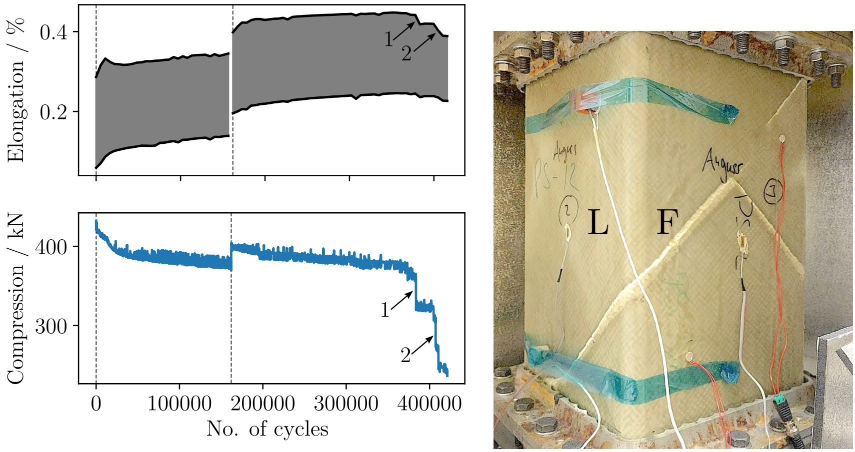

Figure 5.21.: Elongation and amplitude of the compressional fatigue load over the lifetime (left). The dashed lines mark the definition of new fatigue parameters and the numbers indicate the two major progressions of damage. The damaged structure after the experiments shows the fibre buckling damage (right).

temperature of over 10°C, which also slightly influences the measurement of the strain gauges.

After 162.000 cycles, the parameters of the fatigue load were newly calibrated, and all screws of the connection to the Hexapod were tightened, which increased the stiffness of the overall system. As a result, a step in the amplitude of the elongation and of the compression during the fatigue loading occurs (marked by a dashed vertical line in Figure 5.21 left). After around 380.000 cycles, the first buckling damage occurs (marked as first damage), which decreases the measured strain amplitude due to higher elongations around the damage and, consequently, the overall stress. The final damage occurs at 410.000 cycles, shortly after which the VAM measurements were ended due to extensive fibre buckling damage on three sides of the structure. This buckling damage is shown in Figure 5.21 (right) as lighter areas/lines with an angle of ±45° to the loading direction.

During the fatigue loading of the structure, VAM measurements were acquired every 30 min (5400 cycles) for 61 carrier frequencies ($f_c = 190 - 220\,\mathrm{kHz}$ with a distance of 0.5 kHz) and a duration of 1 s. The mean MI for each dynamic measurement over the lifetime is shown for all three measured surfaces in Figure 5.22 (top). The MI of the dynamic VAM does not follow the expected damage curve of such a laminate, as introduced in Chapter 2. The deviations result from the altered testing parameters during the experiment and the strain-controlled testing design. While the first measurements at the front surface follow the expected damage increase of the first stage of fatigue life, the second stage is interrupted by the decreased MI due to the new fatigue parameters (at 162.000 cycles). The slope before and after the step is slightly increasing, which is in accordance with the second stage of the fatigue life. The final stage is governed by a reduction of the MI, which indicates less damage and is in contrast to the actual condition. This reduction is also observable in other damage indices like R or β (which are not included in the picture). Hence, the traditional VAM method and evaluation do not detect the growth of damage in this specimen, and the final failure can not be predicted. This unexpected MI decrease in the third and final stage of the fatigue life can be attributed to the diminishing stress amplitude due to the damage combined with the strain-controlled design.

The MI of the first stage of fatigue life measured on the right surface is governed by an increase. After 30.000 cycles, the MI decreases over time, which does not represent the actual damage as well. The updated fatigue amplitude also results in a sudden MI decrease. After 90 % of the lifetime, the first damages

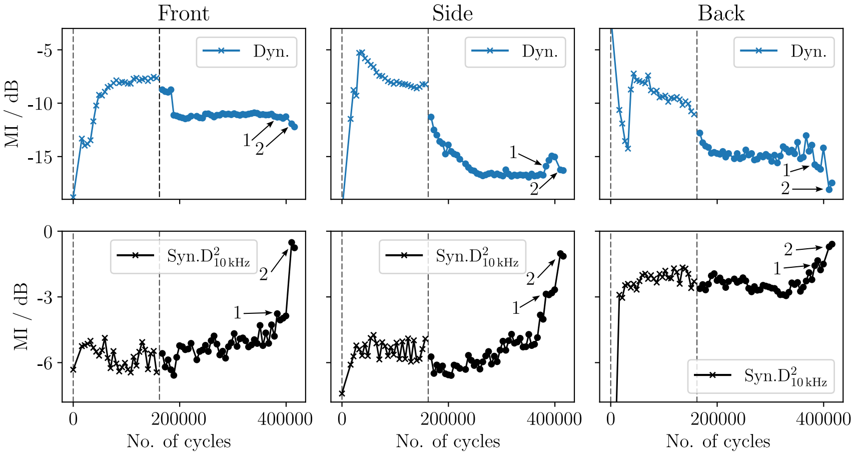

Figure 5.22.: Comparison of the MI calculated from the traditional dynamic method (top) and the synthetic approach (bottom), where the data is extracted from dynamically acquired measurements downsampled to 10 kHz at two stress levels.

result in the MI increase of about 3 dB. However, after 95 % of the lifetime, the MI decreases. Therefore, the ultimate failure is masked by the decreasing MI due to the measured stress amplitude. On the backside of the structure, the MI shows an intense fluctuation in the first and third stages of fatigue life, which also hinders a precise assessment of the specimen's health.

In Figure 5.22, the synthetic MI is shown below the dynamic measurements for each surface of the cuboid. The measured elongation was used to define the individual levels σ_l for the synthetic VAM. As mentioned before, the synthetic VAM allows to compensate for changing and decreasing stress amplitudes by choosing stress levels that regularly occur during the ambient vibration. However, the increasing elongation over the lifetime in this experiment (*cf.* Figure 5.21) prevents using constant values for the definition of the individual stress levels. Consequently, only the choice of a constant amplitude for the synthetic VAM was practical. Despite, the expectation that the changing overall stress is less precise than defined stress levels, it should be more precise than the traditional VAM evaluation. The two levels of the synthetic VAM were defined by selecting the minimal elongation of the dynamic measurement[3] as the first level and adding a constant elongation of 0.15 % to calculate the second level. This amplitude is shown in Figure A.15 in the Appendix. From ten sequentially acquired points ($p = 10$), measured while the elongation was closest to the corresponding load level, the amplitude and phase of the dynamic signal were approximated. Using these approximations, a synthetic signal was then reconstructed, which allowed for the calculation of the MI. Note that the dynamic signals used for the synthetic VAM evaluation were downsampled from $f_\mathrm{s} = 2\,\mathrm{MHz}$ to $f_\mathrm{s} = 10\,\mathrm{kHz}$. This downsampling was performed to validate that the requirements on the sampling rate can be significantly reduced.

Generally, the slope of the synthetic MI differs strongly from the dynamic MI, at all three surfaces of the cuboid. Despite the smaller stress amplitude, the synthetic MI is much higher than the dynamic measurements. This is in contrast to the tests on the coupon specimen, where the decrease of the amplitude resulted in a decrease in the MI. Also, the offset of 2.1 dB for the synthetic VAM is neither evident nor expected in this evaluation since the stress amplitudes differ. While the noise is more pronounced in the synthetic MI due to the undersampling and the usage of just two stress levels, all three curves show an increasing MI over

---

[3] The minimal elongation was multiplied with 1.05, to ensure that the elongation was present in all measured frequencies at the damage state.

the lifetime. At the front surface of the cuboid (Figure 5.22 bottom left), the modulation decreases slightly in the first 100.000 cycles. A clear upward trend is observable afterwards. The first and second major damages can be identified in the graph, as significant increases in MI, especially for the second damage state. Furthermore, in contrast to the dynamic measurements, the constant stress amplitude eliminates the jump of the MI due to the updated testing parameters of the Hexapod after 162.000 cycles.

For the measurements on the side (Figure 5.22 bottom middle), the MI increases over the first measurements, followed by constant MI measurements of high noise, until the testing parameters were adjusted. The step due to the adjustments is larger compared to the synthetic MI of the other two surfaces. After 162.000 cycles, the MI constantly increases until the first and second fibre-buckling damages are observable by an intense increase of MI, which indicates the presence of damage. Interestingly, the two prior measurements show indications of a damage, by an increase in MI, which is not as evident in the measured elongation or any other evaluation. The synthetic MI measured at the backside (Figure 5.22 bottom right) follows the ideal damage curve closely, until the adjustments. Afterwards, no noticeable step in MI is apparent, after which it slightly decreases until approx. 330.000 cycles. Even before the obvious damages, the MI increases, indicating also a continuous damage progression.

Interestingly, the MI at the side increases most after the first damage (around 380.000 cycles). In comparison, the front surface MI increases significantly with the second damage (around 410.000 cycles). These differences indicate that the buckling damage was initiated on the side before the second damage also influenced the signal path of the frontal piezoceramics. For the measurements on the backside, the MI increases more constantly, and both damage events are not as concise compared to the other surfaces. This constant increase indicates a damage progression on the left surface or behind the right piezoceramic. Since the receiver has the same distance to the emitter around the left and the right surface of the structure, it is assumed, that damages around the structure are monitored. These observations indicate, that with an increasing size of the structure, the VAM method becomes less global. The evaluation of individual signal pathways is relevant since the amplitude of the carrier decreases over longer distances due to damping. Hence, the modulated Lamb waves due to damages influence the measured response less if they have a longer signal pathway. This relation can be compensated by applying more sensors, which would increase the precision of localisation even further, as indicated by Broda *et al.* [123].

Contrary to the impact detection on the rotor-blade structure of Chapter 5.6.1, an increase in MI is visible on other sides of the cuboid structure. This phenomenon results from the bent corners of the cuboid (in contrast to the adhesive-bonded webs of the wing) and the type of damage. Also, the thickness of the cuboid is constant. The inter-fibre fractures and buckling are present throughout the structure, influencing the carrier waves more intensively, compared to a localised impact damage.

6. Conclusion and Outlook

The interest in the vibro-acoustic modulation (VAM) has significantly increased in recent years due to its often-praised high sensitivity in detecting even minimal damage. Despite 30 years of VAM research and over 200 published sources, the method is still in its early stages. In the literature, several modifications were proposed to improve the sensitivity of the method (*e.g.* the impact modulation, the cross-modulation) and how to evaluate VAM (*e.g.* MI, β, sideband peak count). However, the applicability of these modifications was primarily validated under controlled laboratory conditions on relatively small specimens. The industrial application of VAM is still far from being realised due to the existing hurdles (*cf.* Chapter 2). Hence, this thesis has aimed to improve the applicability of VAM, with a focus on the evaluation of structures made from fibre-reinforced polymers. Two areas were identified, in which VAM would enhance the state-of-the-art. The first is the non-destructive testing (NDT) of specimens for defects that are challenging to detect with the current NDT methods. The second challenge is the application of VAM on industrial structures, where the damage state has to be evaluated over time. Consequently, two research hypotheses were formulated for each area in Chapter 1 and were individually addressed in Chapter 4 and Chapter 5.

The biggest challenge for the application of VAM in NDT is the lack of a physical baseline, which hinders the comparability of VAM measurements between different structures or specimens. The measured modulation is influenced by many factors, *e.g.* the location of the actuator and the receiving piezoceramic, the geometry of the tested structure, the laminate structure of the composite and the boundary conditions. To overcome this lack of baseline, it was assumed that measurements on similar specimens with constant boundary conditions could be compared. In addition, the applicability of a data-driven evaluation of these similar specimens was evaluated to improve the sensitivity even further.

A severe challenge, particularly in aerospace, is the detection of areas within an adhesive bond where the adhesion is reduced. To the author's knowledge, there is currently no NDT method that can robustly identify these so-called "weak bonds". Therefore, the first hypothesis was evaluated on a set of adhesive-bonded single-lap shear specimens, where two types of defects (release agent contamination and an inserted PTFE film) were incorporated into the bond. While PTFE films in the bond can be detected using ultrasonic scanning, these films may eventually be found with VAM as a global damage evaluation. The detection of release agent contaminations on the other hand is challenging and no NDT method has so far not been approved for a reliable industrial applicability.

Before the mechanical testing of the 33 single-lap shear specimens, VAM measurements were conducted. However, neither the evaluation with the commonly calculated "Modulation Index" (MI) nor any other introduced damage parameter allows to differentiate between pristine and release agent contaminated specimens. Only the MI at specimens with inserted PTFE films is increased, but still in the standard deviation of the MI from the other classes.

To address this limitation, a data-driven classification of the specimens was proposed in this thesis by training artificial neural networks (ANN) on the scaled sideband amplitudes and the carrier of the measured modulated signals. This data-driven approach surpasses traditional VAM evaluation methods, such as simple summation of sideband amplitudes or linear combinations of them, by "learning" specific patterns present in the data. The results demonstrate a substantial improvement in detecting contaminations in the bond line, achieving a classification accuracy of 93.4 %. It was demonstrated that evaluating more sidebands increased the accuracy of the models, and that the carrier frequency significantly influences the resulting signal. Consequently, these high accuracies were only accomplished when a narrow frequency range was used for training and classifying the samples.

These precise predictions by the algorithm implicate the presence of relevant patterns in the VAM measurements. Consequently, the data-driven VAM analysis not only effectively differentiates between contaminated and pristine specimens but also, when conducted thoroughly, indicates how the introduced bond line defects affect the VAM signal. First evaluations of the trained ANNs, by calculating two types of feature importance, reveal that the limited relevance of the first sidebands hinders the detection of the bond line flaws with the traditional

MI (and the other parameters). This experiment also showed a high influence on where the piezoceramic actuators were located. Unfortunately, the destructive nature of determining the maximal shear stress prevented further elaboration on this aspect in this work. Therefore, an in-depth assessment of optimal sensor placement, along with considerations of the distance to the area of interest and proximity to the clamping area, emerges as crucial for the robust application of VAM.

A subsequent review of welded steel specimens with introduced crystallisation damages confirmed this enhanced sensitivity from the data-driven VAM evaluation. First indications of why specific carrier frequency ranges were more “information-rich” compared to others—allowing a more precise prediction—were found. Visualising the eigenmodes of several frequencies in these specimens with a 3D laser vibrometer indicates that the most accurate ANNs were trained with carrier frequencies that also exhibit a substantial magnitude of their modal vibration at the location of the weld/defect. This finding supports the formulated “necessary conditions of modulation” from Lim and Sohn [127]. Furthermore, it also explains the often proposed frequency sweep in a VAM analysis of an unknown structure, as it increases the probability of finding the “right” carrier excitation. This “trial-and-error” methodology could be overcome by further research, if the eigenmodes of the specimen are already known. With this knowledge, the evaluation of distinct modes would improve the sensitivity and even the reliability of VAM.

Also, further research is needed to apply this methodology to industrial structures. These trials should evaluate specimens with an increased dimension, increased bond lines, or even different locations and severities of the contaminations. Furthermore, it is worth evaluating whether a similar accuracy is attainable when the contamination of the adhesive bond is not in the direct signal path or even in the principal stress direction of the pump vibration. These subsequent experiments would require a specimen or structure, where *e.g.* the adhesive bond with its contamination is formed to a stringer or other stiffening elements.

It should be noted that this supervised data-driven approach by training ANNs on a specific task is well-suited for the evaluation of many similar specimens, which can be found exemplary in mass productions. However, variations in the specimen dimensions, adaptations to the manufacturing processes, or changed environmental influences may require the retraining of the ANN, the creation of individual ANNs for each application or a more sophisticated machine-learning approach. Another possibility to address these changes would be the application of *transfer learning*, where only the last layers of an ANN are retrained. This process drastically reduces the effort and amount of required training data to adapt to *e.g.* modified specimen dimensions.

Furthermore, it should be evaluated if an increased size of the tested structure, where the excited carrier vibrations rather show a transient character due to the long signal path, affects the sensitivity of the damage detection with VAM and the data-driven evaluation. In turn, the transient character of VAM could enable or even improve the application of a scanning evaluation of the structure, which was exemplarily performed with a laser vibrometer on the welded specimens. Hence, also the localisation of the damage (*e.g.* the weak bond, welding defect, and damage) or the severity could be assessed. Especially as an NDT method in production sites, the reoccurring evaluation with piezoceramics or a vibrometer could be feasible, in contrast to most SHM applications, where the sensors have to be integrated.

The *second part* of this thesis presents a leap in the applicability of VAM outside the laboratory for the structural health monitoring of industrial structures. Artificially exciting a distinct pump vibration of sufficient energy, which is essential for VAM, is neither feasible nor economical outside the laboratory. The favourable alternative is the utilisation of already present ambient vibrations in these structures, resulting from the in-service loads and environmental influences. However, these ambient vibrations are far from ideal and pose several challenges to the traditional VAM approach. Most importantly, ambient vibrations fluctuate over time due to varying service loads and changing environmental conditions. Additionally, the ambient vibrations manifest rather in a frequency range ($5 - 20\,\mathrm{Hz}$) than in a single frequency [146]. These variations hinder VAM research and complicate the integration of the traditional VAM approach into current structural health monitoring solutions.

To overcome this challenge, the *synthetic VAM* method was proposed in this thesis and addresses the second research hypothesis (see Chapter 1). This method combines the high-frequency response of the carrier at distinct stress levels into an approximated VAM signal, offering several advantages over the traditional VAM. The most significant advantage is the decoupling of VAM from the actual amplitude and frequency of the pump vibration X_p, provided it surpasses the stress levels that were chosen for the evaluation. Furthermore, the synthetic VAM method drastically reduces the requirements on the sampling rate and the length of the acquired carrier response. It was demonstrated on coupon specimens, that by utilising only eight data points at two stress levels (less than 0.016% of the original data points), the MI of the dynamic VAM signal is recreated with sufficient accuracy. Furthermore, the sampling rate f_s of these short measurements at each stress level can be reduced. Even sampling rates below 20 kSa/s (4.5% of the Nyquist rate), combined with the reduced number of data points, were sufficient to recreate the dynamic signal and approximate the MI with adequate accuracy. This was achieved by approximating the amplitude and phase from the resulting signal at each defined stress level and recreating the modulated signal with an arbitrarily chosen low frequency. This reduction in sampling rate and points translates to lower processing demands, reduced hardware costs, and consequently lowers the overhead for the monitoring of industrial structures.

Note that the synthetic VAM (especially if just two stress levels are evaluated), comes with the cost of less information in the generated signals, similar to any “analog-to-digital” conversion. Nevertheless, by including more stress levels σ_l into the synthetic process, the approximation of the signal and consequently of the sidebands in the frequency domain is improved. In contrast to the traditional VAM approach, the measurements at individual stress levels can be extracted from any given vibration or even static loads. This flexibility enables the applicability of the synthetic VAM even in unfavourable conditions, where the dynamic VAM approach is not feasible or would result in imprecise results.

The synthetic process also allows for evaluating the differences in the amplitude or the phase of the signal due to the changes in stress, as these parameters were computed anyway. First indications suggest that evaluating these parameters individually has improved the damage detection at the tested coupon specimens compared to the dynamic VAM or its synthetic recreation. In the experiment, only the average amplitude and average phase over the measured frequency range of two stress levels were compared. A thorough evaluation, by including several stress levels could further increase the precision and information gain.

While this synthetic method was introduced by testing simple coupon specimens under ideal laboratory conditions, it was verified on larger and more complex structures made from fibre-reinforced polymers. It was demonstrated, that the approximations of traditional dynamic VAM were not as precise at these bigger structures. Here, the synthetic MI appeared to be even more sensitive to the impact damage in a subsection of a wind turbine blade, as it was following the anticipated increase with each subsequent impact damage.

The synthetic VAM was further evaluated on a thick-walled cuboid, that was tested under simultaneous compression and torsion loading on a hexapodal testing machine. However, inconsistent stress amplitudes during the fatigue experiment affected the dynamic VAM, made the evaluation of the MI imprecise and introduced artefacts. The occurring damages reduced the stress amplitude of the testing machine and altered the modulation of the signal. By applying the synthetic VAM and choosing a constant stress amplitude throughout all measurements, the increase in damage could be detected more precisely. Severe fibre-buckling resulted in an increased MI and also the adapted testing parameters during the fatigue experiment did not affect the measurements strongly. Consequently, the results underline the benefits of the synthetic over the dynamic VAM method for applicability with changing vibrations. Furthermore, it was shown, that the data reduction by applying the synthetic VAM was possible even at these large structures, as the signals were generated from only 10 points, acquired at $f_\mathrm{s} = 10\,\mathrm{kSa/s}$ (2.3% of signals Nyquist rate) from two stress levels.

Since a reliable application of VAM for industrial structures has not yet been achieved, the first step following the results of this thesis should be the integration of VAM into already existing SHM solutions. This integration allows to compare the results, evaluate the true sensitivity and complement the traditional applied testing methods. The structural health is typically evaluated by dedicated piezoceramic sensors, that measure the acoustic emissions of damages in the structure. Initial experiments on coupon specimens have already indicated (*cf. Chapter A.8*), that all VAM sensors used in this thesis could be replaced with typical acoustic emissions sensors, with negligible impact on the measured VAM response. Consequently, only the signal generation needs to be installed, and the post-processing of the acoustic emissions measurements must be adapted to incorporate VAM into existing SHM systems.

Alternatively, implementing a dedicated sensor network with low-powered microcontrollers would enhance the research by providing crucial experiences outside the lab. By incorporating the synthetic VAM in the signal acquisition, the reduced sampling rate could even enable the use of energy-harvesting sensor nodes without external power sources [12]. For the excitation of the carrier signal, it was indicated that subsequently sent burst signals are sufficient as carrier vibration to evaluate the structure as well. The results of this thesis indicate that the synthetic VAM can be applied to these signals as well, to assess the structure at the defined stress levels. However, this assumption must be validated on larger structures, as it has only been shown on coupon specimens so far.

Finally, the individual evaluation of the variations in amplitude and phase, due to changes in structure's stress is promising and shows a potential to increase the precision of VAM for damage detection. Consequently, further research is needed to assess and improve this evaluation. It is assumed, that this evaluation is the basis of VAM, and would offer more information, which will increase the understanding of VAM.

It can be concluded that combined measurements at several stress states contain information similar to those obtained from dynamic VAM measurements. Since the traditional dynamic VAM approach faces challenges like deviations in the pump vibration over time, the synthetic approach emerges as a valuable enhancement. This new approach enables robust structural health monitoring in changing environmental conditions and variable loading scenarios. Further evaluations are required to determine detectable damage types. Is the synthetic VAM, or VAM in general, capable of detecting damages in larger structures, if they are not located in the signal path, as indicated in the experiments with the wind turbine blade? Consequently, the effect of the stiffening elements, like the shear webs or even stringers, on the modulated signal has to be evaluated further. Simulations of the wave propagation could improve the optimal sensor placement in these cases but it has to be validated. Only if these aspects are better understood, the vibro-acoustic modulation will be valuable for the industries.

Bibliography

[1] Charles R. Farrar and Keith Worden. “An introduction to structural health monitoring”. In: *Philos. Trans. R. Soc. A Math. Phys. Eng. Sci.* 365.1851 (2007), pp. 303–315. DOI: `10.1098/rsta.2006.1928`.

[2] Christian Boller. *Encyclopedia of Structural Health Monitoring.* 2009. DOI: `10.1002/9780470061626`.

[3] Charles R. Farrar and Keith Worden. *Structural Health Monitoring: A Machine Learning Perspective.* 2012. DOI: `10.1002/9781118443118`.

[4] Fu-Kuo Chang. “Structural Health Monitoring: A Summary Report on the First Stanford Workshop on Structural Health Monitoring, September 18-20, 1997”. In: 298 (1998).

[5] Daniel Balageas, Claus-Peter Fritzen, and Alfredo Güemes. *Structural Health Monitoring.* ISTE Ltd, 2006. ISBN: 1-905209-01-0.

[6] Anna-Kathrin Wallasch, Silke Lüers, and Knud Rehfeldt. *Kostensituation der Windenergie an Land in Deutschland.* Tech. rep. Deutsche WindGuard GmbH, 2015, pp. 1–54.

[7] Dino Clark. *GCUBE TOP 5 US WIND ENERGY INSURANCE CLAIMS REPORT.* 2013. URL: `http://www.gcube-insurance.com/news/gcube-top-5-us-wind-energy-insurance-claims-report/` (visited on 11/01/2023).

[8] The Boeing Company. *Commercial Market Outlook 2022-2041.* URL: `https://www.boeing.com/commercial/market/commercial-market-outlook/index.page` (visited on 11/01/2023).

[9] Benjamin Boll, Erik Willmann, Bodo Fiedler, and Robert Horst Meißner. “Weak adhesion detection – Enhancing the analysis of vibroacoustic modulation by machine learning”. In: *Compos. Struct.* 273 (2021). DOI: `10.1016/j.compstruct.2021.114233`.

[10] Benjamin Boll, Erik Willmann, Bodo Fiedler, and Robert Horst Meissner. “Weak bond detection in single-lap shear bonds by evaluating vibroacoustic modulations with artificial neural networks”. In: *Proc. 20th Eur. Conf. Compos. Mater. - Compos. Meet Sustain. (Vol 3)*. Vol. 3. EPFL Lausanne, Composite Construction Laboratory, 2022, pp. 509–516. DOI: `10.5075/epfl-298799_978-2-9701614-0-0`.

[11] Benjamin Boll, Lennart Dorendorf, Peter Oppermann, Erik Willmann, Bodo Fiedler, Bernd-Christian Renner, Marcus Rutner, and Robert Horst Meißner. “Synthetic generation of vibroacoustic modulation signals for structural health monitoring”. In: *Mech. Syst. Signal Process.* 200.5 (Nov. 2023), p. 110498. DOI: `10.1016/j.ymssp.2023.110498`.

[12] Peter Oppermann, Lennart Dorendorf, Benjamin Boll, Abedin Gagani, Nikolay Lalkovski, Christian Renner, Marcus Rutner, Obert Meißner, and Bodo Fiedler. “Towards Structural Health Monitoring using Vibro-Acoustic Modulation in the Real World”. In: *Proc. 18th GI/ITG KuVS Fachgespräch "Sensornetze"*. FGSN (2019).

[13] Erik Willmann, Benjamin Boll, Moritz Scheel, Robert H. Meißner, Bodo Fiedler, Robert Horst, and Bodo Fiedler. “Health monitoring of CFRP laminates under cyclic loading via vibro-acoustic modulation based measurements”. In: *Compos. Struct.* 308.June 2022 (2022), p. 116696. DOI: `10.1016/j.compstruct.2023.116696`.

[14] Erik Willmann, Benjamin Boll, Gor Mikaelyan, Hans Wittich, Robert Horst Meißner, and Bodo Fiedler. “Vibro-acoustic modulation based measurements in CFRP laminates for damage detection in Open-Hole structures”. In: *Compos. Commun.* 42 (2023). DOI: `10.1016/j.coco.2023.101659`.

[15] Erik Willmann, Benjamin Boll, Heinrich Pfeifer, Robert Horst Meissner, and Bodo Fiedler. “Determination of remaining useful life in CFRP for predictive maintenance by the VAM method”. In: *Prepr. Submitt. to Compos. Part A* (2024).

[16] Erik Willmann, Benjamin Boll, Moritz Scheel, Torben Dräger, Robert Meißner, and Bodo Fiedler. “Vibro-acoustic modulation measurements for a lifetime evaluation of composite materials”. In: *23rd International Conference on Composites Materials, ICCM 2023*. International Committee on Composite Materials. 2023.

[17] Lennart Dorendorf, Nikolay Lalkovski, Benjamin Boll, Robert Horst, and Marcus Rutner. "Separation and quantification of damage-induced and non-damage-induced vibro-acoustic modulation and the hazard of contrary modulations in structural health monitoring applications". In: *Submitt. to Mech. Syst. Signal Process.* (2024).

[18] Berit Zeller-Plumhoff, Melissa Gile, Melissa Priebe, Hanna Slominska, Benjamin Boll, Björn Wiese, Tim Würger, Regine Willumeit-Römer, and Robert Horst Meißner. "Exploring key ionic interactions for magnesium degradation in simulated body fluid – A data-driven approach". In: *Corros. Sci.* 182.November 2020 (2021). DOI: `10.1016/j.corsci.2021.109272`.

[19] Robert H. Meißner, Julian Konrad, Benjamin Boll, Bodo Fiedler, and Dirk Zahn. "Molecular simulation of thermosetting polymer hardening: Reactive events enabled by controlled topology transfer". In: *Macromolecules* 53.22 (2020), pp. 9698–9705. DOI: `10.1021/acs.macromol.0c02222`.

[20] Helmut Schürmann. *Konstruieren mit Faser-Kunststoff-Verbunden.* Vol. 1. 4. Springer, 2007, p. 53. DOI: `10.1007/978-3-540-72190-1`.

[21] M. Brod, A. Dean, S. Scheffler, C. Gerendt, and R. Rolfes. "Numerical modeling and experimental validation of fatigue damage in Cross-Ply CFRP composites under inhomogeneous stress states". In: *Compos. Part B Eng.* 200 (2020). DOI: `10.1016/j.compositesb.2020.108050`.

[22] Wayne W. Stinchcomb and Charles E. Bakis. "Fatigue Behavior of Composite Laminates". In: *Compos. Mater. Ser.* Vol. 4. C. 1991, pp. 105–180. DOI: `10.1016/B978-0-444-70507-5.50008-1`.

[23] Johann Körbelin, Benedikt Kötter, Hauke Voormann, Lukas Brandenburg, Stefan Selz, and Bodo Fiedler. "Damage tolerance of few-layer graphene modified CFRP: From thin-to thick-ply laminates". In: *Composites Science and Technology* 209 (Mar. 2021), p. 108765. DOI: `10.1016/j.compscitech.2021.108765`.

[24] Dennis Gibhardt, Christina Buggisch, Devin Meyer, and Bodo Fiedler. "Hygrothermal Aging History of Amine-Epoxy Resins: Effects on Thermo-Mechanical Properties". In: *Frontiers in Materials* (Mar. 2022), p. 826076. DOI: `10.3389/fmats.2022.826076`.

[25] Jonas Drummer, Dennis Gibhardt, Johann Körbelin, and Bodo Fiedler. “General influence of the environmental temperature on the matrix strength under tensile and compressive loading - A comprehensive study on high performance matrices”. In: *Composites Science and Technology* 230 (May 2022), p. 109486. DOI: `10.1016/j.compscitech.2022.109486`.

[26] Alexander Müller. “Schädigungscharakterisierung an Faser-Kunststoff-Verbunden im Schwingversuch mittels Röntgenrefraktionstopographie unter Berücksichtigung der Matrixeigenschaften”. In: September 2018 (2019), p. 189.

[27] Wieslaw J. Staszewski. “Structural Health Monitoring Using Guided Ultrasonic Waves”. In: *Naika.* 14 (2004), pp. 804–810. DOI: `10.1007/978-3-662-05615-8_6`.

[28] Liang Zeng, Liping Huang, Xuwei Cao, and Fei Gao. “Determination of Lamb wave phase velocity dispersion using time-frequency analysis”. In: *Smart Mater. Struct.* 28.11 (2019). DOI: `10.1088/1361-665X/ab47e1`.

[29] Gabriel M.F. Ramalho, António M. Lopes, and Lucas F.M. da Silva. “Structural health monitoring of adhesive joints using Lamb waves: A review”. In: *Struct. Control Heal. Monit.* 29.1 (2022), pp. 1–22. DOI: `10.1002/stc.2849`.

[30] Rolf Lammering, Ulrich Gabbert, Michael Sinapius, Thomas Schuster, and Peter Wierach. *Lamb-Wave Based Structural Health Monitoring.* Springer International Publishing, 2017. DOI: `10.1002/0470869097.ch11`.

[31] Pranav Karve, Sarah Miele, Kyle Neal, Sankaran Mahadevan, Vivek Agarwal, Eric R Giannini, and Patricia Kyslinger. “Vibro-acoustic modulation and data fusion for localizing alkali–silica reaction–induced damage in concrete”. In: *Struct. Heal. Monit.* 19.6 (2020), pp. 1905–1923. DOI: `10.1177/1475921720905509`.

[32] Alfredo Güemes. “SHM Technologies and Applications in Aircraft Structure”. In: *5th Int. Symp. NDT Aerosp.* 26.1 (2013), pp. 77–78.

[33] Anders Rytter. “Vibrational Based Inspection of Civil Engineering Structures”. PhD thesis. Denmark, 1993.

[34] Victor Giurgiutiu. *Structural Health Monitoring.* Elsevier, 2008, pp. 1–747. DOI: `10.1016/B978-0-12-088760-6.X5001-6`.

[35] Yongping Zheng, Roman Gr Maev, and Igor Yu Solodov. “Review / Synthèse non-linear acoustic applications for material characterization : A review”. In: 967.519 (1999), pp. 927–967.

[36] Christian Boller and G R Tomlinson. *Health Monitoring of Aerospace Structures*. 2003. DOI: `10.1002/0470092866`.

[37] Kajetan Dziedziech, Lukasz Pieczonka, Piotr Kijanka, and Wieslaw J Staszewski. “Enhanced non-linear crack-wave interactions for structural damage detection based on guided ultrasonic waves”. In: *Struct. Control Heal. Monit.* 23.8 (Aug. 2016), pp. 1108–1120. DOI: `10.1002/stc.1828`. arXiv: `1011.1669`.

[38] Tribikram Kundu, ed. *Ultrasonic Nondestructive Evaluation*. CRC Press, Dec. 2003. DOI: `10.1201/9780203501962`.

[39] Lukasz Pieczonka, Andrzej Klepka, Adam Martowicz, and Wieslaw Staszewski. “non-linear vibroacoustic wave modulations for structural damage detection: an overview”. In: *Opt. Eng.* 55.1 (2015), p. 011005. DOI: `10.1117/1.oe.55.1.011005`.

[40] Peter B. Nagy. “Fatigue damage assessment by non-linear ultrasonic materials characterization”. In: *Ultrasonics* 36.1 (1998). Ultrasonics International 1997, pp. 375–381.

[41] K. E.-A. Van Den Abeele, Paul A. Johnson, and A. Sutin. “non-linear Elastic Wave Spectroscopy (NEWS) Techniques to Discern Material Damage, Part I: non-linear Wave Modulation Spectroscopy (NWMS)”. In: *Res. Nondestruct. Eval.* 12.1 (2000), pp. 17–30. DOI: `10.1080/09349840009409646`.

[42] V. Yu Zaitsev, A. M. Sutin, I. Yu Belyaeva, and V. E. Nazarov. “non-linear Interaction of Acoustical Waves Due to Cracks and Its Possible Usage for Cracks Detection”. In: *J. Vib. Control* 1.3 (1995), pp. 335–344. DOI: `10.1177/107754639500100305`.

[43] Dimitri Donskoy, Keith Ferroni, Alexander Sutin, and Keith Sheppard. “A non-linear Acoustic Technique for Crack and Corrosion Detection in Reinforced Concrete”. In: *Nondestruct. Charact. Mater. VIII*. Boston, MA: Springer US, 1998, pp. 555–560. DOI: `10.1007/978-1-4615-4847-8_87`.

[44] Dimitri Donskoy, Alexander Ekimov, and Alexander Sutin. “Characterization of bonding quality of composites with the non-linear modulation method”. In: *J. Acoust. Soc. Am.* 105.2 (Feb. 1999), pp. 954–954. DOI: `10.1121/1.425761`.

[45] Alexander Sutin and Dimitri Donskoy. “non-linear Vibro-Acoustic Nondestructive Testing Technique”. In: *Nondestruct. Charact. Mater. VIII.* 1998, pp. 133–138. DOI: `10.1007/978-1-4615-4847-8_21`.

[46] Dmitri M. Donskoy and Alexander M. Sutin. “Vibro-acoustic modulation non-destructive evaluation technique”. In: *J. Intell. Mater. Syst. Struct.* 3397.September 1998 (1998), pp. 765–771.

[47] E. M. Ballad, S. Yu Vezirov, K. Pfleiderer, I. Yu Solodov, and G. Busse. “non-linear modulation technique for NDE with air-coupled ultrasound”. In: *Ultrasonics* 42.1-9 (2004), pp. 1031–1036. DOI: `10.1016/j.ultras.2003.12.022`.

[48] Rafael Muñoz *et al.* “Emerging design solutions in structural health monitoring systems”. In: *Emerg. Des. Solut. Struct. Heal. Monit. Syst.* i (2015), pp. 1–337. DOI: `10.4018/978-1-4666-8490-4`.

[49] Francesco Aymerich and Wieslaw Staszewski. “Experimental study of impact-damage detection in composite laminates using a cross-modulation vibro-acoustic technique”. In: *Struct. Heal. Monit.* 9.6 (2010), pp. 541–553. DOI: `10.1177/1475921710365433`.

[50] A. Carcione, P. Blanloeuil, and M. Veidt. “Demodulation technique to identify non-linear characteristics of vibro-acoustic NDT measurements”. In: *J. Sound Vib.* 466 (2020), p. 115014. DOI: `10.1016/j.jsv.2019.115014`.

[51] Tingyuan Yin, Ching Tai Ng, and Andrei Kotousov. “Damage detection of ultra-high-performance fibre-reinforced concrete using a harmonic wave modulation technique”. In: *Constr. Build. Mater.* 313.November (2021), p. 125306. DOI: `10.1016/j.conbuildmat.2021.125306`.

[52] Andrzej Klepka, Lukasz Pieczonka, Kajetan Dziedziech, Wieslaw Staszewski, Francesco Aymerich, and Tadeusz Uhl. “Structural Damage Detection Based on non-linear Acoustics: Application Examples”. In: *non-linear Ultrason. Vibro-Acoustical Tech. Nondestruct. Eval.* 2019. Chap. 4: Structu, pp. 139–174. DOI: `10.1007/978-3-319-94476-0_4`.

[53] Dmitri M. Donskoy and Alexander M. Sutin. “Vibro-acoustic modulation non-destructive evaluation technique”. In: *J. Intell. Mater. Syst. Struct.* 3397.September 1998 (1998), pp. 765–771.

[54] Dimitri Donskoy. “Encyclopedia of Structural Health Monitoring- Chapter15 - non-linear Acoustic Methods”. In: *Encycl. Struct. Heal. Monit.* 2009. Chap. 15 - Nonli. ISBN: 978-0-470-05822-0.

[55] Dimitri Donskoy, A. Sutin, and A. Ekimov. “non-linear acoustic interaction on contact interfaces and its use for non-destructive testing”. In: *NDT E Int.* 34.4 (2001), pp. 231–238. DOI: `10.1016/S0963-8695(00)00063-3`.

[56] Nathanael C. Yoder and Douglas E. Adams. “Vibro-acoustic modulation utilizing a swept probing signal for robust crack detection”. In: *Struct. Heal. Monit.* 9.3 (2010), pp. 257–267. DOI: `10.1177/1475921710365261`.

[57] Kajetan Dziedziech, Lukasz Pieczonka, Maciej Adamczyk, Andrzej Klepka, and Wieslaw J. Staszewski. “Efficient swept sine chirp excitation in the non-linear vibro-acoustic wave modulation technique used for damage detection”. In: *Struct. Heal. Monit.* 17.3 (2018), pp. 565–576. DOI: `10.1177/1475921717704638`.

[58] Nan Zhao, LinSheng Huo, and Gangbing Song. “Vibration acoustic modulation for bolt looseness monitoring based on frequency-swept excitation and bispectrum”. In: *Smart Mater. Struct.* (2023). DOI: `10.1088/1361-665x/acb579`.

[59] Dong Liu and Dimitri Donskoy. “Frequency Modulation in Vibro-Acoustic Modulation Method”. In: *Int. J. Civ. Environ. Eng.* 17.1 (2023), pp. 42–47.

[60] V.Yu. Zaitsev, V. Gusev, and B. Castagnède. “Observation of the “Luxemburg–Gorky effect” for elastic waves”. In: *Ultrasonics* 40.7 (2002), pp. 627–631. DOI: `10.1103/PhysRevLett.26.410`.

[61] Vladimir Zaitsev, Veniamin Nazarov, Vitaly Gusev, and Bernard Castagnede. “Novel non-linear-modulation acoustic technique for crack detection”. In: *NDT E Int.* 39.3 (2006), pp. 184–194. DOI: `10.1016/j.ndteint.2005.07.007`.

[62] A. Klepka, M. Adamczyk, L. Pieczonka, and W. J. Staszewski. “Wideband excitation in non-linear vibro-acoustic modulation for damage detection”. In: *Heal. Monit. Struct. Biol. Syst. 2016* 9805.April 2016 (2016), p. 980513. DOI: `10.1117/12.2218805`.

[63] Peipei Liu, Hoon Sohn, and Ikgeun Jeon. "non-linear spectral correlation for fatigue crack detection under noisy environments". In: *J. Sound Vib.* 400 (2017), pp. 305–316. DOI: `10.1016/j.jsv.2017.04.021`.

[64] Dimitri Donskoy, A.E. Ekimov, and A.M. Sutin. "Detection and characterization of defects with vibro-acoustic modulation technique". In: *Emerg. Technol. NDT*. 1999, pp. 153–158. DOI: `10.1201/9781003078586-27`.

[65] Dimitri Donskoy, Alexander Ekimov, Emile Luzzato, Jean-Louis Lottiaux, Stanislav Stoupin, and Andrei Zagrai. "N-SCAN: new vibromodulation system for detection and monitoring of cracks and other contact-type defects". In: *Smart Struct. Mater. 2003 Smart Syst. Nondestruct. Eval. Civ. Infrastructures.* Vol. 5057. August 2003. 2003, p. 400. DOI: `10.1117/12.484635`.

[66] Philippe Duffour, Marco Morbidini, and Peter Cawley. "A study of the vibro-acoustic modulation technique for the detection of cracks in metals". In: *J. Acoust. Soc. Am.* 119.3 (2006), pp. 1463–1475. DOI: `10.1121/1.2161429`.

[67] P. Duffour, M. Morbidini, and P. Cawley. "Comparison between a type of vibro-acoustic modulation and damping measurement as NDT techniques". In: *NDT E Int.* 39.2 (2006), pp. 123–131. DOI: `10.1016/j.ndteint.2005.07.010`.

[68] X. J. Chen, J. Y. Kim, K. E. Kurtis, J. Qu, C. W. Shen, and L. J. Jacobs. "Characterization of progressive microcracking in Portland cement mortar using non-linear ultrasonics". In: *NDT E Int.* 41.2 (2008), pp. 112–118. DOI: `10.1016/j.ndteint.2007.08.009`.

[69] Andrei Zagrai, Dimitri Donskoy, Alexander Chudnovsky, Edward Golovin, and Vinod S. Agarwala. "Micro/meso scale fatigue damage accumulation monitoring using non-linear acoustic vibro-modulation measurements". In: *Testing, Reliab. Appl. Micro- Nano-Material Syst. IV.* Ed. by Robert E. Geer, Norbert Meyendorf, George Y. Baaklini, and Dietmar W. Vogel. Vol. 6175. April 2006. Mar. 2006, p. 617506. DOI: `10.1117/12.658558`.

[70] Lennart Dorendorf, Nikolay Lalkovski, Ricarda Stolz, and Marcus Rutner. "Zuverlässigkeit der Vibro-Akustischen Modulationsmethode zur Strukturüberwachung von Metallen unter Ermüdungsbeanspruchung und ihr

Potenzial für das Bauwesen”. In: *22. DASt-Forschungskolloquium.* Karlsruhe, Deutschland, 2020, pp. 135–139.

[71] Lennart Dorendorf, Nikolay Lalkovski, and Marcus Rutner. “Physical explanation for vibro-acoustic modulation due to local and global nonlinearities in a structure and its experimental and numerical validation”. In: *J. Sound Vib.* (2022), p. 116885. DOI: `https://doi.org/10.1016/j.jsv.2022.116885`.

[72] Abdullah Alnutayfat, Alexander Sutin, and Dong Liu. “Vibroacoustic Modulation of Wideband Vibrations and Its Possible Application for Windmill Blade Diagnostics”. In: *Int. J. Civ. Environ. Eng.* 17.1 (2023), pp. 31–36.

[73] V.Yu Zaitsev and P. Sas. “non-linear response of a weakly damaged metal samle: A Dissipative Modulation Mechanism of Vibro-Acoustic Interaction”. In: *J. Vib. Control* 6 (2000), pp. 803–822.

[74] Andrei Zagrai, Dimitri Donskoy, Alexander Chudnovsky, and Edward Golovin. “Micro-and macroscale damage detection using the non-linear acoustic vibro-modulation technique”. In: *Res. Nondestruct. Eval.* 19.2 (2008), pp. 104–128. DOI: `10.1080/09349840801931817`.

[75] Jingpin Jiao, Lei Zheng, Guorong Song, Cunfu He, and Bin Wu. “Vibro-acoustic modulation technique for micro-crack detection in pipeline”. In: *Seventh Int. Symp. Precis. Eng. Meas. Instrum.* Ed. by Kuang-Chao Fan, Man Song, and Rong-Sheng Lu. Vol. 8321. SPIE, Aug. 2011, pp. 1013–1020. DOI: `10.1117/12.905550`.

[76] Ted Ooijevaar, Matthew D. Rogge, Richard Loendersloot, Laurent Warnet, Remko Akkerman, and Tiedo Tinga. “Vibro-acoustic modulation–based damage identification in a composite skin–stiffener structure”. In: *Struct. Heal. Monit.* 15.4 (2016), pp. 458–472. DOI: `10.1177/1475921716645107`.

[77] Furui Wang and Gangbing Song. “Bolt early looseness monitoring using modified vibro-acoustic modulation by time-reversal”. In: *Mech. Syst. Signal Process.* 130 (2019), pp. 349–360. DOI: `10.1016/j.ymssp.2019.04.036`.

[78] Andrzej Klepka, Kajetan Dziedziech, Jakub Mrówka, and Jakub Górski. “Experimental investigation of modulation effects for contact-type interfaces in vibro-acoustic modulation tests”. In: *Struct. Heal. Monit.* 20.3 (2021), pp. 917–930. DOI: `10.1177/1475921719857624`.

[79] Gabriela Loi, Francesco Aymerich, and Maria Cristina Porcu. “Influence of Sensor Position and Low-Frequency Modal Shape on the Sensitivity of Vibro-Acoustic Modulation for Impact Damage Detection in Composite Materials”. In: *J. Compos. Sci.* 6.7 (2022). DOI: `10.3390/jcs6070190`.

[80] Tingyuan Yin, Ching Tai Ng, James Vidler, Van Dac Ho, and Andrei Kotousov. “Amplitude-Modulation Vibro-Acoustic Technique for Damage Evaluation”. In: *Struct. Heal. Monit.* 0.0 (2022), pp. 1–22. DOI: `10.1177/14759217221106209`.

[81] Hoon Sohn, Hyung Jin Lim, Martin P. Desimio, Kevin Brown, and Mark Derriso. “non-linear ultrasonic wave modulation for online fatigue crack detection”. In: *J. Sound Vib.* 333.5 (2014), pp. 1473–1484. DOI: `10.1016/j.jsv.2013.10.032`.

[82] Lukasz Pieczonka, L. Zietek, Andrzej Klepka, Wieslaw J. Staszewski, Francesco Aymerich, and Tadeusz Uhl. “Damage imaging in composites using non-linear vibro-acoustic wave modulations”. In: *Struct. Control Heal. Monit.* 25.2 (2018), pp. 1–13. DOI: `10.1002/stc.2063`.

[83] M. Miró, J. N. Eiras, P. Poveda, M. Climent, and J. Ramis. “Detecting cracks due to steel corrosion in reinforced cement mortar using intermodulation generation of ultrasonic waves”. In: *Constr. Build. Mater.* 286 (2021), p. 122915. DOI: `10.1016/j.conbuildmat.2021.122915`.

[84] H. F. Hu, G. J. Shen, D. X. Yang, S. F. Zhang, Y. M. Yang, and F. J. Guan. “Crack localization in plate-like metallic structures using vibration modulated guided waves”. In: *J. Phys. Conf. Ser.* 2184.1 (2022). DOI: `10.1088/1742-6596/2184/1/012032`.

[85] Michele Meo, Umberto Polimeno, and Giuseppe Zumpano. “Detecting damage in composite material using non-linear elastic wave spectroscopy methods”. In: *Appl. Compos. Mater.* 15.3 (2008), pp. 115–126. DOI: `10.1007/s10443-008-9061-7`.

[86] Francesco Ciampa, Dimitrios Dionysopoulos, Gian Piero Malfense Fierro, and Michele Meo. "Damage detection in composites using non-linear ultrasonically modulated thermography". In: March 2018 (2018), p. 20. DOI: `10.1117/12.2303404`.

[87] Sungmin Kim *et al.* "Crack detection technique for operating wind turbine blades using Vibro-Acoustic Modulation". In: *Struct. Heal. Monit.* 13.6 (2014), pp. 660–670. DOI: `10.1177/1475921714553732`.

[88] Wieslaw Staszewski, Christian Boller, S. Grondel, C. Biemans, E. O'Brien, C. Delebarre, and G. R. Tomlinson. *Damage Detection Using Stress and Ultrasonic Waves.* 2004, pp. 125–162. DOI: `10.1002/0470092866.ch4`.

[89] I. Solodov, J. Wackerl, K. Pfleiderer, and G. Busse. "non-linear self-modulation and subharmonic acoustic spectroscopy for damage detection and location". In: *Appl. Phys. Lett.* 84.26 (2004), pp. 5386–5388. DOI: `10.1063/1.1767283`.

[90] Andrzej Klepka, Wieslaw Staszewski, R. B. Jenal, M. Szwedo, Joanna Iwaniec, and Tadeusz Uhl. "non-linear acoustics for fatigue crack detection - experimental investigations of vibro-acoustic wave modulations". In: *Struct. Heal. Monit.* 11.2 (2012), pp. 197–211. DOI: `10.1177/1475921711414236`.

[91] H. F. Hu, Wieslaw J. Staszewski, N. Q. Hu, R. B. Jenal, and G. J. Qin. "Crack detection using non-linear acoustics and piezoceramic transducers-instantaneous amplitude and frequency analysis". In: *Smart Mater. Struct.* 19.6 (2010). DOI: `10.1088/0964-1726/19/6/065017`.

[92] Edouard Oyallon and Stéphane Mallat. "Deep roto-translation scattering for object classification". In: *Proc. IEEE Comput. Soc. Conf. Comput. Vis. Pattern Recognit.* 07-12-June (2015), pp. 2865–2873. DOI: `10.1109/CVPR.2015.7298904`. arXiv: `1412.8659`.

[93] Zheng Huifeng, Hu Liuchen, Fang Piaopiao, Wang Yuebing, and Cao Yonggang. "The study of micro-crack localisation based on vibro-acoustic modulation and time reversal method". In: *Nondestruct. Test. Eval.* 34.3 (2019), pp. 324–338. DOI: `10.1080/10589759.2019.1600687`.

[94] Ning Li, Furui Wang, and Gangbing Song. “New entropy-based vibro-acoustic modulation method for metal fatigue crack detection: An exploratory study”. In: *Meas. J. Int. Meas. Confed.* 150 (2020), p. 107075. DOI: `10.1016/j.measurement.2019.107075`.

[95] Sang Eon Lee and Jung Wuk Hong. “Detection of micro-cracks in metals using modulation of PZT-induced lamb waves”. In: *Materials (Basel).* 13.17 (2020). DOI: `10.3390/ma13173823`.

[96] K. Dziedziech, A. Klepka, J. Roemer, and L. Pieczonka. “Experimental study of thermo-acoustic wave modulation in a cracked plate”. In: *J. Sound Vib.* 498 (2021), p. 115970. DOI: `10.1016/j.jsv.2021.115970`.

[97] Peter Oppermann, Lennart Dorendorf, Marcus Rutner, and Christian Renner. “non-linear modulation with low-power sensor networks using undersampling”. In: *Struct. Heal. Monit.* January (2021). DOI: `10.1177/1475921720982885`.

[98] Francesco Aymerich and Wieslaw Staszewski. “Impact damage detection in composite laminates using non-linear acoustics”. In: *Compos. Part A Appl. Sci. Manuf.* 41.9 (2010), pp. 1084–1092. DOI: `10.1016/j.compositesa.2009.09.004`.

[99] A. Klepkal, Francesco Aymerich, Wieslaw Staszewski, and Tadeusz Uhl. “non-linear vibro-acoustic wave modulations for impact damage detection in composites”. In: *ECCM 2012 - Compos. Venice, Proc. 15th Eur. Conf. Compos. Mater.* June. 2012, pp. 24–28. ISBN: 9788888785332.

[100] L Pieczonka, P Ukowski, Andrzej Klepka, WJ Staszewski, T Uhl, and Francesco Aymerich. “Impact damage detection in light composite sandwich panels using piezo-based non-linear vibro-acoustic modulations”. In: *Smart Materials and Structures* 23.10 (2014), p. 105021.

[101] Phong B Dao, Łukasz Pieczonka, Maciej Petko, and Wieslaw J Staszewski. “Damage Detection in Composite Sandwich Panels Using non-linear Acoustics and Cointegration-Based Signal Processing”. In: *Int.Symp SHM NDT Saarbrücken* October (2018).

[102] Andrzej Klepka, Lukasz Pieczonka, W. J. Staszewski, and Francesco Aymerich. “Impact damage detection in laminated composites by non-linear vibro-acoustic wave modulations”. In: *Compos. Part B Eng.* 65 (2014), pp. 99–108. DOI: `10.1016/j.compositesb.2013.11.003`.

[103] Gabriela Loi, G Marongiu, Maria Cristina Porcu, and Francesco Aymerich. "Vibro-Acoustic Modulation with broadband pump excitation for efficient impact damage detection in composite materials". In: *IOP Conf. Ser. Mater. Sci. Eng.* IOP Publishing, 2023, p. 1275. DOI: `10.1088/1757-899X/1275/1/012008`.

[104] M. Dunn, A. Carcione, P. Blanloeuil, and M. Veidt. "Critical Aspects of Experimental Damage Detection Methodologies Using non-linear Vibro-ultrasonics". In: *6th Asia Pacific Work. Struct. Heal. Monit. 6th APW-SHM.* Vol. 188. The Author(s), 2017, pp. 133–140. DOI: `10.1016/j.proeng.2017.04.466`.

[105] Shervin Tashakori, Amin Baghalian, Volkan Y. Senyurek, Muhammet Unal, Dwayne McDaniel, and Ibrahim N. Tansel. "Implementation of heterodyning effect for monitoring the health of adhesively bonded and fastened composite joints". In: *Appl. Ocean Res.* 72 (2018), pp. 51–59. DOI: `10.1016/j.apor.2018.01.008`.

[106] Ashish Kumar Singh, Vincent B.C. Tan, Tong Earn Tay, and Heow Pueh Lee. "Experimental Investigations into non-linear Vibro-Acoustics for Detection of Delaminations in a Composite Laminate". In: *J. Nondestruct. Eval. Diagnostics Progn. Eng. Syst.* 2.1 (2019), pp. 1–11. DOI: `10.1115/1.4041122`.

[107] Ashish Kumar Singh. "DETECTION OF DEFECTS IN COMPOSITE LAMINATES WITH VIBRO-ULTRASONIC METHODS". PhD thesis. NATIONAL UNIVERSITY OF SINGAPORE, 2019. DOI: `10.13140/RG.2.2.25647.38560`.

[108] Yi He, Yi Xiao, Zhongqing Su, Yongdong Pan, and Zhen Zhang. "Contact acoustic non-linearity effect on the vibro-acoustic modulation of delaminated composite structures". In: *Mech. Syst. Signal Process.* 163.July 2021 (2022). DOI: `10.1016/j.ymssp.2021.108161`.

[109] Lunan Wei and Jun Chen. "Determination of optimal probing frequency for enhancing non-linear vibro-acoustic modulation behaviors of delaminated CFRP based on local defect resonance". In: *Mech. Syst. Signal Process.* 187 (2023), p. 109961. DOI: `https://doi.org/10.1016/j.ymssp.2022.109961`.

[110] Zhen Zhang, Menglong Liu, Zhongqing Su, and Yi Xiao. "Quantitative evaluation of residual torque of a loose bolt based on wave energy dissipation and vibro-acoustic modulation: A comparative study". In: *J. Sound Vib.* 383 (2016), pp. 156–170. DOI: `10.1016/j.jsv.2016.07.001`.

[111] Zhen Zhang, Hao Xu, Yaozhong Liao, Zhongqing Su, and Yi Xiao. "Vibro-acoustic modulation (VAM)-inspired structural integrity monitoring and its applications to bolted composite joints". In: *Compos. Struct.* 176 (2017), pp. 505–515. DOI: `10.1016/j.compstruct.2017.05.043`.

[112] Carter L. Neblett, Manton J. Guers, and Dean E. Capone. "Evaluation of bolt torque levels using non-linear wave modulation spectroscopy". In: *AIP Conf. Proc.* 2102.May (2019). DOI: `10.1063/1.5099736`.

[113] Janette J. Meyer and Douglas E. Adams. "Using impact modulation to quantify non-linearities associated with bolt loosening with applications to satellite structures". In: *Mech. Syst. Signal Process.* 116 (2019), pp. 787–795. DOI: `10.1016/j.ymssp.2018.06.042`.

[114] Xiaoshu Qin, Chang Peng, Gaozheng Zhao, Zengye Ju, Shanshan Lv, Mingshun Jiang, Qingmei Sui, and Lei Jia. "Full life-cycle monitoring and earlier warning for bolt joint loosening using modified vibro-acoustic modulation". In: *Mech. Syst. Signal Process.* 162 (2022), p. 108054. DOI: `https://doi.org/10.1016/j.ymssp.2021.108054`.

[115] Xiao Xue Li, Dan Li, Wei Xin Ren, and Jun Shu Zhang. "Loosening Identification of Multi-Bolt Connections Based on Wavelet Transform and ResNet-50 Convolutional Neural Network". In: *Sensors* 22.18 (2022), p. 6825. DOI: `10.3390/s22186825`.

[116] Hao Gong, Jiayu Huang, Jianhua Liu, and Xinjian Deng. "Proof-of-concept study of high-order sideband for bolt loosening detection using vibroacoustic modulation method". In: *Mech. Syst. Signal Process.* 169 (Apr. 2022), p. 108638. DOI: `10.1016/j.ymssp.2021.108638`.

[117] N. Wilkie-Chancellier and K. Van Den Abeele. "Experimental detection of structural damage in natural building stones using non-linear wave modulation spectroscopy". In: *AIP Conf. Proc.* 760.May (2005), pp. 361–368. DOI: `10.1063/1.1916699`.

[118] Tingyuan Yin, Wanlin Meng, Neda Talebzadeh, and Jun Chen. “Experimental characterization of sulfate damage of concrete based on the harmonic wave modulation technique”. In: *AIP Conf. Proc.* 1806.February 2017 (2017). DOI: `10.1063/1.4974633`.

[119] Jun Chen, Yuning Wu, Tinyuan Yin, Neda Talebzadeh, and Quanquan Guo. “Characterization of concentrated and distributed cracks in concrete using a harmonic wave modulation technique”. In: *Mater. Struct. Constr.* 51.1 (2018), pp. 1–10. DOI: `10.1617/s11527-017-1129-0`.

[120] Sarah Miele, Pranav M Karve, Sankaran Mahadevan, and Vivek Agarwal. “Diagnosis of internal cracks in concrete using vibro-acoustic modulation and machine learning”. In: *Struct. Heal. Monit.* 0.0 (2022), p. 147592172110479. DOI: `10.1177/14759217211047901`.

[121] Ruztamreen B Jenal and Wieslaw J Staszewski. “Crack detection in glass plates using non-linear acoustics with low-profile piezoceramic transducers”. In: *Health Monitoring of Structural and Biological Systems 2010.* Vol. 7650. SPIE. 2010, pp. 924–933.

[122] T. Goursolle, S. Dos Santos, O. Bou Matar, and S. Callé. “Non-linear based time reversal acoustic applied to crack detection: Simulations and experiments”. In: *Int. J. Non. Linear. Mech.* 43.3 (2008), pp. 170–177. DOI: `10.1016/j.ijnonlinmec.2007.12.008`.

[123] Dariusz Broda, Krzysztof Mendrok, Vadim V. Silberschmidt, Lukasz Pieczonka, and Wieslaw J Staszewski. “The Study of Localized Crack-Induced Effects of non-linear Vibro-Acoustic Modulation”. In: *Materials (Basel).* 16.4 (Feb. 2023), p. 1653. DOI: `10.3390/ma16041653`.

[124] Mohammad M. Bazrafkan and Marcus Rutner. “Defect Localization in Metal Plates Using Vibroacoustic Modulation”. In: *Ndt* 1.1 (2023), pp. 3–21. DOI: `10.3390/ndt1010002`.

[125] Dimitri Donskoy, A. Zagrai, A. Chudnovsky, E. Golovin, and V. Agarwala. “non-linear vibro-acoustic modulation technique for life prediction of aging aircraft components”. In: *Proc. 3rd Eur. Work. - Struct. Heal. Monit. 2006* January (2006), pp. 251–258.

[126] Majid Ramezani. “Enhancement of Joining Method and Damage Detection Methodology in Structural Materials”. PhD thesis. STEVENS INSTITUTE OF TECHNOLOGY, 2018.

[127] Hyung Jin Lim and Hoon Sohn. "Necessary conditions for non-linear ultrasonic modulation generation given a localized fatigue crack in a plate-like structure". In: *Materials (Basel).* 10.3 (2017). DOI: `10.3390/ma10030248`.

[128] Hyung Jin Lim, Hoon Sohn, and Yongtak Kim. "Data-driven fatigue crack quantification and prognosis using non-linear ultrasonic modulation". In: *Mech. Syst. Signal Process.* 109 (2018), pp. 185–195. DOI: `10.1016/j.ymssp.2018.03.003`.

[129] Bo Yang Chen, Su Kiat Soh, Heow Pueh Lee, Tong Earn Tay, and Vincent B.C. Tan. "A vibro-acoustic modulation method for the detection of delamination and kissing bond in composites". In: *J. Compos. Mater.* 50.22 (2016), pp. 3089–3104. DOI: `10.1177/0021998315615652`.

[130] Peipei Liu, Hoon Sohn, Tribikram Kundu, and Suyoung Yang. "Non-contact detection of fatigue cracks by laser non-linear wave modulation spectroscopy (LNWMS)". In: *NDT E Int.* 66 (2014), pp. 106–116. DOI: `10.1016/j.ndteint.2014.06.002`.

[131] Peipei Liu, Hyung Jin Lim, Suyoung Yang, Hoon Sohn, Cheul Hee Lee, Yung Yi, Daewoo Kim, Jinhwan Jung, and In Hwan Bae. "Development of a "stick-and-detect" wireless sensor node for fatigue crack detection". In: *Struct. Heal. Monit.* 16.2 (2017), pp. 153–163. DOI: `10.1177/1475921716666532`.

[132] Abdullah Alnutayfat, Sophia Hassiotis, Dong Liu, and Alexander Sutin. "Sideband Peak Count in a Vibro-Acoustic Modulation Method for Crack Detection". In: *Acoustics* 4.1 (2022), pp. 74–86. DOI: `10.3390/acoustics4010005`.

[133] Dimitri Donskoy and Dong Liu. "Vibro-acoustic modulation baseline-free non-destructive testing". In: *J. Sound Vib.* 492 (2021), p. 115808. DOI: `10.1016/j.jsv.2020.115808`.

[134] Behnoush Golchinfar, Majid G. Ramezani, Dimitri Donskoy, and Hossain Saboonchi. "Vibro-acoustic modulation technique comparison with conventional non-destructive evaluation methods". In: *Heal. Monit. Struct. Biol. Syst. IX*. Ed. by Paul Fromme and Zhongqing Su. May 2020. SPIE, Apr. 2020, p. 77. DOI: `10.1117/12.2558905`.

[135] Dimitri Donskoy and Majid Ramezani. "Separation of amplitude and frequency modulations in Vibro-Acoustic Modulation non-destructive testing method". In: *Proc. Meet. Acoust.* Vol. 34. 1. 2018, p. 045002. DOI: `10.1121/2.0000831`.

[136] Zhongqing Su, Chao Zhou, Ming Hong, Li Cheng, Qiang Wang, and Xinlin Qing. "Acousto-ultrasonics-based fatigue damage characterization: Linear versus non-linear signal features". In: *Mech. Syst. Signal Process.* 45.1 (2014), pp. 225–239. DOI: `10.1016/j.ymssp.2013.10.017`.

[137] Feilong Li, Youxuan Zhao, Peng Cao, and Ning Hu. "Mixing of ultrasonic Lamb waves in thin plates with quadratic non-linearity". In: *Ultrasonics* 87 (2018), pp. 33–43. DOI: `10.1016/j.ultras.2018.02.005`.

[138] P Kijanka, R Radecki, P Packo, W J Staszewski, and T Uhl. "GPU-based local interaction simulation approach for simplified temperature effect modelling in Lamb wave propagation used for damage detection". In: 22.3 (2013), p. 35014. DOI: `10.1088/0964-1726/22/3/035014`.

[139] Jun Jia, Haifeng Hu, Limin Tao, and Yongpan Hu. "In situ measurement of fatigue crack opening stresses by non-linear vibro-acoustic modulation testing". In: *Adv. Mech. Eng.* 9.7 (2017), pp. 1–12. DOI: `10.1177/1687814017706265`.

[140] Ashish Kumar Singh, Boyang Yang Chen, Vincent B. C. Tan, Tong Earn Tay, and Heow Pueh Lee. "A theoretical and numerical study on the mechanics of vibro-acoustic modulation". In: *J. Acoust. Soc. Am.* 141.4 (2017), pp. 2821–2831. DOI: `10.1121/1.4981133`.

[141] Yanfeng Shen and Carlos E S Cesnik. "Modeling Guided Wave Propagation in Composite Structures Using Local Interaction Simulation Approach{\normalfont, in} Structural Health Monitoring for Advanced Composite Structures". In: 2018. Chap. 2, pp. 47–91.

[142] Dong Liu and Dimitri Donskoy. "Cross-correlation vibro-acoustic modulation method for damage detection". In: *Struct. Heal. Monit.* (2023), pp. 1–20. DOI: `10.1177/14759217231177005`.

[143] Bin Liu, Tie Gang, Chuhao Wan, Changxi Wang, and Zhiwei Luo. "Analysis of non-linear modulation between sound and vibrations in metallic structure and its use for damage detection". In: *Nondestruct. Test. Eval.* 30.3 (2015), pp. 277–290. DOI: `10.1080/10589759.2015.1034718`.

[144] A Frau, F Aymerich, M C Porcu, L Pieczonka, A Klepka, and W J Staszewski. “Probing wave frequency selection for the non-linear vibro-acoustic wave modulation tests”. In: *AIAS – Assoc. Ital. per l’Analisi delle Sollecitazioni, 43° Convegno Naz.* January (2014), pp. 9–12.

[145] Andrzej Klepka, Wieslaw Staszewski, Kajetan Dziedziech, and Francesco Aymerich. “Non-Linear Vibro-Acoustic Wave Modulations - Analysis of Different Types of Low-Frequency Excitation”. In: *Key Eng. Mater.* 569-570.2 (2013), pp. 924–931. DOI: `10.4028/www.scientific.net/kem.569-570.924`.

[146] Kay Smarsly, Mathias Worm, Kosmas Dragos, José Joaquín Peralta Abadía, Marc Wenner, and Oliver Hahn. “Mobile structural health monitoring using quadruped robots”. In: *Health Monitoring of Structural and Biological Systems XVI.* Vol. 12048. SPIE. 2022, pp. 404–417.

[147] Ye Lu, Lin Ye, Zhongqing Su, Limin Zhou, and Li Cheng. “Artificial Neural Network (ANN)-based crack identification in aluminum plates with lamb wave signals”. In: *J. Intell. Mater. Syst. Struct.* 20.1 (2009), pp. 39–49. DOI: `10.1177/1045389X07088782`.

[148] A. De Fenza, A. Sorrentino, and P. Vitiello. “Application of Artificial Neural Networks and Probability Ellipse methods for damage detection using Lamb waves”. In: *Compos. Struct.* 133.January 2018 (2015), pp. 390–403. DOI: `10.1016/j.compstruct.2015.07.089`.

[149] Vincentius Ewald, Roger M. Groves, and Rinze Benedictus. “DeepSHM: a deep learning approach for structural health monitoring based on guided Lamb wave technique”. In: March (2019), p. 19. DOI: `10.1117/12.2506794`.

[150] Iuliana Tabian, Hailing Fu, and Zahra Sharif Khodaei. “A Convolutional Neural Network for Impact Detection and Characterization of Complex Composite Structures”. In: *Sensors (Basel).* 19.22 (2019), pp. 1–25. DOI: `10.3390/s19224933`.

[151] Joel B. Harley and Daniel Sparkman. “Machine learning and NDE: Past, present, and future”. In: *AIP Conf. Proc.* 2102.May (2019). DOI: `10.1063/1.5099819`.

[152] Jinho Jang, Hoon Sohn, and Hyung Jin Lim. “Spectral noise and data reduction using a long short-term memory network for nonlinear ultrasonic modulation-based fatigue crack detection”. In: *Ultrasonics* 129.December (2023). DOI: `10.1016/j.ultras.2022.106909`.

[153] Keith A. Vehorn. “Vibro-acoustic Modulation as a Baseline-free Structural Health Monitoring Technique”. In: *Master’s Thesis: University of Dayton* (2013).

[154] Ulf Paul Breuer. *Commercial aircraft composite technology.* 2016, pp. 1–257. DOI: `10.1007/978-3-319-31918-6`.

[155] Bastien Ehrhart, Bernd Valeske, C. Muller, and Clemens Bockenheimer. “Methods for the Quality Assessment of Adhesive Bonded CFRP Structures - A Resumé”. In: *AIP Conf. Proc.* 44.3 (2010), pp. 1–8. DOI: `10.1109/TUFFC.924`.

[156] C. J. Brotherhood, B. W. Drinkwater, and S. Dixon. “The detectability of kissing bonds in adhesive joints using ultrasonic techniques”. In: *Ultrasonics* 41.7 (2003), pp. 521–529. DOI: `10.1016/S0041-624X(03)00156-2`.

[157] Theodor A. Schmid Fuertes, Thomas Kruse, Thomas Körwien, and Matthias Geistbeck. “Bonding of CFRP primary aerospace structures - Discussion of the certification boundary conditions and related technology fields addressing the needs for development”. In: *Compos. Interfaces* 22.8 (2015), pp. 795–808. DOI: `10.1080/09276440.2015.1077048`.

[158] Lennert Heilmann. “Qualitätskontrolle von Reparaturklebungen an Faserverbundstrukturen durch vollflächige Festigkeitsprüfung”. In: (2020).

[159] R. Jairaja and G. Narayana Naik. “Weak bond effects in adhesively bonded joints between the dissimilar adherends”. In: *J. Adhes.* 00.00 (2019), pp. 1–23. DOI: `10.1080/00218464.2019.1702027`.

[160] Baiyang Ren and Cliff J. Lissenden. “Ultrasonic guided wave inspection of adhesive bonds between composite laminates”. In: *Int. J. Adhes. Adhes.* 45 (2013), pp. 59–68. DOI: `10.1016/j.ijadhadh.2013.04.001`.

[161] F. Heidarpour, M. Farahani, and P. Ghabezi. “Experimental investigation of the effects of adhesive defects on the single lap joint strength”. In: *Int. J. Adhes. Adhes.* 80.August 2017 (2018), pp. 128–132. DOI: `10.1016/j.ijadhadh.2017.08.005`.

[162] Peiyu Wang, Zhencheng Li, Licheng Zhou, and Yongmao Pei. “Microwave non-destructive detection and quantitative evaluation of kissing defects in GFRP laminates”. In: *Compos. Sci. Technol.* 162.November 2017 (2018), pp. 117–122. DOI: `10.1016/j.compscitech.2018.04.029`.

[163] Michael Wood, Peter Charlton, and Dawei Yan. “Ultrasonic evaluation of artificial kissing bonds in CFRP composites”. In: *e-Journal Nondestruct. Test.* 19.12 (2014), pp. 1–10.

[164] Bengisu Yilmaz and Elena Jasiūnienė. “Advanced ultrasonic NDT for weak bond detection in composite-adhesive bonded structures”. In: *Int. J. Adhes. Adhes.* 102 (2020). DOI: `10.1016/j.ijadhadh.2020.102675`.

[165] Bastien Ehrhart, Romain Ecault, Fabienne Touchard, Michel Boustie, Laurent Berthe, Clemens Bockenheimer, and Bernd Valeske. “Development of a laser shock adhesion test for the assessment of weak adhesive bonded CFRP structures”. In: *Int. J. Adhes. Adhes.* 52 (2014), pp. 57–65. DOI: `10.1016/j.ijadhadh.2014.04.002`.

[166] Peter B. Nagy. “Ultrasonic classification of imperfect interfaces”. In: *J. Nondestruct. Eval.* 11.3-4 (1992), pp. 127–139. DOI: `10.1007/BF00566404`.

[167] C. Jeenjitkaew, Zofia Luklinska, and Felicity Guild. “Morphology and surface chemistry of kissing bonds in adhesive joints produced by surface contamination”. In: *Int. J. Adhes. Adhes.* 30.7 (2010), pp. 643–653. DOI: `10.1016/j.ijadhadh.2010.06.005`.

[168] Sergej Harder, Florian Röper, Dennis Gibhardt, Benedikt Koert, and Bodo Fiedler. “Strength of scarf-bonded CFRP repairs containing disc-shaped zones of weak bonding considering hot-wet conditioning”. In: *Int. J. Adhes. Adhes.* 102 (Oct. 2020), p. 102643. DOI: `10.1016/j.ijadhadh.2020.102643`.

[169] Taru Singhal, Eunho Kim, Tae Yeon Kim, and Jinkyu Yang. “Weak bond detection in composites using highly non-linear solitary waves”. In: *Smart Mater. Struct.* 26.5 (2017). DOI: `10.1088/1361-665X/aa6823`.

[170] Dawei Yan, Bruce W. Drinkwater, and Simon A. Neild. “Measurement of the ultrasonic non-linearity of kissing bonds in adhesive joints”. In: *NDT E Int.* 42.5 (2009), pp. 459–466. DOI: `10.1016/j.ndteint.2009.02.002`.

[171] Camille Gauthier, Mounsif Ech-Cherif El-Kettani, Jocelyne Galy, Mihai Predoi, and Damien Leduc. “Structural adhesive bonding characterization using guided Lamb waves and the vertical modes”. In: *Int. J. Adhes. Adhes.* 98.November 2019 (2020), p. 102467. DOI: `10.1016/j.ijadhadh.2019.102467`.

[172] Jakub Spytek, Aleksandra Ziaja-Sujdak, Kajetan Dziedziech, Lukasz Pieczonka, Ivan Pelivanov, and Lukasz Ambrozinski. “Evaluation of disbonds at various interfaces of adhesively bonded aluminum plates using all-optical excitation and detection of zero-group velocity Lamb waves”. In: *NDT E Int.* 112 (2020), p. 102249. DOI: `10.1016/j.ndteint.2020.102249`.

[173] R. L. Vijaya Kumar, M. R. Bhat, and C. R.L. L Murthy. “Evaluation of kissing bond in composite adhesive lap joints using digital image correlation: Preliminary studies”. In: *Int. J. Adhes. Adhes.* 42 (2013), pp. 60–68. DOI: `10.1016/j.ijadhadh.2013.01.004`.

[174] Romain Ecault, Fabienne Touchard, Laurent Berthe, and Michel Boustie. “Laser shock adhesion test numerical optimization for composite bonding assessment”. In: *Compos. Struct.* 247.May (2020), p. 112441. DOI: `10.1016/j.compstruct.2020.112441`.

[175] Office of the Federal Register National Archives and Records Administration. “Damage tolerance and fatigue evaluation of structure”. In: *14 CFR § 23.573* (2017), pp. 241–242.

[176] U.S. Department of Transportation. Federal Aviation Administration and Federal Aviation Administration. “Advisory Circular Advisory Circular”. In: *Aviation* 1.AC 25.1529-1A (2012), pp. 1–2. DOI: `10.1177/004728757301200242`.

[177] ASTM D5868-01(2014). “Standard Test Method for Lap Shear Adhesion for fibre Reinforced Plastic (FRP) Bonding”. In: *ASTM Int. West Conshohocken, PA* (2014). DOI: `10.1520/D5868-01R14`.

[178] Gerhard Mook, Christian Willberg, Ulrich Gabbert, and Jürgen Pohl. “Lamb wave mode conversion in CFRP plates”. In: *11th Eur. Conf. Non-Destructive Test.* October (2014). DOI: `10.13140/2.1.3372.4161`.

[179] François Chollet *et al. Keras.* 2015.

[180] TensorFlow-Developers. *TensorFlow.* 2021. DOI: `10.5281/zenodo.4758419`.

[181] James Bergstra and Yoshua Bengio. “Random Search for Hyper-Parameter Optimization”. In: *J. Mach. Learn. Res.* 13.null (2012), pp. 281–305.

[182] Diederik P. Kingma and Jimmy Lei Ba. “Adam: A method for stochastic optimization”. In: *3rd Int. Conf. Learn. Represent. ICLR 2015 - Conf. Track Proc.* (2015), pp. 1–15. arXiv: `1412.6980`.

[183] Christopher M Bishop. *Pattern Recognition and Machine Learning (Information Science and Statistics).* Springer, 2006. ISBN: 0387310738.

[184] Scott M. Lundberg, Su-In Lee, and Lee Su-In. “A Unified Approach to Interpreting Model Predictions”. In: *Adv. Neural Inf. Process. Syst. 30.* Ed. by I Guyon, U V Luxburg, S Bengio, H Wallach, R Fergus, S Vishwanathan, and R Garnett. Vol. 32. 2. Curran Associates, Inc., 2017, pp. 4765–4774. arXiv: `1610.07524 [stat.AP]`.

[185] Christoph Molnar. *Interpretable machine learning.* Lulu. com, 2020.

[186] G David Garson. “Interpreting Neural-Network Connection Weights”. In: *AI Expert* 6.4 (1991), pp. 46–51.

[187] Andreas Fischer. “Garson’s method trumps Olden’s method in every case - How to determine relative importance of input-variables in non-linear regression with artificial neural networks”. In: *Ecol. Modell.* 309-310 (2015), pp. 60–63. DOI: `10.1016/j.ecolmodel.2015.04.015`.

[188] Sylvie Legendre, Daniel Massicotte, Jacques Goyette, and Tapan K. Bose. “Neural classification of lamb wave ultrasonic weld testing signals using wavelet coefficients”. In: *IEEE Trans. Instrum. Meas.* 50.3 (2001), pp. 672–678. DOI: `10.1109/19.930439`.

[189] Peng Gao, Chunfei Wang, Yipo Li, and Zheng Cong. “Electromagnetic and eddy current NDT in weld inspection: A review”. In: *Insight - Non-Destructive Testing and Condition Monitoring* 57 (June 2015). DOI: `10.1784/insi.2015.57.6.337`.

[190] Furkan SOYTURK, Alper GUNOZ, and Memduh KARA. “Detection of Welding Defects by Non-Destructive Testing Methods”. In: *Int. Conf. Appl. Eng. Nat. Sci.* 1.1 (2023), pp. 424–427. DOI: `10.59287/icaens.1033`.

[191] Saad Mohammed. “NDT and SHM Methods of Damage Detection in Welded Structures”. In: March (2016), p. 152.

[192] Volkmar Schuler. *Praxiswissen Schweißtechnik*. 6. Auflage. Springer-Verlag, 2019. ISBN: 978-3-658-24265-7.

[193] Günter Schulze. *Die Metallurie des Schweißens, Eisenwerkstoffe - Ncihteisenmetallische Werkstoffe*. 4. Auflage. 2010, p. 614. ISBN: 9783642031823.

[194] Wolfram Lohse, Jörg Laumann, and Christian Wolf. *Stahlbau 1: Bemessung von stahlbauten nach eurocode mit zahlreichen beispielen*. Springer-Verlag, 2016.

[195] Hyung Jin Lim and Hoon Sohn. "Online fatigue crack prognosis using non-linear ultrasonic modulation". In: *Struct. Heal. Monit.* 2 (2019). DOI: `10.1177/1475921719828271`.

[196] Jakob Brunow, Niclas Spalek, Fawad Mohammadi, and Marcus Rutner. "Nanostructured metallic multilayer for superior fatigue strength of welded joints – a new post-weld treatment". In: (Aug. 2023). DOI: `10.21203/rs.3.rs-3293490/v1`.

[197] Christian Renner, Stefan Unterschütz, Volker Turau, and Kay Römer. "Perpetual Data Collection with Energy-Harvesting Sensor Networks". In: *ACM Trans. Sens. Networks* 11 (2014), 12:1–12:45.

[198] Amir H Alavi, Hassene Hasni, Pengcheng Jiao, Kenji Aono, Nizar Lajnef, and Shantanu Chakrabartty. "Self-charging and self-monitoring smart civil infrastructure systems: current practice and future trends". In: *Sensors and Smart Structures Technologies for Civil, Mechanical, and Aerospace Systems 2019*. Vol. 10970. International Society for Optics and Photonics. 2019, 109700W.

[199] Peter Oppermann and Bernd Christian Renner. "Acoustic Backscatter Communication and Power Transfer for Batteryless Wireless Sensors". In: *Sensors* 23.7 (2023), pp. 1–26. DOI: `10.3390/s23073617`.

[200] Wieslaw Ostachowicz, Rohan Soman, and Pawel Malinowski. "Optimization of sensor placement for structural health monitoring: a review". In: *Struct. Heal. Monit.* 18.3 (2019), pp. 963–988. DOI: `10.1177/1475921719825601`.

[201] R.M. Gray and D.L. Neuhoff. "Quantization". In: *IEEE Transactions on Information Theory* 44.6 (1998), pp. 2325–2383. DOI: `10.1109/18.720541`.

[202] Eric W Weisstein. *Fourier Series–Square Wave.* From MathWorld–A Wolfram Web Resource. URL: `https://mathworld.wolfram.com/FourierSeriesSquareWave.html`.

[203] Andrzej Klepka, Wieslaw Staszewski, Dario di Maio, Fabrizio Scarpa, Kong Fah Tee, and Tadeusz Uhl. “Sensor Location Analysis in non-linear Acoustics Used for Damage Detection in Composite Chiral Sandwich Panels”. In: *Adv. Sci. Technol.* 83 (2012), pp. 223–231. DOI: `10.4028/www.scientific.net/ast.83.223`.

[204] John Alexiou. *Describe a sine wave of known frequency with only two points.* Mathematics Stack Exchange. Mar. 2013. URL: `https://math.stackexchange.com/q/383910`.

[205] D. Broda, Wieslaw J. Staszewski, A. Martowicz, T. Uhl, and V. V. Silberschmidt. “Modelling of non-linear crack-wave interactions for damage detection based on ultrasound - A review”. In: *J. Sound Vib.* 333.4 (2014), pp. 1097–1118. DOI: `10.1016/j.jsv.2013.09.033`.

[206] Dimitri Donskoy, Behnoush Golchinfar, Majid Ramezani, Marcus Rutner, and Sophia Hassiotis. “Vibro-acoustic amplitude and frequency modulations during fatigue damage evolution”. In: *AIP Conf. Proc.* 2102.May (2019). DOI: `10.1063/1.5099754`.

[207] *Analyse des Einflusses der Temperatur auf das Werkstoffverhalten an Faserfehlorientierungen in dickwandigen Faser-Kunststoff-Verbunden.* URL: `https://gepris.dfg.de/gepris/projekt/428324840`.

[208] A. E. Ekimov, I. N. Didenkulov, and V. V. Kazakov. “Modulation of torsional waves in a rod with a crack”. In: *J. Acoust. Soc. Am.* 106.3 (1999), pp. 1289–1292. DOI: `10.1121/1.427163`.

[209] P.A. Johnson, A. Sutin, and K.E.-A. Van Den Abeele. “Application of non-linear wave modulation spectroscopy to discern material damage”. In: *Emerg. Technol. NDT.* 1999, pp. 159–166. DOI: `10.1201/9781003078586-28`.

[210] Koen E.A. Van Den Abeele, Alexander Sutin, Jan Carmeliet, and Paul A. Johnson. “Micro-damage diagnostics using non-linear elastic wave spectroscopy (NEWS)”. In: *NDT E Int.* 34.4 (2001), pp. 239–248. DOI: `10.1016/S0963-8695(00)00064-5`.

[211] Z. Parsons and Wieslaw Staszewski. "non-linear acoustics with low-profile piezoceramic excitation for crack detection in metallic structures". In: *Smart Mater. Struct.* 15.4 (2006), pp. 1110–1118. DOI: `10.1088/0964-1726/15/4/025`.

[212] U. Polimeno and M. Meo. "Understanding the effect of boundary conditions on damage identification process when using non-linear elastic wave spectroscopy methods". In: *Int. J. Non. Linear. Mech.* 43.3 (2008), pp. 187–193. DOI: `10.1016/j.ijnonlinmec.2007.12.013`.

[213] Dimitri Donskoy, Alexander Chudnovsky, Andrei Zagrai, Edvard Golovin, and Vinod Agarwala. "Fatigue Damage Monitoring and Remaning Life Assessment using non-linear Vibro-Modulation Technique". In: *J. Acoust. Soc. Am.* 123.5 (May 2008), pp. 3396–3396. DOI: `10.1121/1.2934077`.

[214] Ladislav Straka, Yuriy Yagodzinskyy, Michal Landa, and Hannu Hänninen. "Detection of structural damage of aluminum alloy 6082 using elastic wave modulation spectroscopy". In: *NDT E Int.* 41.7 (Oct. 2008), pp. 554–563. DOI: `10.1016/j.ndteint.2008.04.004`.

[215] M. Ryles, F. H. Ngau, I. McDonald, and Wieslaw Staszewski. "Comparative study of non-linear acoustic and Lamb wave techniques for fatigue crack detection in metallic structures". In: *Fatigue Fract. Eng. Mater. Struct.* 31.8 (2008), pp. 674–683. DOI: `10.1111/j.1460-2695.2008.01253.x`.

[216] T. J. Ulrich, A. M. Sutin, R. A. Guyer, and P. A. Johnson. "Time reversal and non-linear elastic wave spectroscopy (TR NEWS) techniques". In: *Int. J. Non. Linear. Mech.* 43.3 (2008), pp. 209–216. DOI: `10.1016/j.ijnonlinmec.2007.12.017`.

[217] K. Zacharias, E. Balabanidou, I. Hatzokos, I. T. Rekanos, and A. Trochidis. "Microdamage evaluation in human trabecular bone based on non-linear ultrasound vibro-modulation (NUVM)". In: *J. Biomech.* 42.5 (2009), pp. 581–586. DOI: `10.1016/j.jbiomech.2008.12.018`.

[218] V. Yu Zaitsev, L. A. Matveev, and A. L. Matveyev. "On the ultimate sensitivity of non-linear-modulation method of crack detection". In: *NDT E Int.* 42.7 (2009), pp. 622–629. DOI: `10.1016/j.ndteint.2009.05.001`.

[219] Kyung-Young Jhang. "non-linear ultrasonic techniques for non-destructive assessment of micro damage in material: A review". In: *Int. J. Precis. Eng. Manuf.* 10.1 (Jan. 2009), pp. 123–135. DOI: `10.1007/s12541-009-0019-y`.

[220] Andrzej Klepka, Wieslaw Staszewski, Francesco Aymerich, and Tadeusz Uhl. "Sensor location analysis for non-linear-acoustics-based damage detection in composite structures". In: *Heal. Monit. Struct. Biol. Syst. 2012* 8348.April 2012 (2012), 83482G. DOI: `10.1117/12.915282`.

[221] Chul Min Yeum, Hoon Sohn, Jeong Beom Ihn, and Hyung Jin Lim. "Instantaneous delamination detection in a composite plate using a dual piezoelectric transducer network". In: *Compos. Struct.* 94.12 (2012), pp. 3490–3499. DOI: `10.1016/j.compstruct.2012.06.003`.

[222] Andrzej Klepka, Wieslaw Staszewski, Dario Di Maio, and Fabrizio Scarpa. "Impact damage detection in composite chiral sandwich panels using non-linear vibro-acoustic modulations". In: *Smart Mater. Struct.* 22.8 (2013). DOI: `10.1088/0964-1726/22/8/084011`.

[223] Y. Zhang, V. Tournat, O. Abraham, O. Durand, S. Letourneur, A. Le Duff, and B. Lascoup. "Nonlinear mixing of ultrasonic coda waves with lower frequency-swept pump waves for a global detection of defects in multiple scattering media". In: *J. Appl. Phys.* 113.6 (2013). DOI: `10.1063/1.4791585`.

[224] Lukasz Pieczonka, Andrzej Klepka, Wieslaw Staszewski, Tadeusz Uhl, and Francesco Aymerich. "Analysis of Vibro-Acoustic Modulations in non-linear Acoustics Used for Impact Damage Detection - Numerical and Experimental Study". In: *Key Eng. Mater.* 558 (2013), pp. 341–348. DOI: `10.4028/www.scientific.net/kem.558.341`.

[225] Dariusz Broda, Andrzej Klepka, Wieslaw J. Staszewski, and Fabrizio Scarpa. "non-linear acoustics in non-destructive testing - from theory to experimental application". In: *Key Eng. Mater.* 588 (2014), pp. 192–201. DOI: `10.4028/www.scientific.net/KEM.588.192`.

[226] Hyung Jin Lim, Hoon Sohn, Martin P. Desimio, and Kevin Brown. "Reference-free fatigue crack detection using non-linear ultrasonic modulation under various temperature and loading conditions". In: *Mech. Syst. Signal Process.* 45.2 (2014), pp. 468–478. DOI: `10.1016/j.ymssp.2013.12.001`.

[227] Lukasz Pieczonka, P. Ukowski, Andrzej Klepka, Wieslaw Staszewski, Tadeusz Uhl, and Francesco Aymerich. “Impact damage detection in light composite sandwich panels using piezo-based non-linear vibro-acoustic modulations”. In: *Smart Mater. Struct.* 23.10 (2014). DOI: `10.1088/0964-1726/23/10/105021`.

[228] Hyung Jin Lim, Hoon Sohn, and Peipei Liu. “Binding conditions for non-linear ultrasonic generation unifying wave propagation and vibration”. In: *Appl. Phys. Lett.* 104.21 (2014), pp. 1–5. DOI: `10.1063/1.4879836`.

[229] Gian Piero Malfense Fierro and Michele Meo. “Residual fatigue life estimation using a non-linear ultrasound modulation method”. In: *Smart Mater. Struct.* 24.2 (2015). DOI: `10.1088/0964-1726/24/2/025040`.

[230] Nikolaos A. Chrysochoidis, Theoni T. Assimakopoulou, and Dimitris A. Saravanos. “non-linear wave structural health monitoring method using an active non-linear piezoceramic sensor for matrix cracking detection in composites”. In: *J. Intell. Mater. Syst. Struct.* 26.15 (2015), pp. 2108–2120. DOI: `10.1177/1045389X14549865`.

[231] Lukasz Pieczonka, Andrzej Klepka, Kajetan Dziedziech, Dariusz Broda, Pawel Packo, Adam Martowicz, Tadeusz Uhl, and Wieslaw J. Staszewski. “non-linear acoustics for structural health monitoring - Classical vs. non-classical approaches”. In: *8th Eur. Work. Struct. Heal. Monit. EWSHM 2016* 1.July (2016), pp. 1–12.

[232] Hyung Jin Lim, Yongtak Kim, Gunhee Koo, Suyoung Yang, Hoon Sohn, In Hwan Bae, and Jeong Hwan Jang. “Development and field application of a non-linear ultrasonic modulation technique for fatigue crack detection without reference data from an intact condition”. In: *Smart Mater. Struct.* 25.9 (2016). DOI: `10.1088/0964-1726/25/9/095055`.

[233] Sylvain Mezil, Nikolay Chigarev, Vincent Tournat, and Vitalyi Gusev. “Evaluation of crack parameters by a non-linear frequency-mixing laser ultrasonics method”. In: *Ultrasonics* 69 (July 2016), pp. 225–235. DOI: `10.1016/j.ultras.2016.04.005`.

[234] Nan Li, Junjun Sun, Jingpin Jiao, Bin Wu, and Cunfu He. “Quantitative evaluation of micro-cracks using non-linear ultrasonic modulation method”. In: *NDT E Int.* 79 (Apr. 2016), pp. 63–72. DOI: `10.1016/j.ndteint.2015.12.003`.

[235] P. Blanloeuil, L. R.F. Rose, C. H. Wang, and M. Veidt. “Efficient Simulations of the Nonlinear Wave Modulation Induced by a Closed Crack Using Local Contact Modelling”. In: *Procedia Eng.* 188 (2017), pp. 201–208. DOI: `10.1016/j.proeng.2017.04.475`.

[236] Jun Jia, Haifeng Hu, Limin Tao, and Dingxin Yang. “Analysis of load effect on non-linear vibro-acoustic modulation used in on-line monitoring of fatigue cracks”. In: *Smart Mater. Struct.* 26.9 (2017). DOI: `10.1088/1361-665X/aa8149`.

[237] Phong B. Dao, Andrzej Klepka, Lukasz Pieczonka, Francesco Aymerich, Wieslaw Staszewski, Lukasz Pieczonka, and Francesco Aymerich. “Impact damage detection in smart composites using non-linear acoustics - Cointegration analysis for removal of undesired load effect”. In: *Smart Mater. Struct.* 26.3 (Feb. 2017). DOI: `10.1088/1361-665X/aa5744`.

[238] Bin Liu, Zhiwei Luo, and Tie Gang. “Influence of low-frequency parameter changes on non-linear vibro-acoustic wave modulations used for crack detection”. In: *Struct. Heal. Monit.* 17.2 (2018), pp. 218–226. DOI: `10.1177/1475921716689385`.

[239] Peipei Liu, Jinho Jang, Suyoung Yang, and Hoon Sohn. “Fatigue crack detection using dual laser induced non-linear ultrasonic modulation”. In: *Opt. Lasers Eng.* 110.May (2018), pp. 420–430. DOI: `10.1016/j.optlaseng.2018.05.025`.

[240] Yongtak Kim, Hyung Jin Lim, and Hoon Sohn. “non-linear ultrasonic modulation based failure warning for aluminum plates subject to fatigue loading”. In: *Int. J. Fatigue* 114.May (2018), pp. 130–137. DOI: `10.1016/j.ijfatigue.2018.05.014`.

[241] Majid G. Ramezani, Behnoush Golchinfar, Dimitri Donskoy, Sophia Hassiotis, and Giri Venkiteela. “Steel Material Degradation Assessment Via Vibro-Acoustic Modulation Technique”. In: *Transp. Res. Rec.* May (2019). DOI: `10.1177/0361198119838271`.

[242] A. Carcione, P. Blanloeuil, L. R.F. Rose, Chun H. Wang, and M. Veidt. “Modulated high frequency excitation approach to non-linear ultrasonic NDT”. In: *J. Sound Vib.* 446 (2019), pp. 238–248. DOI: `10.1016/j.jsv.2018.12.034`.

[243] Nesrine Houhat, Vincent Tournat, Sébastien Ménigot, Tarek Boutkedjirt, and Jean Marc Girault. "Optimal pump excitation frequency for improvement of damage detection by non-linear vibro acoustic modulation method in a multiple scattering sample". In: *Appl. Acoust.* 155 (2019), pp. 222–231. DOI: `10.1016/j.apacoust.2019.06.010`.

[244] Hyung Jin Lim, Young Joo Lee, and Hoon Sohn. "Continuous fatigue crack length estimation for aluminum 6061-T6 plates with a notch". In: *Mech. Syst. Signal Process.* 120 (2019), pp. 356–364. DOI: `10.1016/j.ymssp.2018.10.018`.

[245] Jakub Górski, Andrzej Klepka, Kajetan Dziedziech, Jakub Mrówka, Rafał Radecki, and Ziemowit Dworakowski. "Identification of the stick and slip motion between contact surfaces using artificial neural networks". In: *Nonlinear Dyn.* 100.1 (Apr. 2020), pp. 225–242. DOI: `10.1007/s11071-020-05515-8`.

[246] Pranav Karve and Sankaran Mahadevan. "On the performance of vibro-acoustic-modulation-based diagnosis of breathing cracks in thick, elastic slabs". In: *Struct. Control Heal. Monit.* 27.3 (2020), pp. 1–26. DOI: `10.1002/stc.2470`.

[247] Bin Liu, Jun Yang, and Tie Gang. "Analysis of sound and vibration interaction on a crack and its use in high-frequency parameter selection for vibro-acoustic modulation testing". In: *Mech. Syst. Signal Process.* 143 (Sept. 2020), p. 106835. DOI: `10.1016/j.ymssp.2020.106835`.

[248] Furui Wang and Gangbing Song. "Monitoring of multi-bolt connection looseness using a novel vibro-acoustic method". In: *non-linear Dyn.* 100.1 (2020), pp. 243–254. DOI: `10.1007/s11071-020-05508-7`.

[249] Nan Zhao, Linsheng Huo, and Gangbing Song. "A non-linear ultrasonic method for real-time bolt looseness monitoring using PZT transducer–enabled vibro-acoustic modulation". In: *J. Intell. Mater. Syst. Struct.* 31.3 (2020), pp. 364–376. DOI: `10.1177/1045389X19891534`.

[250] Bin Liu, Jun Yang, Guoqiang Zhang, and Tie Gang. "The choice of the sweep-frequency rate for the probing wave in non-linear-modulation method of crack detection in resonant samples". In: *NDT E Int.* 123.June (2021), p. 102524. DOI: `10.1016/j.ndteint.2021.102524`.

[251] Jianbin Li, Yi He, Qian Li, and Zhen Zhang. “Artificial Intelligence (AI)-Based Evaluation of Bolt Loosening Using Vibro-Acoustic Modulation (VAM) Features from a Combination of Simulation and Experiments”. In: *Appl. Sci.* 12.24 (2022). DOI: `10.3390/app122412920`.

[252] Volodymyr Gatsa, Nesrine Houhat, and Sébastien Ménigot. “Hybrid optimization of driving frequency for crack signature enhancement in nonlinear ultrasonic non-destructive testing”. In: *Appl. Acoust.* 195 (June 2022), p. 108810. DOI: `10.1016/j.apacoust.2022.108810`.

[253] Ashish Kumar Singh, Vincent B.C. Tan, Tong Earn Tay, and Heow Pueh Lee. “Numerical Investigations into non-linear Vibro-Ultrasonics and Surface Vibration Comparison Method for Detection of Defects in a Composite Laminate”. In: *J. Nondestruct. Eval. Diagnostics Progn. Eng. Syst.* 5.2 (2022), pp. 1–13. DOI: `10.1115/1.4052957`.

[254] Naserodin Sepehry, Mohammad Ehsani, Sina Asadi, Mahnaz Shamshirsaz, and Firooz Bakhtiari Nejad. “Fourier spectral element for simulation of vibro-acoustic modulation caused by contact non-linearity in the beam”. In: *Thin-Walled Struct.* 174 (Apr. 2022), p. 109112. DOI: `10.1016/j.tws.2022.109112`.

[255] Lunan Wei and Jun Chen. “Experimental and numerical characterization of delamination features in orthotropic CFRP laminates using pre-modulated waves”. In: *Appl. Acoust.* 201 (Dec. 2022), p. 109102. DOI: `10.1016/j.apacoust.2022.109102`.

[256] Krzysztof Czeluśniak, Wiesław J. Staszewski, and Francesco Aymerich. “Local bispectral characteristics of nonlinear vibro-acoustic modulations for structural damage detection”. In: *Mech. Syst. Signal Process.* 178 (Oct. 2022), p. 109199. DOI: `10.1016/j.ymssp.2022.109199`.

[257] Mohammad Ehsani, Mahnaz Shamshirsaz, Mojtaba Sadighi, Naserodin Sepehry, and Richard Loendersloot. “Theoretical and experimental investigations on control parameters of piezo-based vibro-acoustic modulation health monitoring of contact acoustic non-linearity in a sandwich beam”. In: *Appl. Acoust.* 203 (Feb. 2023), p. 109193. DOI: `10.1016/j.apacoust.2022.109193`.

[258] Xueliang Duan, Huifeng Zheng, Wenjie Du, Tianhao Ling, and Runguang Yao. “Research on nonlinear response analysis of micro-cracks un-

der vibro-acoustic modulation”. In: *Rev. Sci. Instrum.* 94.5 (2023). DOI: `10.1063/5.0140052`.

[259] Lunan Wei and Jun Chen. “Determination of optimal probing frequency for enhancing nonlinear vibro-acoustic modulation behaviors of delaminated CFRP based on local defect resonance”. In: *Mech. Syst. Signal Process.* 187 (2023), p. 109961. DOI: `https://doi.org/10.1016/j.ymssp.2022.109961`.

[260] Tingyuan Yin, Ching Tai Ng, James Vidler, Van Dac Ho, and Andrei Kotousov. “Characterization of thermal damage in graphene mortar materials using High-order sideband generation of Amplitude-modulation Vibro-acoustic technique”. In: *Mech. Syst. Signal Process.* 193.August 2022 (June 2023), p. 110259. DOI: `10.1016/j.ymssp.2023.110259`.

[261] Runye Lu, Yanfeng Shen, Bo Zhang, and Wu Xu. “Nonlinear Electro-Mechanical Impedance Spectroscopy for fatigue crack monitoring”. In: *Mech. Syst. Signal Process.* 184.March (Feb. 2023), p. 109749. DOI: `10.1016/j.ymssp.2022.109749`.

[262] Horace Lamb. “On waves in an elastic plate”. In: *Proceedings of the Royal Society of London. Series A, Containing papers of a mathematical and physical character* 93.648 (1917), pp. 114–128.

[263] Joseph L Rose. “Dispersion curves in guided wave testing”. In: *Materials Evaluation* 61.1 (2003), pp. 20–22.

[264] Jan D. Achenbach. *Wave propagation in elastic solids.* 3. print. North Holland series in applied mathematics and mechanics. Amsterdam u.a.: North-Holland Publishing Company, 1980. URL: `http://www.gbv.de/dms/bowker/toc/9780720403251.pdf`.

[265] Jan Achenbach. *Wave propagation in elastic solids.* Elsevier, 2012.

[266] Zi Zhang, Hong Pan, and Xingyu Wang. “Machine Learning-Enriched Lamb Wave Approaches”. In: (2020).

[267] Zhongqing Su and Lin Ye. “Identification of Damage Using Lamb Waves: From Fundamentals to Applications”. In: *Lect. Notes Appl. Comput. Mech.* 48 (2009). DOI: `10.1007/978-1-84882-784-4`.

[268] National Instruments. *Understanding FFTs and Windowing.* URL: `https://download.ni.com/evaluation/pxi/Understanding%20FFTs%20and%20Windowing.pdf` (visited on 11/01/2023).

[269] Tribikram Kundu. *non-linear ultrasonic and Vibro-acoustical techniques for Nondestructive evaluation*. 2018, pp. 1–759. DOI: `10.1007/978-3-319-94476-0`.

[270] Michael Cerna and Audrey F Harvey. *The Fundamentals of FFT-Based Signal Analysis and Measurement*. Tech. rep. National Instruments, 2000.

A. Appendix

A.1. VAM literature over the years

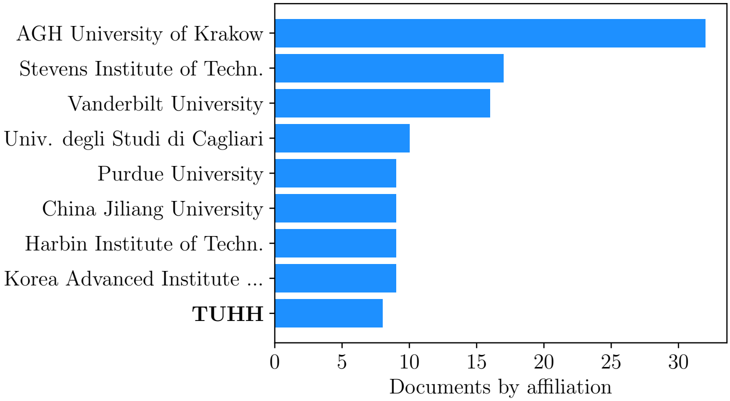

Figure A.1.: Number of publications sorted by the affiliation of the Scopus search.

Over the years, several VAM publications have been published. In this thesis, two databases of VAM literature are compared. The first is a database of cherry-picked publications, which were found by searching the internet and cross-references from other papers. Since not all of these documents are publicly accessible, several papers have not been included in the literature review of the main document. However, from the accessible information, 193 published documents have been found, which are related to VAM. These cherry-picked documents are compared to the results of a Scopus search for the variations of the method's name. All sources, where "Vibro-acoustic modulation", "Vibroacoustic modulation", "nonlinear wave modulation spectroscopy" or "nonlinear acoustic modulation" appears in the title, the abstract or the keywords, were collected. It should be noted, that this analysis was conducted in 12/2023. While the

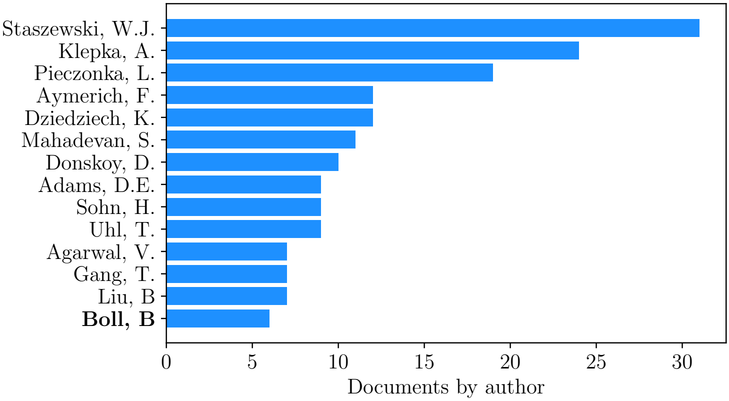

Figure A.2.: Number of publications sorted by the authors of the Scopus search.

number of publications was already shown as an accumulation over the years in Figure 2.5 of the main document, some additional observations will be shown in the following. In Figure A.1 the results of the Scopus search, which were counted for the mentioned affiliations and sorted for the authors in Figure A.2. It is obvious, that the team of the University of Krakow, including W. Staszewski, A. Klepka, and L. Pieczonka have contributed the most publications. Also, the Stevens Institute of Technology has produced 19 publications.

From the cherry-picked literature sources, the amount of publications is given for each year in Table A.1. These results are furthermore divided into published journal articles and other publications. "Other" in this case indicates a publication in a conference band, a published thesis by the university, book chapters or other sources. The referenced works are only journal articles.

Table A.1.: VAM Literature sorted by year

Year	Journals	Other	Journal publications
1998	3	0	[43, 45, 53]
1999	4	0	[44, 64, 208, 209]
2000	2	0	[41, 73]
2001	2	0	[55, 210]
2002	1	0	[60]
2004	2	0	[47, 89]
2006	5	1	[61, 66, 67, 69, 211]
2008	9	1	[68, 74, 85, 122, 212–216]
2009	3	1	[217–219]
2010	4	0	[49, 56, 91, 98]
2012	4	2	[90, 203, 220, 221]
2013	4	2	[145, 222–224]
2014	9	3	[81, 87, 102, 130, 205, 225–228]
2015	4	1	[39, 143, 229, 230]
2016	7	4	[76, 110, 129, 231–234]
2017	9	2	[63, 111, 127, 131, 139, 140, 235–237]
2018	9	8	[57, 82, 105, 119, 128, 137, 238–240]
2019	9	7	[77, 93, 106, 113, 195, 241–244]
2020	9	2	[21, 31, 50, 94, 95, 245–249]
2021	8	2	[9, 51, 78, 83, 96, 97, 133, 250]
2022	17	3	[13, 71, 79, 80, 108, 114–116, 120, 132, 251–256]
2023	18	3	[11, 14, 17, 58, 59, 72, 109, 123, 124, 142] [152, 257–261]
Sum	142	51	

A.2. Lamb waves

Lamb waves, also known as guided waves or plate waves, are a type of mechanical wave that propagates within thin plates or solid structures. Named after the British mathematician Sir Horace Lamb [262], these waves have unique properties that make them valuable for various applications in non-destructive testing (NDT), structural health monitoring (SHM), and materials characterisation.

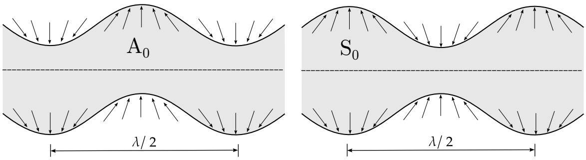

Figure A.3.: Particle displacement of the first anti-symmetric Lamb mode A_0 (left) and the first symmetric Lamb mode S_0 (right). The dashed line represents the centre of the plate.

Unlike traditional bulk waves, which propagate through the entire volume of a material, Lamb waves travel along the surfaces or interfaces of a structure. They are dispersive, meaning that their velocity depends on both frequency and the material properties of the medium through which they propagate [263].

Lamb waves are characterised by multiple modes, each with distinct phase velocities and dispersion characteristics. The primary Lamb wave modes include the symmetric Lamb mode (S_0), the anti-symmetric Lamb mode (A_0), and various higher-order modes (S_1, A_1, S_2, A_2, etc.). These modes exhibit different behaviours and can be selectively excited and detected based on their frequency and polarisation [264].

The fundamental A_0 and S_0 modes correspond to simple flexural/compressive modes, which are present at every excited frequency. They are visualised in Figure A.3. After a certain frequency, higher order Lamb wave modes occur, which are defined by an increased complexity within the displacement and, hence, also the evaluation.

The propagation behaviour of the Lamb wave modes can be described with their dispersion curves, where the phase and group velocities are plotted versus the excitation frequency. They can be expressed by the Rayleigh-Lamb equation [265]:

$$\frac{\tan(qh)}{\tan(ph)} = \frac{-4k^2pq}{(q^2-k^2)^2}\text{(Symmetric Lamb wave modes)} \tag{A.1}$$

$$\frac{\tan(qh)}{\tan(ph)} = \frac{\left(q^2-k^2\right)^2}{-4k^2pq}\text{(Anti-symmetric Lamb wave modes)} \tag{A.2}$$

$$\mathrm{q}^2 = \frac{\omega^2}{{c_T}^2} - \mathrm{k}^2, \mathrm{p}^2 = \frac{\omega^2}{c_L^2} - \mathrm{k}^2, k = \frac{2\pi}{\lambda}. \tag{A.3}$$

In these equations, k, f and h represent the wave number, frequency and plate thickness. The velocities of the longitudinal c_L and transverse/shear modes c_T are defined by

$$c_L = \sqrt{\frac{E(1-v)}{\rho(1+v)(1-2v)}} = \sqrt{\frac{2\mu(1-v)}{\rho(1-2v)}}, \quad c_T = \sqrt{\frac{E}{2\rho(1+v)}} = \sqrt{\frac{\mu}{\rho}}, \quad \text{(A.4)}$$

where E denotes the Young's modulus of the medium ($E = 2\mu(1+v)$), λ is the Lamé constant and v is the Poisson's ratio. Consequently, Lamb waves are essentially the superposition of transverse and longitudinal modes.

In Figure A.4 (left) the phase velocity for the different wave modes which are plotted over the frequency-thickness product is shown exemplarily for an aluminium plate. The dispersion behaviour in FRPs is more complex and dependent on the fibre directions of the laminate, and due to the different stiffness of the fibres compared to the matrix material. It can be seen, that the wave speed highly depends on the thickness or the frequency and the type of mode as described in equations A.2 and A.1. It can be estimated from this graph, that in plates with a thickness of up to 10 mm and a carrier frequency of 200 kHz only the fundamental Lamb wave modes occur.

Due to the differences in wave propagation, the different Lamb wave modes can be utilised in thin plate-like structures for the damage detection of different types. Zhang *et al.* [266] reviewed publications stating, that the S_0 mode—as shear wave—is more sensitive for internal damage, while the A_0 mode—as flexual wave–is sensitively for surface damages.

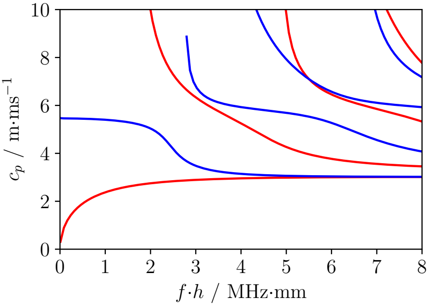

Figure A.4.: Theoretical dispersion curves of an aluminium plate.

For the application of Lamb waves in anisotropic, multi-layered structures like FRPs, further influences have to be taken into consideration. For example, depending on the fibre orientation and fibre layup of the structure, there are directional differences in wave speed, phase and group velocities. Furthermore, wave skewing, mode-conversions and other phenomenons occur [267].

A.3. Types of signal modulation

In this chapter, the different types of signal modulations which can be present in the VAM signal are presented. A VAM measurement can be the superposition of amplitude modulation (AM) and angular modulation, which can be further divided into frequency modulation (FM) and phase modulation (PM). Let the signal of the ultrasonic carrier wave be defined as

$$X_{\mathrm{c}}(t) = A_{\mathrm{c}} \cdot \sin(\omega_{\mathrm{c}} t) \tag{A.5}$$

and the pumping wave introduced by the hydraulic pulsing machine as

$$X_{\mathrm{p}}(t) = A_{\mathrm{p}} \cdot \cos(\omega_{\mathrm{p}} t + \phi_{\mathrm{p}}) \tag{A.6}$$

with $\omega = 2\pi f$, the individual frequencies $f_{\mathrm{p}} \ll f_{\mathrm{c}}$ and A as amplitude. Then, an amplitude-modulated signal can be combined to

$$\begin{aligned} X_{\mathrm{AM}} &= \left[1 + \frac{X_{\mathrm{p}}(t)}{A_{\mathrm{c}}}\right] X_{\mathrm{c}}(t) \\ &= \left[1 + m_a \cos\left(\omega_{\mathrm{p}} t + \phi_{\mathrm{p}}\right)\right] A_{\mathrm{c}} \sin\left(\omega_{\mathrm{c}} t\right). \end{aligned} \tag{A.7}$$

The amplitude modulation parameter $m_{\mathrm{a}} = A_{\mathrm{p}}/A_{\mathrm{c}}$ expresses the ratio from the amplitudes of the pumping wave to the carrier wave.

In contrast to the AM, both angular modulations are closely related, as shown in the following equations. A phase modulation between the given signals can be expressed as:

$$X_{\mathrm{PM}} = A_{\mathrm{c}} \sin\left(\omega_{\mathrm{c}} t + m_{\mathrm{p}} \cos\left(\omega_{\mathrm{p}} t\right) + \phi_{\mathrm{p}}\right) \tag{A.8}$$

and the frequency modulation, since $X_{\mathrm{p}}(t)$ is a sinusoidal as:

$$X_{\mathrm{FM}} = A_{\mathrm{c}} \sin\left(\omega_{\mathrm{c}} t + \frac{m_f}{\omega_{\mathrm{p}}} \cdot \sin\left(\omega_{\mathrm{p}} t\right) + \phi_{\mathrm{p}}\right). \tag{A.9}$$

Here, m_p is the phase modulation parameter, and m_f is the frequency modulation parameter. When comparing (A.8) and (A.9) it can be concluded that PM is shifted by $\pi/2$ which in addition to multi-path propagation through a specimen hinders a separation of FM and PM in an angular modulated signal. Therefore, in this thesis, the angular modulation is treated as pure PM.

A.4. Effect of windowing on the evaluation

To increase the precision of each measurement, the carrier and the sidebands have to be significantly above the noise floor in the frequency domain $\mathcal{F}$. Noise in $\mathcal{F}(X_\mathrm{r})$ is often a result of spectral leakage due to the FFT algorithm's assumption that the input signal is ideally repeated over the signal length and its periodicity from start to end. By measuring an unknown response, this periodicity is violated in many cases. Consequently, a distortion of the FFT occurs where energy from a given frequency component is spread over adjacent frequency bins [268]. Hence, the measured steady-state signals were convoluted with a Hanning-window function to reduce the noise and consequently allow the evaluation of more sidebands [87, 104, 269, 270]. The Hanning-window has been chosen since it smoothly converges to zero at both sides and, therefore, eliminates all discontinuities in the periodicity. Other window functions, like the Hamming window, end above zero and thus have a slight discontinuity in the signal [268].

The effect of a window function is shown in Figure A.5, where the frequency domain of a typical VAM measurement is shown. Distinct sidebands (Signal) are visible around the carrier since the periodicity was ensured in the VAM measurement setup. However, deleting the last value of the measured signal (2,000,000 points) results in a violation of these conditions, which results in severe spectral leakage (Unperiodic). Only the first sideband is visible, while the others are covered by spectral leakage. Convoluting the “Unperiodic” signal with a Hanning-window function restores the sidebands. One downside of using window functions is the reduced carrier and sideband amplitude. To prevent errors, it is important to compare only signals of the same length which were multiplied by the same window functions. Prior tests have shown excellent results and improved comparability if a Hanning window is applied to all signals.

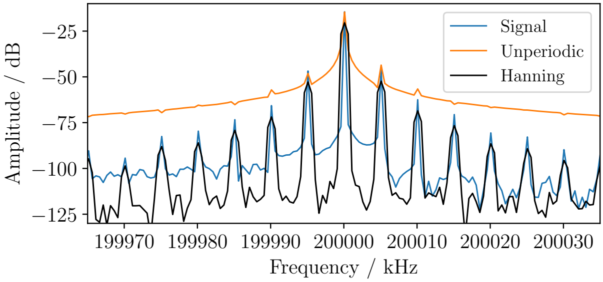

Figure A.5.: Comparison of the sidebands of a measured signal (Signal), the same signal without the last value to be unperiodic, and the unperiodic signal multiplied with a Hanning window function.

A.5. Adhesive bonding evaluation

Stress-strain curves from the mechanical testing of the single-lap shear specimen are illustrated in Figure A.6, displaying mean values and standard deviations for both the pristine specimen and the specimen with introduced defects. The standard deviation of the ultimate shear strength and elongation at break is typical. The standard deviation for ultimate shear strength and elongation at break is fairly typical for all adhesively bonded joints, but unexpectedly, it is highest for the pristine joints concerning shear strength. Since the introduced defects are centrally located and away from the edges of the bonded joint, the standard deviations overlap, resulting in only minor decreases in shear strength and elongation at break. This highlights the challenge of identifying defective bonded joints, as significant differences are nearly impossible to detect even with

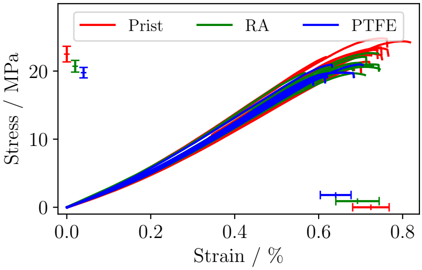

Figure A.6.: Stress-strain curves of the lap-shear specimen. The mean and standard deviation of the ultimate shear strength and elongation at break is marked for each class respectively next to the corresponding axis.

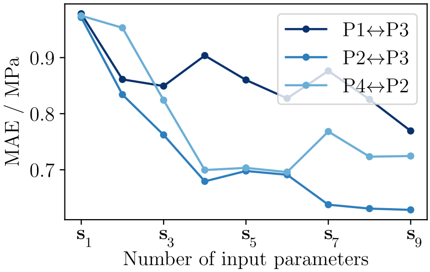

Figure A.7.: MAE reduces with more sidebands used for the evaluation.

destructive testing methods. Nonetheless, defective bonded specimens are likely to have a much shorter service life, leading to potentially dramatic consequences, which are more likely to become apparent during dynamic testing.

In Figure A.7, the decrease of the MAE is shown, if the ANN is trained on more sidebands of the VAM measurements. $\mathbf{s}_1$ in this case indicates, that the input to the ANN contains the amplitude of the carrier and the amplitudes of the first sideband to each side. This result is consistent with the evaluation of the classification, that was presented in the main document.

A.6. Welded steel evaluation

A.6.1. Manufacturing

In Chapter 4.2, the detection of welding defects in welded steel specimens was shown. Since the specimens originate from another research project [196], the precise manufacturing will be introduced in the following. The specimens were manufactured from two S355 structural steel plates with a thickness of 8 mm, a width of 300 mm and a length of 800 mm. Each plate was prepared for the welding by creating two chamfers of 45°. Two plates were mounted to a rig to assure the positioning and to prevent movement or bending.

The welds were introduced by a welding robot, joining two plates with the dimensions of $1 \times 0.4\,\mathrm{m}^2$. The process is shielded with a mixture of active and inert gases consisting of 18 % argon and 82 % carbon dioxide. To create a pristine set of specimens and additionally defect counterparts, this process was repeated for a second set of plates. Afterwards, a water-jet cutting machine is used to cut

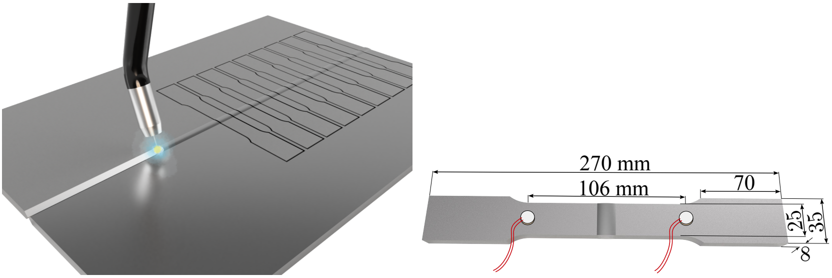

Figure A.8.: Manufacturing process of the welded dog-bone specimen (left) with the welding of two plates and the water-jet cutting to receive the final specimens (right).

30 equivalent specimens from each joined plate. The manufacturing process and the specimen dimensions are illustrated in Figure A.8.

The first specimen batch was produced with optimised welding parameters, resulting in an ideal weld.[1] During the production of the second batch, defects were introduced into the weld by altering the parameters.[2] These parameters resulted in slightly flatter welds compared to the first batch of the ideal specimens and, hence, indicates an unacceptably high degree of molten base material with a deep penetration of the molten zone. The combination led to an excessive mixing of the base material with the pure material in the electrode. An unfavourable crystallisation in the root of the weld is occurring, which results in a steep stiffness gradient that could initiate cracks, which reduce the joint strength and the fatigue life in particular [193]. In addition, the high temperature combined with the high cooling rate increased the risk of hot cracking [193]. In the text, the specimens with the altered welding parameters will be referred to as the *defect* group due to their inferior tensile and fatigue properties compared to the welded specimen with *ideal* parameters. To evaluate the influence of the weld on the VAM signal, three specimens of the same dimensions were cut from a similar steel plate and evaluated with VAM. Hence, they are *without* a weld.

A.6.2. Defect detection

In Figure 4.14, the MI was shown for the different classes, to evaluate if the MI is sufficient to differentiate between the three classes. As addition to the presented

---

[1] frontside: 165 A and 7 mm / s, backside: 200 A and 11 mm / s

[2] frontside: 165 A and 7 mm / s, backside: 165 A and 7 mm / s

results, the AM and PM values can be found in Figure A.9, for the comparison of the three specimen classes. However, the difference between the *ideal* and the *defect* specimens are minimal. However, the mean AM and PM of the specimens without a weld has a pronounced offset compared to the others. Therefore, no further information gain is achievable compared to the MI values, and more sophisticated methods of evaluating the VAM measurements were proposed.

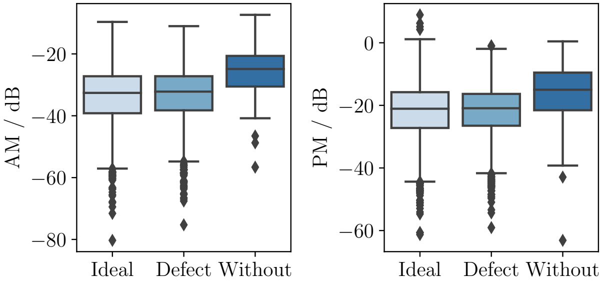

Figure A.9.: Amplitude modulation (left) and phase modulation (right) of the VAM measurements at the welded steel specimens, to accompany the MI of the main document.

A.7. Synthetic VAM

In this Chapter, additional material from the evaluation of the synthetic VAM is shown, first for the shown coupon specimens and afterwards for the more complex structures.

A.7.1. Coupon specimens

In addition to the shown results in the main document, the MI was plotted for every frequency of the dynamic measurements over the frequency and the maximal tensile stress of the specimen in Figure A.10. These measurements are used as reference to compare the following synthetic computation of VAM.

The measured signals of the undamaged specimen (max. stress of 22.2 MPa), show a severe frequency dependence of the MI. Observable are two areas (196 kHz & 205.5 kHz), which show a drastically reduced MI in the VAM measurements. After the first loading steps, the MI over the frequency remains constant, until the first crack occurs at 54 MPa. This crack results in an increased MI over the whole frequency range. This increase is only absent in the vicinity of the resonances, due to the already minimal modulation.

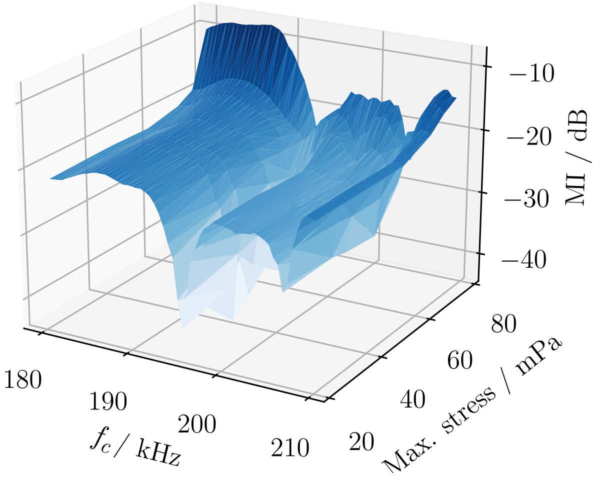

Figure A.10.: MI of the dynamic VAM measurement for all frequencies over the applied stress. Except for frequencies near resonances, a significant increase of the MI for all frequencies due to the inter-fibre cracks is occurring.

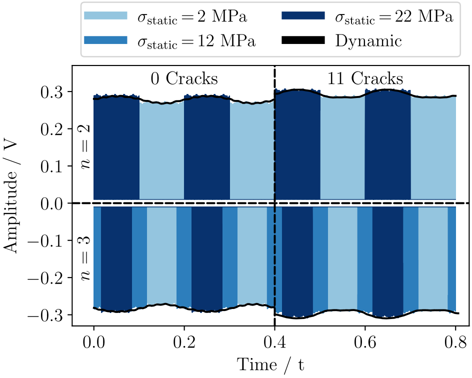

Figure A.11.: Synthetic generated signals (left) of a GFRP specimen from $n = 2$ (top) and $n = 3$ (bottom) static measurements for the pristine state compared to 11 cracks. The envelope of the dynamic VAM is given as a black line.

In Figure 5.9 of the main document, the synthetic VAM was evaluated for the frequency of 185 kHz. However, the shown relation of a decrease in amplitude due to the damage at the lower stress is only observable for that specific carrier frequencies. The relation between the different stress states for the to damage states is shown for $f_c = 209.5$ kHz in Figure A.11. At this carrier frequency, the signal amplitude at each all stress states increases due to the damage, which is not intuitive from a wave-propagation aspect. However, due to the changes in the specimen's eigenmode due to the damage, such a behaviour is also possible.

In Figure A.12 the process of the phase extraction is shown. Since the approximation results in values between $0 - 2\pi$, some adjustments have to be performed to become the representation of the main document. Throughout the frequency range, several jumps are visible (left). By applying the "unwrap" function from Numpy, a smooth slope of the phase was created (centre). The occurring downward trend is explainable by the decreasing wavelength of the carrier, the resulting change in the wave speed and time of arrival at the second piezoceramic. By applying a linear baseline correction (right), the differences between both stress states were highlighted, to improve the interpretability. The comparison of the baseline-corrected phase to the amplitude of the signal has been given in the main document in Figure 5.16.

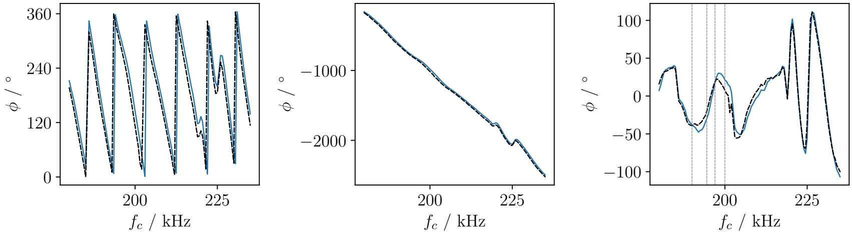

Figure A.12.: The evaluation of the Phase was possible by deleting the jumps at 0 and 2π (left). The resulting downward slope of the phase with increasing frequency (centre) was reduced by a baseline correction (right), to become a better interpretation of the difference in phase between both shown stress levels.

In the following, four tables present a parameter analysis, where the MI of the dynamic measurements is compared to the MI by the synthetic VAM, generated with different numbers of quantisation levels n, sampling frequencies f_s, and the number of points p. The label of each table includes the name of the specimen. Since a difference between both values is expected due to the process itself, also a deviation to the expected offset is calculated. The specified percentage is determined by dividing the deviation by the mean value of the MI of the frequency range.

Table A.2.: Specimen: GFRP 1

n	f_s [kSa/s]	p	Averaged difference [dB]	Deviation [dB]	[%]
2	2000	8	2.254 ± 0.447	0.154	0.73
2	2000	50	2.257 ± 0.448	0.157	0.74
2	20	8	2.256 ± 0.449	0.156	0.73
2	20	50	2.257 ± 0.447	0.157	0.74
3	2000	8	0.988 ± 0.438	0.138	0.61
3	2000	50	0.990 ± 0.437	0.140	0.63
3	20	8	0.989 ± 0.441	0.139	0.62
3	20	50	0.991 ± 0.436	0.141	0.63
7	2000	8	0.437 ± 0.439	0.027	0.12
7	2000	50	0.439 ± 0.437	0.029	0.12
7	20	8	0.438 ± 0.438	0.028	0.12
7	20	50	0.439 ± 0.437	0.029	0.13

Table A.3.: Specimen: GFRP 2

n	f_s [kSa/s]	p	Averaged difference [dB]	Deviation [dB]	[%]
2	2000	8	2.302 ± 0.418	0.202	0.97
2	2000	50	2.237 ± 0.388	0.137	0.66
2	20	8	2.322 ± 0.488	0.222	1.07
2	20	50	2.326 ± 0.421	0.226	1.08
3	2000	8	1.027 ± 0.348	0.177	0.80
3	2000	50	0.964 ± 0.304	0.114	0.52
3	20	8	1.050 ± 0.404	0.200	0.90
3	20	50	1.052 ± 0.336	0.202	0.92
7	2000	8	0.494 ± 0.314	0.084	0.37
7	2000	50	0.413 ± 0.288	0.003	0.01
7	20	8	0.507 ± 0.365	0.097	0.43
7	20	50	0.500 ± 0.302	0.090	0.40

Table A.4.: Specimen: Aluminum 1

n	f_s [kSa/s]	p	Averaged difference [dB]	Deviation [dB]	[%]
2	2000	8	1.828 ± 1.329	−0.272	−1.26
2	2000	50	1.909 ± 1.142	−0.191	−0.89
2	20	8	2.154 ± 1.308	0.054	0.25
2	20	50	1.960 ± 1.088	−0.140	−0.65
3	2000	8	0.630 ± 1.365	−0.220	−0.96
3	2000	50	0.727 ± 1.154	−0.123	−0.54
3	20	8	0.955 ± 1.303	0.105	0.47
3	20	50	0.770 ± 1.101	−0.080	−0.35

Table A.5.: Specimen: Aluminum 2

n	f_s [kSa/s]	p	Averaged difference [dB]	Deviation [dB]	Deviation [%]
2	2000	8	1.761 ± 0.804	-0.339	-1.86
2	2000	50	1.740 ± 0.805	-0.360	-1.98
2	20	8	1.762 ± 0.795	-0.338	-1.85
2	20	50	1.752 ± 0.775	-0.348	-1.91
3	2000	8	0.492 ± 0.730	-0.358	-1.84
3	2000	50	0.459 ± 0.708	-0.391	-2.00
3	20	8	0.487 ± 0.716	-0.363	-1.86
3	20	50	0.462 ± 0.683	-0.388	-1.99

A.7.2. The effect of Data Reduction

Besides the decoupling of VAM from the actual vibration, the synthetic VAM offers the possibility of data reduction and the reduced hardware requirements, which pave the way for the application of low-power sensor nodes. The cable-free deployment of sensors reduces the costs of such a system, and the ongoing costs for the monitoring of large structures drastically.

The energy consumption of a sensor node depends on the sampling rate and length of the measured response and intuitively the complexity of the evaluation and transmission of the data. Regarding the low-powered chips, especially the high sampling rate of $0.5 - 1\,\text{MHz}$ is the most challenging aspect. To overcome this aspect, first approaches have been published, in which the undersampling methods have been applied to the dynamic signal. The most relevant work in this regard, using similar specimens as this thesis, is the work of Oppermann *et al.* [97]. The application of the STFT algorithm on VAM measurements allowed for the reduction of measured points by 99.8 %. The increase in modulation could be reconstructed with an average error of $\Delta\text{MI} = 0.1668\,\text{dB}$ compared to the traditional evaluation. Despite the undersampled data residing at 0.2 %, still 1600 points are obtained during the period of 2 s, in which a constant amplitude and frequency of the ambient vibration are essential. While the constant vibration over a time of 2 s is suitable for laboratory applications, it is not likely in most industrial structures.

The synthetic VAM, on the other hand, requires even fewer data points. In the described experiment with a pumping frequency of $f_\mathrm{p} = 5\,\mathrm{Hz}$ and a carrier frequency of $f_\mathrm{c} = 200\,\mathrm{kHz}$, $3-8$ measured points of two stress levels are required for a precise reconstruction of the dynamic VAM. The resulting error for the presented GFRP specimen of this minimal number of points results in 0.202 dB over all frequencies and damage states and −0.339 dB for aluminium. In contrast to the dynamic VAM, where at least 0.2 s have to be acquired at 500 kSa/s which results in 100 000 data points per measurement, a reduction of measured data points of 99.984 % is feasible.

Moreover, the STFT algorithm or basic upsampling methods can be applied to the static measurements of the carrier f_c. This makes it possible to obtain the necessary information about each stress level from carrier signals that are sampled significantly below the carrier frequency $f_\mathrm{c} = 200\,\mathrm{kHz}$. To demonstrate this potential, the original static data for the synthetic VAM was downsampled by a factor of 100 by extracting every 100th point of the original signal, resulting in a sampling rate of $f_\mathrm{s} = 20\,\mathrm{kSa/s}$. From these downsampled signals, eight consecutive points were used to reconstruct the carrier frequency at each stress level and afterwards combined into a synthetic VAM signal. The fitting process was already used to elongate the signals of each stress level, so no additional modifications to the synthetic VAM were required. The downsampling barely affects the error of this method, which remains below 0.23 dB for the GFRP specimens and 0.34 dB for the aluminium specimens from two stress levels. Consequently, there is potential to further reduce the required sampling rate or number of points. Hardware requirements become minimal and achievable even in combination with energy harvesting and wireless data transmission. However, a base station is required to aggregate all the measurements and to compute and evaluate the synthetic signals.

A.7.3. Wind-turbine blade

The tested specimen from the wing of a wind turbine was chosen to evaluate, if impact damages are detectable with VAM and if the synthetic VAM method is working on this larger structure as well. The dynamic load for the pump vibration of VAM was introduced with a hydraulic testing machine. The load, which was introduced into the frontal surface of the structures was set to

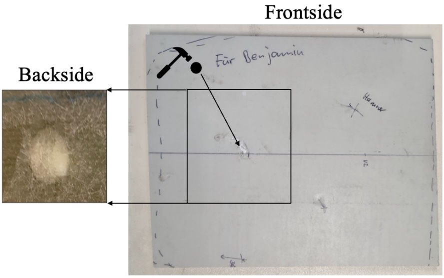

Figure A.13.: Frontside and backside around the introduced impact damage. The scale of both sides is equal, and the delaminations from the impact can be seen on the backside.

$F_p = 1.5 - 15\,\text{kN}$ to mimic the in-service loads. The carrier was introduced and measured with piezoceramics of two diameters (10 & 20 mm).

After an initial VAM measurement (index 0) the first impact was introduced at location 1, by a moderate tap with a hammer on a steel ball ($d = 15\,\text{mm}$). After the impulse, a VAM measurement has been performed. In five following subsequent impacts to the same location, the impact energy was subsequently increased. Before the seventh measurement, the energy was increased by using a hammer with a weight of 1 kg. The eighth impact was conducted by using a steel structure of 10 kg wight.

At the tested structure of the wind turbine blade, the carrier vibration was introduced with two piezoceramics of different diameters. The results of the 10x2 mm

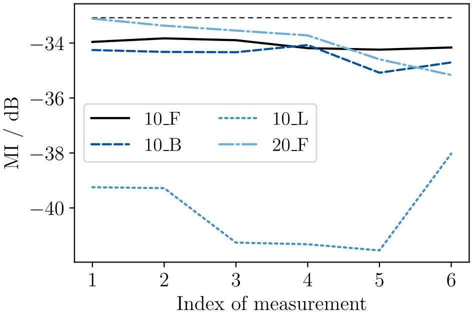

Figure A.14.: MI over the subsequent introduced impact damages for the excitation with the 20 mm piezoceramic.

piezoceramic actuator have already been presented in the main document. The MI over the measurements acquired with a 20 x 2 mm piezoceramic is shown in Figure A.14. Here, the trend observed before is not clearly visible. At the forward-facing 10 mm piezoceramic, an increase between the first and final test is observable. However, the measurements in between also result in a decrease of modulation.

A.7.4. Synthetic VAM at the composite cuboid

In Figure A.15 the measured amplitude of elongation of the VAM measurements over the lifetime is shown as the area between the minimum and maximum value (Dyn.). It is evident, that especially near the end of the experiment, the amplitude (and consequently the stress of the vibration) is drastically reduced, which affects the VAM evaluation and hinders the detection of the occurring damages. With the synthetic VAM, the choice of a constant amplitude for the VAM evaluation has been tested. An amplitude of 0.15 % elongation was selected. The minimal stress level was chosen by the minimal occurring stress in the VAM measurements (multiplied by 0.05) to prevent errors in the evaluation.

In Figure A.16 all four sides of the specimen are shown after the specimen was extracted from the testing machine. Visible in an angle of ±45°, is the fibre buckling. However, since the temperature chamber has been closed around the structure, the precise damage evaluation is not possible to reconstruct. In Chap-

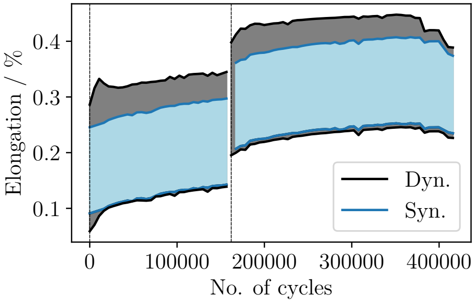

Figure A.15.: Comparison of the elongation, that was occurring during the dynamic VAM measurement (Dyn.) and the chosen amplitude of 0.15 of the synthetic measurement (Syn.), where the amplitude and phase were extracted from the dynamic VAM measurements, at the points in time, where the elongation passed the defined stress level.

ter 5.6.2, it was tried to reconstruct the damage mechanisms from the sensor data of the elongation and the VAM measurements.

Figure A.16.: All four sides of the cuboid after the testing. A severe fibre-buckling is visible, which runs around the structure, due to the combination of compression and torsion.

A.8. Integration of VAM into existing monitoring applications

In chapter 5, the synthetic VAM was proposed for the application of VAM in SHM applications. To complement the SHM integration, the potential of VAM and the relevance to progress VAM research outside the laboratory and onto industrial applications is underlined in this chapter. However, installing actuators for the pump and the carrier vibration and the sensor nodes for the actual VAM measurement results in high costs. In Chapter 5.4 the actuators for the pump vibration were replaced by utilising the ambient vibrations with the synthetic VAM approach. However, the excitation of the carrier vibration and the measurements of the resulting signal require installing the relevant equipment into the structure.

For a comprehensive study of the VAM method, this chapter is focused on the actual sensing of VAM. As known from the literature and indicated in Chapter 5.6.2, damage localisation with VAM is possible by comparing the modulations of several sensors at multiple locations. Therefore, the sensor where the MI increases the most should be closest to the damage. However, the method does not have the “technology readiness” level to replace the current best practices for damage detection and localisation. Hence, the application of VAM should—in the first stage—be an addition to the already implemented SHM systems, like acoustic emissions or other guided wave approaches.

To decrease the additional costs for the integration of VAM into the systems, the sensing of VAM with an acoustic emissions sensor has been tested in a test setup similar to the one presented in Chapter 5.4. The $[0,90_4]_s$ cross-ply laminate with a thickness of 3 mm and dimensions of 30 x 260 mm has been tested by consecutively increasing the maximal load. As before, the carrier frequency is introduced by the 2 x 10 mm piezoceramic disks on the upper side of the specimen in a frequency range of $f_\text{c} = 185 - 215\,\text{kHz}$, as shown in Figure A.17 (left). As visible on the lower half of the specimen, a second piezoceramic is applied to measure the occurring signal modulation. On the opposing side of the monitoring piezoceramic, a commonly used acoustic emissions sensor (Physical Acoustics R15a) is installed. This procedure allows for comparing both sensors as they acquire the vibrations at the same location but on opposing sides, which should result in comparable measurements. In Figure A.17 (right), the MI evolution from the pristine state to a damaged state with 13 severe inter-fibre cracks

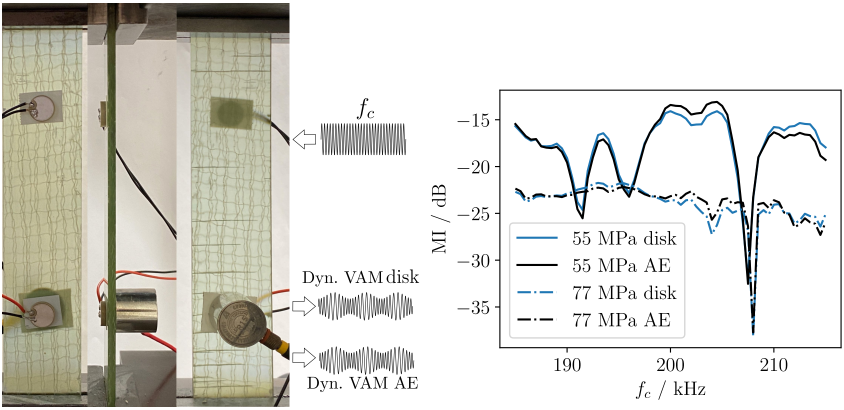

Figure A.17.: Picture of the tested specimen in a pristine state (left) shown from the front and the side. Both receiving piezoceramics have been attached by double-sided tape on opposing sides. After loading with 77 MPa, several cracks were initiated (backside view), which resulted in a significant increase of the MI in most frequencies (right).

is shown for the measured frequency range. A significant increase in MI can be seen for most frequencies. Furthermore, the measured MI of the acoustic emissions sensor closely matches the MI measured with the piezoceramics applied to measure VAM in this thesis. The resemblance between both reviving sensors is shown in Figure A.18. The MI is plotted over the maximal applied stress (left) and the resulting number of inter-fibre fractures at the individual damage state (right). These results again highlight the nearly linear increase in MI with each inter-fibre crack in these coupon specimens, even if the cracks penetrate only half the width.

Based on this ideal resemblance, the receiving piezoceramics of this thesis could be replaced by most piezoceramic sensors used to measure acoustic emissions and which are already attached to the structure for other purposes. Consequently, only the software of these existing systems has to be adapted to filter out the carrier vibrations used for VAM. However, since the VAM measurements can be performed in a regular pattern, this filtering process is a trivial adaptation in most cases. It enables the integration of VAM into many commercial SHM systems with only minimal effort. The resulting system could combine *e.g.* the passive acoustic emissions recording of emitted energy caused by ruptures of the

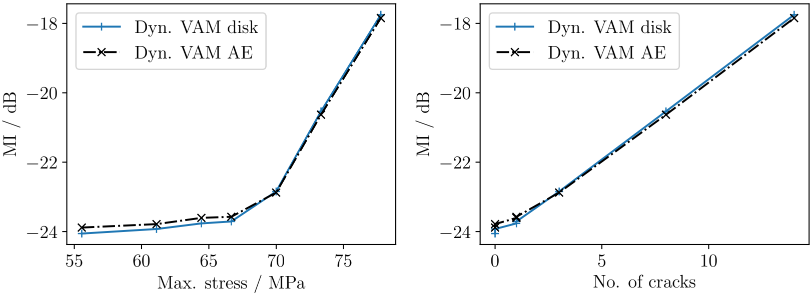

Figure A.18.: Comparison of the MI measured with an acoustic emissions sensor and the usual 2x10 mm disk actuator. Both sensors show the same quantitative result with minimal divergence between the absolute signal strength and MI.

material with the active VAM method that can evaluate the structural integrity at any point in time.